

Characterization of Phosphoric Acid Doped Polybenzimidazole Membranes

Yu Lin

Energie & Umwelt / Energy & Environment

Band / Volume 440

ISBN 978-3-95806-364-8

Forschungszentrum Jülich GmbH
Institut für Energie- und Klimaforschung
Elektrochemische Verfahrenstechnik (IEK-3)

Characterization of Phosphoric Acid Doped Polybenzimidazole Membranes

Yu Lin

Schriften des Forschungszentrums Jülich
Reihe Energie & Umwelt / Energy & Environment

Band / Volume 440

ISSN 1866-1793

ISBN 978-3-95806-364-8

Bibliografische Information der Deutschen Nationalbibliothek.
Die Deutsche Nationalbibliothek verzeichnet diese Publikation in der
Deutschen Nationalbibliografie; detaillierte Bibliografische Daten
sind im Internet über <http://dnb.d-nb.de> abrufbar.

Herausgeber
und Vertrieb: Forschungszentrum Jülich GmbH
 Zentralbibliothek, Verlag
 52425 Jülich
 Tel.: +49 2461 61-5368
 Fax: +49 2461 61-6103
 zb-publikation@fz-juelich.de
 www.fz-juelich.de/zb

Umschlaggestaltung: Grafische Medien, Forschungszentrum Jülich GmbH

Druck: Grafische Medien, Forschungszentrum Jülich GmbH

Copyright: Forschungszentrum Jülich 2018

Schriften des Forschungszentrums Jülich
Reihe Energie & Umwelt / Energy & Environment, Band / Volume 440

D 82 (Diss., RWTH Aachen University, 2018)

ISSN 1866-1793
ISBN 978-3-95806-364-8

Vollständig frei verfügbar über das Publikationsportal des Forschungszentrums Jülich (JuSER)
unter www.fz-juelich.de/zb/openaccess.



This is an Open Access publication distributed under the terms of the [Creative Commons Attribution License 4.0](https://creativecommons.org/licenses/by/4.0/),
which permits unrestricted use, distribution, and reproduction in any medium, provided the original work is properly cited.

Characterization of phosphoric acid doped polybenzimidazole membranes

Abstract

A polymer electrolyte fuel cell (PEFC) is an energy converter that converts the chemical energy of a fuel directly into electrical energy through electrochemical reactions. Compared to classic PEFCs, high-temperature PEFCs (with operating temperatures between 140-180 °C) have several advantages, such as high carbon monoxide tolerance and easier water management. A key component of HT-PEFCs is the phosphoric acid-doped polybenzimidazole (PBI) membrane. The interactions between the components of the $\text{PBI-H}_3\text{PO}_4\text{-H}_2\text{O}$ ternary system have an influence on cell behavior. In this work, this system was investigated by means of ex situ, in situ and operando methods. In ex situ doping experiments, the water and acid uptake of the membranes were determined at different temperatures and acid concentrations. The water uptake of the membranes increased slightly in the range of 30 to 70 °C, but decreased significantly in the range of 70 to 110 °C, while the acid doping level of the membrane increased across the entire temperature range. The acid doping and water absorption increased with increasing acid concentration of the solution in the doping bath within the investigated range of acid concentration of 1.66-14.67 M. At low acid concentrations, the water absorption is independent of the acid absorption. In the case of high acid concentrations in the doping bath, the water absorption is coupled with acid absorption.

As shown by in-situ current density measurements, the partial pressure of water vapor along the channel can have a significant impact on the local current density distribution. In the gas flow direction, the partial pressure of water vapor on the cathode side increases with dry input gases and a stoichiometry of two from 0 up to a maximum of 210 mbar. Accordingly, a local phosphoric acid concentration in the cell of between 76 wt.-% P_2O_5 and 68 wt.-% P_2O_5 at 160 °C arises. The resulting local differences in proton conductivities can affect the performance of a cell. It was found that due to the high water vapor partial pressure at the cell exit and the associated high proton conductivity, the effect of oxygen depletion can be overcompensated. After an initial decrease in the current density, this increased again in the direction of the cathode-side gas outlet.

Long-term measurements with single cells showed that based on impedance measurements, which the ohmic resistance of the cells decreased during the measurement period, whereas charge transfer and mass transport increased. The solubility of the PBI membranes in the hot phosphoric acid environment can be responsible for this. The dissolution phenomena of the membrane results, on the one hand, in a reduction in the membrane thickness, with the result of decreasing ohmic resistance. On the other hand, membrane material penetrates into the catalyst layer and reduces the usable active area of the catalyst. However, these two opposite effects ultimately lead to the degradation of the cell.

By operando-neutron radiography experiments with H_2 and D_2 as fuel gas, different H-to-D and D-to-H exchange times were detected in the phosphoric acid-doped membrane. On the basis of statistical considerations, the assumption of quantum-mechanical H-D transition probabilities and that only phosphoric acid is involved in the exchange, the different exchange times can be explained while maintaining the charge retention. The estimated times for the complete replacement of H_3PO_4 with D_3PO_4 in the phosphoric acid are in good agreement with the neutron radiographically-measured values.

Charakterisierung von phosphorsäuredotierten Polybenzimidazol-Membranen

Kurzfassung

Eine Polymerelektrolytbrennstoffzelle (PEFC) ist ein Energiewandler, der die chemische Energie eines Brennstoffes durch elektrochemische Reaktionen direkt in elektrische Energie umwandelt. Im Vergleich zu klassischen PEFCs hat die Hochtemperatur-PEFC (Betriebstemperatur zwischen 140-180 °C) mehrere Vorteile, wie zum Beispiel eine hohe Kohlenmonoxid-Toleranz und ein einfacheres Wassermanagement. Eine Schlüsselkomponente der HT-PEFC ist die Phosphorsäure-dotierte Polybenzimidazol (PBI)-Membran. Die Wechselwirkungen zwischen den Komponenten des Ternärsystems $\text{PBI-H}_3\text{PO}_4\text{-H}_2\text{O}$ haben Einfluss auf das Zellverhalten. In der vorliegenden Arbeit wurde dieses System mit ex-situ, in-situ und operando Methoden untersucht.

In ex-situ-Dotierungsexperimenten wurden die Wasser- und die Säureaufnahme der Membranen bei verschiedenen Temperaturen und Säurekonzentrationen bestimmt. Die Wasseraufnahme der Membranen nahm leicht im Bereich von 30 bis 70 °C zu, nahm jedoch deutlich im Bereich von 70 bis 110 °C ab, während der Säuredotierungsgrad der Membran im gesamten Temperaturbereich anstieg. Der Säuredotierungsgrad und die Wasseraufnahme stiegen bei steigender Säurekonzentration der Lösung im Dotierungsbad im untersuchten Bereich der Säurekonzentration von 1,66-14,67 M an. Bei geringen Säurekonzentrationen zeigt sich die Wasseraufnahme unabhängig von der Säureabsorption. Im Falle von hohen Säurekonzentrationen im Dotierungsbad ist die Wasseraufnahme mit der Säureabsorption gekoppelt.

Wie durch in-situ Stromdichtemessungen gezeigt, kann der Wasserdampfpartialdruck entlang des Kanals signifikante Auswirkungen auf die lokale Stromdichteverteilung haben. Entlang der Gasströmungsrichtung steigt der Wasserdampfpartialdruck auf der Kathodenseite, bei trockenen Eingangsgasen und einer Stöchiometrie von zwei, von 0 auf maximal 210 mbar. Entsprechend stellt sich eine lokale Phosphorsäurekonzentration in der Zelle zwischen 76 Gew.-% P_2O_5 und 68 Gew.-% P_2O_5 bei 160 °C ein. Die sich hieraus ergebenden lokalen Unterschieden der Protonenleitfähigkeiten können sich auf das Betriebsverhalten einer Zelle auswirken. Es zeigte sich, dass aufgrund des hohen Wasserdampfpartialdrucks am Zellausgang und der damit verbundenen hohen Protonenleitfähigkeit der Effekt der Sauerstoffabreicherung überkompensiert werden kann. Nach einem anfänglichen Abfall der Stromdichte, stieg diese in Richtung des kathodenseitigen Gasaustrittes wieder an.

Bei Langzeitmessungen mit Einzelzellen zeigte es sich, basierend auch Impedanzmessungen, dass der ohmsche Widerstand der Zellen während der Messdauer abnahm, wohingegen Ladungstransfer und Massentransport anstiegen. Die Löslichkeit der PBI-Membranen in der heißen phosphorsauren Umgebung kann hierfür verantwortlich gemacht werden. Die Auflösungserscheinungen der Membran resultiert auf der einen Seite in einer Verringerung der Membrandicke mit der Folge eines abnehmenden ohmschen Widerstandes. Auf der anderen Seite dringt Membranmaterial in die Katalysatorschicht ein und reduziert als Folge die nutzbare aktive Fläche des Katalysators. Diese beiden gegenläufigen Effekte führen letztendlich jedoch zu einer Degradation der Zelle.

Durch operando-Neutronen-Radiographieexperimente mit wechselweise H_2 und D_2 als Brenngas konnten unterschiedliche H-zu-D und D-zu-H Austauschzeiten in der phosphorsäuredotierten Membran nachgewiesen werden. Aufgrund statistischer Betrachtungen, der Annahme von quantenmechanisch basierten H-D Übergangswahrscheinlichkeiten und der Annahme, dass an dem Austausch ausschließlich

die Phosphorsäure beteiligt ist, können die unterschiedlichen Austauschzeiten unter Beibehaltung der Ladungserhaltung erklärt werden. Die mit diesem Modell abgeschätzten Zeiten für den kompletten Austausch von H_3PO_4 nach D_3PO_4 in der Phosphorsäure sind in guter Übereinstimmung mit den neutronenradiographisch gemessenen Werten.

Contents

1	Introduction and Goal of work	1
1.1	Working principle.....	2
1.2	Goal of work.....	3
1.3	Outline.....	3
2	Literature overview and device introduction	5
2.1	Literature review.....	5
2.1.1	PBI and its derivatives	6
2.1.2	Composite PBI membranes.....	10
2.1.3	The proton transferring mechanism in phosphoric acid	11
2.2	Device introduction.....	13
2.2.1	Karl Fischer Titration	13
2.2.2	Local current density measurement device (current scan shunt)	15
2.2.3	Neutron radiography	17
3	Membrane doping.....	21
3.1	Experimental setup.....	22
3.1.1	Definition and calculation of water uptake and phosphoric acid doping level	23
3.1.2	Definition and calculation of thickness and volumetric swelling.....	24
3.2	Results and discussion	25
3.2.1	Ternary system of <i>m</i> -PBI – H ₃ PO ₄ – H ₂ O	25
3.2.2	Doping temperature VS water uptake	26
3.2.3	Concentration of phosphoric acid solution VS water uptake	28
3.2.4	Crosslinking degree of <i>m</i> -PBI membranes VS water uptake	29
3.2.5	Temperature and acid concentration effect on ADL	30
3.2.6	ADL of crosslinked <i>m</i> -PBI membranes	32
3.2.7	Acid concentration in polymer.....	33
3.2.8	Dimension variations of pure <i>m</i> -PBI	34

3.2.9	Dimension variations of crosslinked <i>m</i> -PBI membranes	36
3.2.10	Single cell performance.....	38
3.3	Summary	41
4	Dissolution of PBI membranes in phosphoric acid solution	43
4.1	Experimental setup	44
4.1.1	Materials	44
4.1.2	Determination of the weight loss of membranes after dissolution.....	45
4.2	Results and discussions.....	48
4.2.1	Dissolving membranes in open vessel	48
4.2.2	Dissolving membranes in closed vessel	54
4.3	Summary	57
5	Long-term single cell test and post-mortem analysis.....	59
5.1	Experimental setup	59
5.1.1	MEA assembly.....	59
5.1.2	Single cell tests and EIS measurements.....	60
5.1.3	Sample preparation for post-mortem analysis.....	62
5.2	Results and discussions.....	64
5.2.1	Single cell test results.....	64
5.2.2	EIS results	65
5.2.3	Post-mortem analysis -- SEM results	68
5.2.4	Post-mortem analysis -- EDX results	73
5.3	Summary	76
6	Local current density analysis of the operando cell	77
6.1	Experimental setup	77
6.1.1	Cell design	77
6.1.2	MEA preparation.....	78
6.2	Results and discussion	79
6.3	Model.....	81
6.3.1	Oxygen concentration effect	81
6.3.2	Water vapor partial pressure effect.....	83
6.4	Summary	87
7	Operando Neutron radiography of HT-PEFC.....	89

7.1	Experimental setup	89
7.2	Results and discussions	90
7.2.1	Cell performance and EIS	90
7.2.2	Determination phosphoric acid content	94
7.2.3	Overall H/D exchange process in the MEA	96
7.2.4	Models of the substitution between H and D	97
7.2.5	Local H/D exchange process of MEA	102
7.2.6	Impact of different current density on H/D exchange process in the MEA	105
7.2.7	Transmittance changes in dependent of different gas flow rates at the cathode	106
7.2.8	Difference of MEA between under channels and ribs of flow field	108
7.3	Summary	109
8	Discussion	111
9	Conclusion	115
	Bibliography	117
	Nomenclature	125
	List of Figures	131
	List of Tables	137
	Acknowledgments	139

1 Introduction and Goal of work

Climate change [1] and increasing energy demand [2] are two of the most important challenges facing human beings. With advantages such as zero-carbon emissions and high energy conversion efficiency, polymer electrolyte fuel cells (PEFCs) are recognized as an alternative solution for future energy conversion technologies and have achieved substantial development in recent years [3].

PEFC is a clean energy-converting device, which directly converts the chemical energy of fuel into electrical energy through an electrochemical reaction [4]. It can be applied in many areas, such as portable, mobile and stationary power generation. According to different electrolyte and operating temperature, PEFC can be classified in two types: 1) classical PEFC, which is based on PFSA-type membranes (e.g., the well-known Nafion® series membranes) and is operated between 60-90 °C; 2) high temperature polymer electrolyte fuel cell (HT-PEFC), which is based on phosphoric acid-doped polybenzimidazole (PBI) membranes, with higher operating temperature between 140-180 °C[5-7].

Nevertheless, hydrogen is the main fuel for these two types of PEFCs. To date, hydrogen is mainly produced by steam reforming of natural gas or other fossil fuels, such as propane, gasoline, diesel, methanol, or ethanol [8-10]. However, steam reforming of fossil fuels produces low purity hydrogen with a high concentration of carbon monoxide. The carbon monoxide molecules can be adsorbed on the surface of platinum of a PEFC, which blocks the active sites on the catalyst and decreases the performance [11, 12]. In the case of classical PEFC, only 5-10 ppm carbon monoxide mixing in the feed fuel can poison the platinum/carbon catalyst [13]. On the other hand, since the classical PEFC is operating below boiling temperature of water at ambient pressure, the existence of liquid water inside the cell is always an issue. With low water content, the Nafion membrane would be dehydrated, which will dramatically decrease the proton conductivity of the membrane, but with high water content, the gas diffusion layers (GDLs) and gas channels would be flooded, which will block the gas transport pathway. Therefore, complex water management is needed for the classical PEFC. However, the HT-PEFC based on PBI membranes doped with phosphoric acid can overcome the problems mentioned above due to the higher operating temperature.

1.1 Working principle

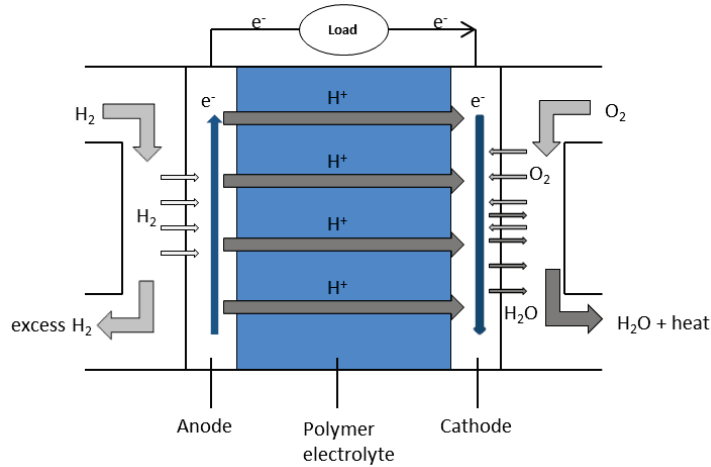
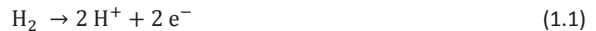


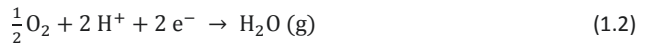
Figure 1.1: The basic working principle of HT-PEFC

The Basic working principle of HT-PEFC is displayed in Figure 1.1. It is worth to note that, other components (GDLs and catalyst layers on the both side of the polymer electrolyte) of an MEA (membrane electrolyte assembly) in a HT-PEFC are not shown here since they are not the focus of this work. When the HT-PEFC is operating, hydrogen and oxygen (normally air) are pumped into the cell at anode and cathode separately. In the anode, the hydrogen molecule splits into two protons and two electrons under the action of catalyst. The protons transfer through the electrolyte to the cathode side and the electrons move through the external circuit also to the cathode side. On the cathode side, the protons and electrons react with oxygen and generate water and heat. The water production is mainly in the gaseous phase. The electrochemical reactions are shown below:

Anode reaction:



Cathode reaction:



Overall reaction:



1.2 Goal of work

As one of the key component of the HT-PEFC, PBI membrane doped with phosphoric acid plays an important role. It serves as a proton conducting electrolyte, an interfacial environment for electrochemical reaction, an effective reactant separator, as well as a support for catalysts/electrodes. In the present study, several ex-situ and in-situ experiments were conducted in order to investigate the doping behavior of the PBI membrane with phosphoric acid, the degradation mechanism of the membrane and the proton transport mechanism inside the membrane.

1.3 Outline

- Chapter 2 presents the status of the research in the literature and introduces the main devices used in this work.
- Chapter 3 investigates the interactions of each component in the system of PBI-H₃PO₄-H₂O.
- Chapter 4 studies on the dissolution behaviors of AB-PBI at a series of temperature in various concentrated phosphoric acid solutions.
- Chapter 5 investigates the degradation mechanism of the membrane in HT-PEFCs.
- Chapter 6 discusses the influence of different factors on local current density distribution.
- Chapter 7 displays the operando neutron radiograph in HT-PEFC.
- Chapter 8 and 9 are the overall discussion and conclusion.

2 Literature overview and device introduction

In this chapter, a literature review about the PBI membrane will be given, and some of the main devices which were used will be introduced.

2.1 Literature review

The polybenzimidazole membrane doped with phosphoric acid was first used as polymer electrolyte of fuel cells by Wainright et al. [7]. It showed that the proton conductivity was affected by the water vapor activity and temperature. After that a lot of attention has been attracted by PBI/H₃PO₄ based HT-PEFC. PBI membranes have a lot of advantages such as excellent chemical and thermal stability (glass transition temperature, $T_g=425-436$ °C) and good mechanical strength [6]. After doped with phosphoric acid, the PBI membranes exhibit very good proton conductivity. These properties make the PBI membrane a very good polymer electrolyte for HT-PEFC.

Besides phosphoric acid, PBI has also been doped with some other acids, such as sulphuric acid, perchloric acid and so on [14]. However, phosphoric acid is the most suitable due to its superior thermal stability, high proton conductivity and low vapor pressure at elevated temperature. In phosphoric acid doped PBI membrane, PBI is the polymeric membrane material and phosphoric acid is the proton carrier. It is reported that phosphoric acid doped PBI have good thermal stability and high proton conductivity. Samms et al. [15] investigated the thermal stability of phosphoric acid doped PBI membranes under atmospheres of either nitrogen, 5% hydrogen, or air. They found that weight loss of doped membranes below 400 °C was due to loss of absorbed water and dehydration of phosphoric acid in all cases, which indicates the thermal stability of the doped membranes, is more than adequate for use as a polymer electrolyte in HT-PEFC. Xiao et al. [16] prepared pyridine-based PBI membranes by direct-casting of the polyphosphoric acid (PPA) polymerization solution without isolation or re-dissolution of the polymers. These membranes exhibited high proton conductivities of 0.1 to 0.2 S cm⁻¹ at 160 °C with an acid doping level range of 15 to 25 molecules phosphoric acid per PBI repeating unit. This generally satisfies the target of U. S. Department of

Energy (DoE) (0.1 S cm^{-1} at 120°C) [17]. Furthermore, the higher operation temperature (comparing with the DoE target: 120°C) between 150°C to 180°C in HT-PEFC can lead to better CO tolerance of the catalyst.

2.1.1 PBI and its derivatives

Currently, the most widely studied PBIs are poly[2,2'-(m-phenylene)-5,5'-bibenzimidazole] and poly(2,5-benzimidazole), denoted as m-PBI (or often only PBI) and AB-PBI, respectively. The chemical structures of the repeating units of PBI and AB-PBI are shown in the Figure 2.1. As it shows, these polymers contain two basic functionalities (—NH— and =N—) that can build up hydrogen bonds (—N—H... O—) with the phosphoric acid molecules. These hydrogen bonds offer the ability for PBI polymer absorbing acidic electrolyte which provides the high proton conductivity of the doped membranes.

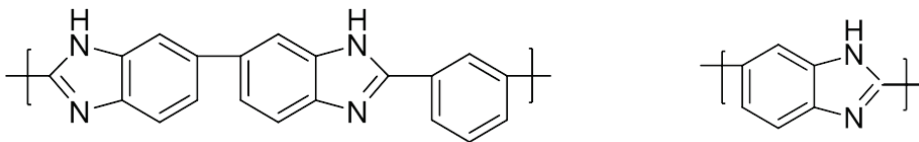


Figure 2.1: Chemical structure of the repeating units of PBI (left) and AB-PBI (right).

Apart from m-PBI and AB-PBI, there are various polybenzimidazole synthesized derivatives. One has very similar molecular structure as m-PBI, only the m-phenylene group is substituted by p-phenylene. The poly[2,2'-(p-phenylene)-5,5'-bibenzimidazole] (p-PBI) was first synthesized in the early 1960s [18, 19]. The introduction of the p-phenylene linkage in the backbone enhanced the flexibility of the polymer chain. The p-PBI has superior tensile strength and stiffness [20] but lower glass transition temperature by 59°C [21], compared with the m-PBI.

Among the various PBI derivatives, the phenyl ring in the backbone of the polymer chain was modified or substituted very often. For example, Kallitsis and Gourdoupi [22, 23] prepared a blend membrane (pyridine-based PBI) by using polar pyridine groups as a main chain linkage of aromatic copolymers. These membranes show enhanced chemical stability against oxidative degradation. It was found [16, 24] that, when the phenyl ring was substituted by the pyridine ring, the incorporation of an extra nitrogen atom in the polymer significantly improves the solubility. In

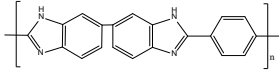
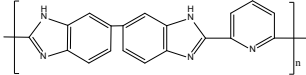
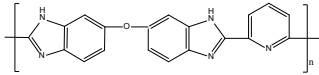
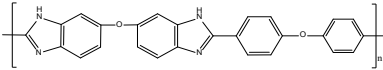
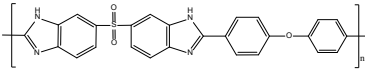
addition, the numbers of N atoms or NH groups in PBI structures have strong effect for enhancing the acid doping and proton conductivity. Carollo et al. [25] synthesized and compared a series of PBIs with different numbers of N atoms and membrane molecular weight. They found that both the acid doping level and the proton conductivity remarkably increased with the membrane molecular weight and basicity, which depend on the amount of NH-groups as well as on their position in the polymer backbone.

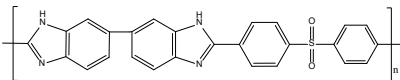
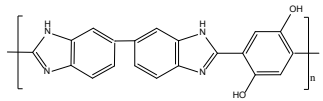
Moreover, by introducing ether and sulphone into the main chains of PBI polymers, Fumatech [26] has synthesized Py-O-PBI, OO-PBI and OSO₂-PBI. Similarly, Qing et al. [27] prepared sulphone containing PBI. Their results showed that the polymers containing ether, sulphone, etc., are soluble in common organic polar solvents like N-methylpyrrolidone (NMP) and N,N-dimethylacetamide (DMAc). The good solubility allows further processing, modification (cross-linking, sulphonation to high ion exchange capacity) and production of membranes with excellent mechanical properties.

Another attempt was made by using a variety of diacids to modify the PBI structures. Yu et al. [28] synthesized poly[2,2'-(2,5-dihydroxy-1,4-phenylene) 5,5'-bibenzimidazole] (2OH-PBI) which is insoluble in concentrated sulphuric acid and much less soluble in phosphoric acid against para-PBI. However, membranes by direct casting of the polymer solution in polyphosphoric acid (PPA) showed much higher conductivity than the corresponding para-PBI films.

The information of all the PBI and its derivatives are shown in the Table 2.1 below.

Table 2.1: Derivatives of PBI.

Polymers	Functional groups	Properties	Structures
p-PBI	p-phenylene	superior tensile strength, lower glass transition temperature	
pyridine-based PBI	pyridine	high acid doping level and proton conductivity	
Py-O-PBI	pyridine and ether	good solubility, membrane casting	
OO-PBI	ether	good solubility, membrane casting	
OSO2-PBI	ether and sulphone	good solubility, membrane casting	

Sulphone-PBI	sulphone	good solubility, membrane casting	 <p>The chemical structure shows the repeating unit of Sulphone-PBI. It consists of two benzimidazole rings connected at their 2-positions. The 5-position of the first benzimidazole ring is linked to the 6-position of the second benzimidazole ring. The 4-position of the second benzimidazole ring is connected to a para-phenylene ring, which is further linked to a sulfonyl group (-SO₂-) and another para-phenylene ring. The entire unit is enclosed in brackets with a subscript 'n'.</p>
2OH-PBI	dihydroxy	insolubility, high proton conductivity	 <p>The chemical structure shows the repeating unit of 2OH-PBI. It features two benzimidazole rings connected at their 2-positions. The 5-position of the first benzimidazole ring is linked to the 6-position of the second benzimidazole ring. The 4-position of the second benzimidazole ring is connected to a benzene ring that has two hydroxyl groups (-OH) at the 3 and 5 positions. The entire unit is enclosed in brackets with a subscript 'n'.</p>

2.1.2 Composite PBI membranes

Apart from the modifications of the main chains of the polymers, addition of inorganic-organic substances is another way to improve the thermal stability, water absorption, reactant crossover resistance, mechanical strength and proton conductivity of the polymer membranes [29-31].

Pu et al. [32] and Quartarone et al. [33] prepared a series of PBI/SiO₂ composite membranes. They found the mechanical properties of the membranes were improved. After doping with phosphoric acid, the composite membranes could maintain more than half of the tensile strength of the undoped membranes, while the pure PBI membrane could only keep less than one-third of the tensile strength. Furthermore, the existence of SiO₂ in the composite membranes could enhance the ability to capture phosphoric acid, which is good for the proton conductivity of the membranes.

Zirconium dioxide (ZrO₂) has also been used as an additive to prepare composite PBI membranes by Nawn et al. [34]. The presence of the nano-ZrO₂ particles increased the thermal stability of the membranes. A proton conductivity of up to $1.04 \times 10^{-1} \text{ Scm}^{-1}$ at 185 °C was obtained.

Another attempt of preparing composite PBI membranes is mixed with titanium dioxide (TiO₂) by Lobato et al. [35-37]. It revealed that the PBI/TiO₂ composite membranes showed more or less high and stable proton conductivity (nearly $1.3 \times 10^{-1} \text{ S cm}^{-1}$) in the temperature range of 125 °C – 175 °C, while the membranes without TiO₂ showed a decrease in the conductivity with temperature due to a dehydration process. The results [38] from the long-term testing of the composite membranes in HT-PFEC demonstrated that the TiO₂ in the membranes caused not only water retention but also acid retention, which prevented the leakage of phosphoric acid from the membrane.

Since the proton resistance of the membrane is associated with the thickness of the membrane, Lin et al. [39] prepared the PBI/PTFE composite membranes, which had a thickness of roughly 22 μm and good mechanical strength. However, the lower thickness causes high gas permeability [40] which was indicated by the low OCV (open cell voltage) of the cell using this composite membrane.

2.1.3 The proton transferring mechanism in phosphoric acid

As mentioned before, the pure PBI membrane does not conduct protons. Only after it absorbs some acids, especially phosphoric acid here, it can exhibit excellent proton conductivity. Therefore, phosphoric acid is recognized as the main electrolyte in the PBI/H₃PO₄ system.

In phosphoric acid, charge can be transferred by proton migration or by migration of anions such as H₂PO₄⁻, H₃P₂O₇⁻ or H₂P₂O₇²⁻ [41, 42]. However, the migration of protons is much more interesting in fuel cell application. Generally, there are two principles of proton migration, which are widely accepted [43]. One describes that protons hop between H₂O molecules or/and H₃PO₄, which is called Grotthuss mechanism (also called hopping mechanism); the other (vehicle mechanism) depicts that protons move with the migration of H₃O⁺ or H₄PO₄⁺ ions, in which the ions serve as vehicles and protons are like passages.

However, proton migration via a hopping mechanism is much faster than the migration via vehicle mechanism, which was discussed by Dippel et al. [44]. They demonstrated that the rate of proton transfer via the hopping mechanism is about 170 times faster than that of vehicle diffusion, assuming a jump length of 443 pm corresponding to the average P/P distance. Furthermore, by means of the PFG-NMR (pulsed field gradient – nuclear magnetic resonance) technique, the self-diffusion coefficients of ¹H and ³¹P in fused H₃PO₄ at the melting temperature ($T_{\text{melt}} = 42\text{ }^{\circ}\text{C}$) were measured [44, 45]. It revealed that ¹H diffusion constant is roughly 4.5 times larger than that of ³¹P, which demonstrated that $\approx 98\%$ of proton migrations resulted from hopping mechanism while only about 2% of the conductivity was contributed from vehicular diffusion of phosphorus species.

In addition, by the NMR studies, the proton transport mechanisms were determined at various concentrations of phosphoric acid. Chung et al. [46] found that the diffusion coefficients and conductivity values are greater for the 85 wt.-% than for the 100 wt.-% concentration of phosphoric acid. They suggested that the presence of water in 85 wt.-% phosphoric acid system plays a significant role in providing a pathway for protons from one molecule to the next and a probable mode of proton transfer in the 85 wt.-% phosphoric acid is between adjacent acid sites through an intermediate H-bonded water molecule. Aihara et al. [47] measured the self-diffusion coefficients of H and P in phosphoric acid with concentrations ranging from 75 to 105 wt.-%. They found the self-diffusion coefficient of H was always larger than that of P. And with the concentration range of 75-

105 wt.-%, the self-diffusion coefficient ratios of H/P were increased from 2.7 to 5.3 at 313K. Additionally, in the case of 75 wt.-% phosphoric acid, the averaged proton diffusion coefficients were enhanced by the free water diffusion indicating proton transport through water molecules. In general, protons will be transferred mainly between water molecules in the case of low phosphoric acid concentrations (as shown in Figure 2.2 (a)). In the case of high phosphoric acid concentrations, in which the fraction of water molecules is very small compared with the fraction of phosphoric acid molecules, protons will move directly between H_3PO_4 molecules (as shown in Figure 2.2 (b)).

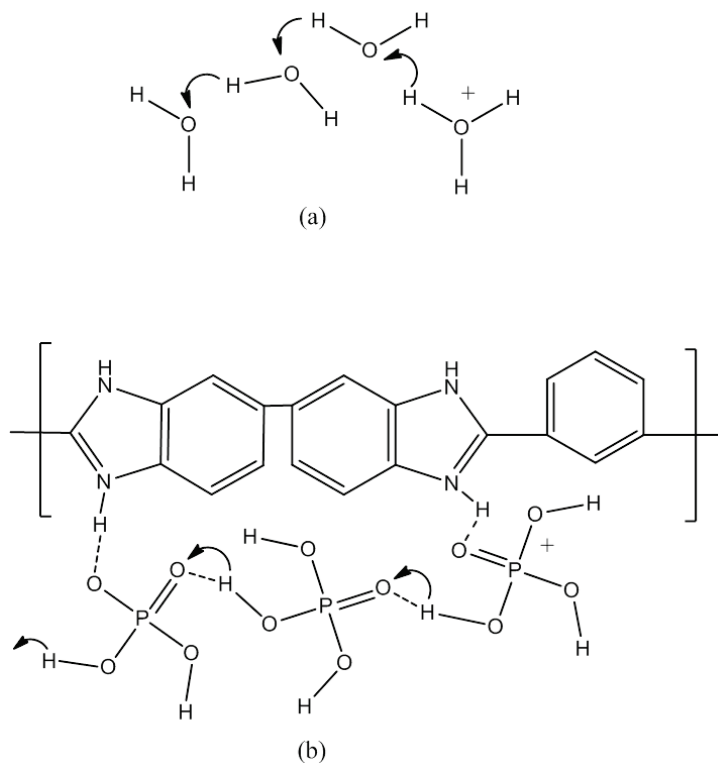


Figure 2.2: Proton migration via hopping mechanism in PBI/ H_3PO_4 system. (a) at low concentration of H_3PO_4 in the membrane, protons transfer between free water molecules; (b) at high concentration of H_3PO_4 in the membrane, protons transfer through bonded H_3PO_4 network.

Furthermore, proton transport via the aqueous phosphoric acid is very sensitive to the composition and temperature of the phosphoric acid solution. Greenwood et al. [41] displayed that the activation energy of proton transport in fused phosphoric acid decreased from 6.0 to 4.5 kcal mol⁻¹

when the temperature increased from 25 to 60 °C. McDonald et al. [48] measured the conductivity of phosphoric acid with concentration ranging from 85.10 wt.-% to 99.72 wt.-% at 130 °C. The conductivity decreased from 0.4904 to 0.3982 S cm⁻¹. Chin et al. [42] and Korte [43] presented more detailed data of conductivity of phosphoric acid as functions of composition and temperature. Generally, the proton conductivity will increase with the concentration until a maximum value and then decrease with further increasing of concentration. This is because that, at low concentration, there are not enough free protons in the solution, and with the increase of the phosphoric acid amount, the protons amount in the acid solution increase which provides more charges for conduction. However, after the protons are saturated in the solution, with the increase of the phosphoric acid concentration, the dissociation of protons is restrained and the viscosity of the solution increases, which is harmful to proton transport. On the other hand, the proton conductivity increases with the temperature. This is mainly due to the increasing of thermal motion of protons and hydrogen bond, which makes the kinetics of proton transport faster.

2.2 Device introduction

In this part, some of the main devices used in this work will be introduced.

2.2.1 Karl Fischer Titration

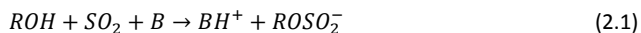
In order to measure the water uptake of PBI membranes after doping with phosphoric acid, the Karl Fischer Titration was induced. The device is showed in Figure 2.3.



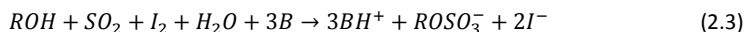
Figure 2.3: Karl Fischer Titration system

Karl Fischer Titration (KFT) is a common measurement method for determining trace amounts of water in different samples [49-52]. It was first introduced by Karl Fischer in 1935. Karl Fischer Titration (KFT) includes volumetric titration and coulometric titration. For coulometers, the measuring range is from 1-5ppm to ca. 5% [53]. However, most of the samples have the water content over 5%. In order to make sure all the data acquired has the same accuracy, the volumetric Karl Fischer Titration (vKFT) with the measuring range from 1% to 100% [50] is used for determining water contents in samples.

The main components of the titrant solution for KFT include solvent, base, Sulphur dioxide (SO_2) and iodine (I_2). The typical solvent that can be used is methanol or diethylene glycol monoethyl ether which can provide good solubility of other components and a fast reaction rate. Here, methanol was applied. The base (here, it is imidazole) is used to buffer the pH of the KF solution in the optimum range between 5 and 8. The following reaction equations [51] show the basic principle of the KFT.



Overall reaction:



where R is alkyl group, B is base (imidazole).

As showed in equation (2.1), the alcohol ROH (here is methanol) is esterified with Sulphur dioxide. And then, alkyl sulphite is oxidized by iodine, where water is consumed simultaneously. It is clear that one mole of iodine (I_2) is consumed for each mole of H_2O . By detecting the consumption of I_2 , the water amount can be calculated.

The Karl Fischer Titration system was supplied by Metrohm, Switzerland, including 860 KF Thermoprep, 803 Ti Stand and 852 Titrado. The test temperature was set at 160 °C and the rate of gas flow was set at 100 mL per minutes. Before measuring the water content by KFT, the residual acid needs to be removed from the surface of membranes. The tiamo TM 2.3 software was applied for recording the experiment data.

2.2.2 Local current density measurement device (current scan shunt)

In a fuel cell the local conditions differ. For example, due to the hydration or dehydration, phosphoric acid amount, concentration and phosphorus species will be different locally. This leads to an inhomogeneous mass conversion resulting in an inhomogeneous current production. In order to understand the dynamics of phosphoric acid in the MEAs, the current density distribution in an operating HT-PEFC should be measured.

With the current scan shunt, the current density distribution in HT-PEFCs can be measured [54]. The devices of current scan shunt series use a low ohmic shunt resistor for current measurement. The general principle of the current scan shunt follows the Ohm's law, as shown in equation (2.4).

$$I_m = \frac{U_t}{R} \quad (2.4)$$

I_m A current need to be measured

U_t V measured voltage

R Ω resistance of the shunt

However, due to the high temperature coefficient of resistance of copper which is used to build up the shunt, temperature compensation is necessary during the measurement. Finally, the signals (U_t) from the shunt resistors will be switched to an amplifier and evaluation electronic with Analog-to-Digital converter. The principle of current scan shunt is shown in Figure 2.4.

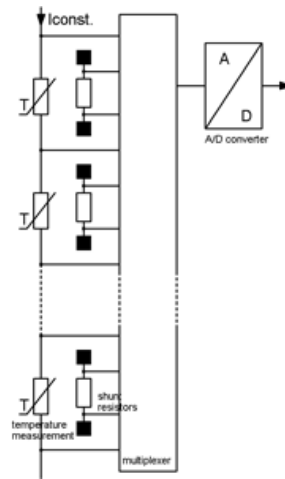


Figure 2.4: Principle of current scan shunt [54]

In this work, the current scan shunt has a resolution of 70×1 current measurement cells, 14×1 temperature measurement cells and an active area of 21.7 cm^2 . Figure 2.5 shows the image of the sensor plate of the current scan shunt, and Figure 2.6 gives the information of the sensor plate applied in a fuel cell. The plate was located in the middle of the graphite bipolar plate and the endplate at cathode of the cell.



Figure 2.5: The sensor plate of current scan shunt



Figure 2.6: The sensor plate in a test cell

2.2.3 Neutron radiography

In order to observe the transport phenomena or structural changes in a PEFC that operates at high temperature, some effective techniques have already been applied. For example, Maier et al. [55, 56] used synchrotron X-ray radiography to perform phosphoric acid distribution and re-distribution inside MEAs, which was considered as one of the first real operando attempts in operating high temperature PEFCs. In these studies, the re-distribution of the acid from the open cell voltage (OCV) condition to the load condition was analyzed on the basis of the in-plane direction of the cell, with membrane expansions and contractions on the micrometer scale explained by the hydration and dehydration of phosphoric acid in the membrane, which is highly affected by the water partial pressure within the cell.

Compared with X-rays which are attenuated based on a material's density, the attenuation of neutrons is not related to density. Some light materials such as boron absorb neutrons while hydrogen will generally scatter neutrons, and many commonly used metals (such as aluminum (Al), iron (Fe), copper (Cu)) with the mass attenuation coefficients of about 0.028, 0.108 and 0.101 $\text{cm}^2 \text{g}^{-1}$ respectively (see figure 1 in [57]) allow most neutrons to pass through them [58]. Figure 2.7 shows the basic principle of the neutron radiography. The neutron beams are first collimated and pass through the objects. Due to the different attenuation coefficient of the substance, different the signals can be acquired on the detector. In addition, for one kind of object, its linear attenuation coefficient can be used to calculate the linear density of the material combined with the final transmittance, which can be used to quantitatively analyze the phosphoric acid amount in the MEA by the contrast of hydrogen and deuterium. This makes neutron radiography a very good way to

detect the movement of hydrogen atoms or phosphoric acid molecules inside the MEAs of the HT-PEFC.

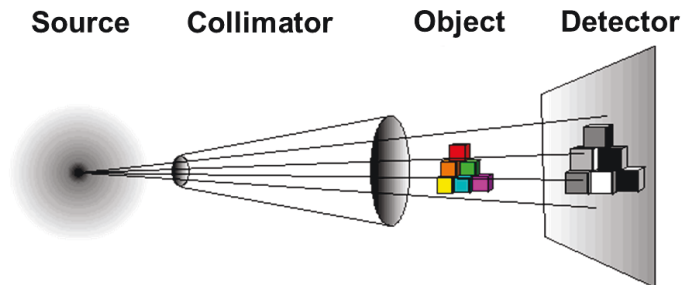


Figure 2.7: Schematic of Neutron radiography measurement.

Neutron radiography as a non-invasive and non-destructive method was applied to characterize an operando HT-PEFC, which has been widely used for the study of water transport properties of classical PEFCs and direct methanol fuel cells [59-65]. Boillat et al. [65] first proved the potential of using neutron radiography for the analysis of phosphoric acid distribution in high temperature PEFCs. Recently, a joint study between the Helmholtz Center Berlin and our group monitored hydrogen diffusion by using hydrogen-deuterium contrast neutron imaging on an operating high temperature PEFC with five meander-shaped channels for the flow field and square active area (49 cm^2) [66]. It revealed that the exchange rate from H-to-D is higher than that from D-to-H, and the gas exchange time at the gas inlet is shorter than that at the gas outlet.

In this work, Neutron radiographs were taken at the CONRAD2 beamline of the neutron source BER2 [67]. The neutron beam irradiated the cell in a through-plane direction, vertical to the membrane plane. All images were exposed for 0.5 s without a pause between the single exposures. A sCMOS camera (Andor "NEO"), in combination with a $20 \text{ }\mu\text{m}$ -thick Gadox scintillator, was used with an optical magnification optic that resulted in a pixel size of $11 \text{ }\mu\text{m}$ in each direction. More detailed information about this equipment can be found elsewhere [68]. The experimental setup of the operando neutron radiographic measurement of the cell is depicted in Figure 2.8. In this study, we used either hydrogen or deuterium as the anode reactant gas supply for the fuel cell's operation to

gain an imaging contrast for proton exchange processes. The data analysis was performed using ImageJ [69].

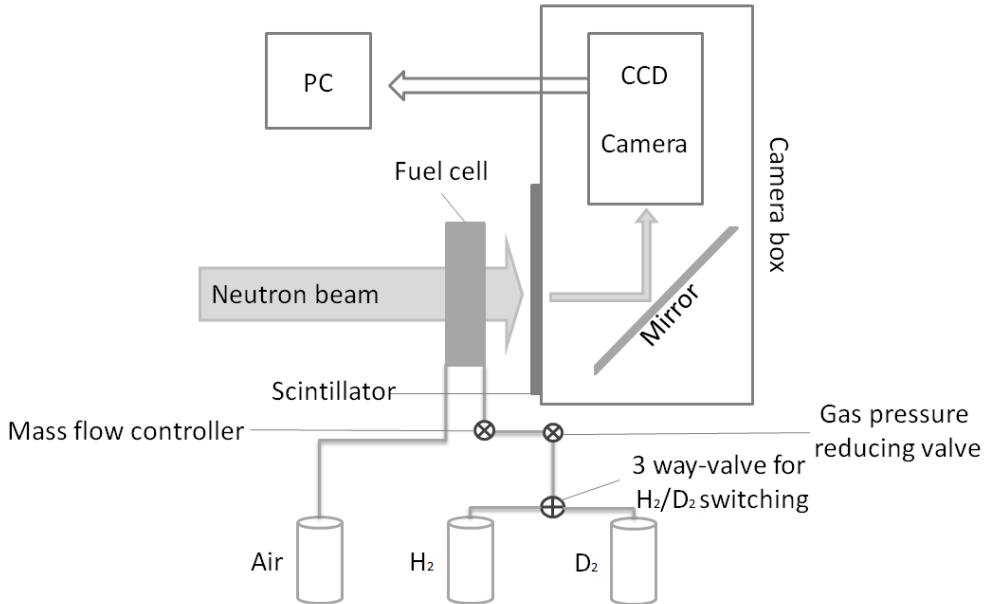


Figure 2.8: Experimental setup for this in-operando neutron radiographic measurement of the HT-PEFC. The tube length between 3 way-valve and gas pressure reducing valve is about 10 m, gas pressure inside the tube is about 3 bar; the tube length between pressure reducing valve and mass flow controller is about 1 m, gas pressure inside the tube is about 2 bar; the tube length between mass flow controller and cell inlet is about 1.5 m. gas pressure inside the tube is ambient pressure. The diameter of all the tubes is 0.4 cm.

3 Membrane doping

The proton conductivity of acid-doped PBI membranes depends strongly on the doping level and the water content. Asensio et al. [70, 71] measured the conductivity of anhydrous AB-PBI membranes doped with phosphoric acid. They found that the conductivities of doped membranes increased significantly with even slight increase of acid doping level. At 190 °C, the conductivity of AB-PBI doped with 69 wt.-% H_3PO_4 (corresponding 2.7 moles acid molecules per repeating unit of polymer), 68 wt.-% H_3PO_4 (corresponding 2.5 moles acid molecules per repeating unit of polymer), and 62 wt.-% H_3PO_4 (corresponding 1.9 moles acid molecules per repeating unit of polymer) were approximately 0.025, 0.014 and 0.004 S cm^{-1} respectively. Additionally, they also found that the conductivities of AB-PBI with a doping level of 3.0 moles acid molecules per repeating unit of polymer increased from about 0.040 to 0.052 S cm^{-1} when the relative humidity increased from 5% to 10% at 180 °C. The same trend of conductivity of phosphoric acid doped PBI membranes was also found by Ma et al. [72]. This indicates the significant role of the absorption of phosphoric acid (as well as water) in the membrane. Studies on the interaction between polymer chains and acid/water molecules are useful to understand this process in detail.

In this chapter, the influencing factors such as temperature, phosphoric acid concentration for doping and the crosslinked degree of the membranes on acid doping level and water uptake in the membrane is discussed. Also the swelling of the membranes after doping with a series of different amounts of phosphoric acid is depicted. Furthermore, the conductivity of membranes with different acid doping level was measured, and the HT-PEFCs based on PBI membranes with different acid doping level was tested.

In this chapter, the experimental work was mainly by Jianmin Xue and Yiwei Qiang, and a part of the content has been included in their bachelor thesis [73, 74].

3.1 Experimental setup

Before doping, a series of different concentrations of phosphoric acid solutions were prepared by phosphoric acid solution (known weight concentration of 85 wt.-%) and distilled water in a certain proportion. The weight concentration and molar concentration are listed in Table 3.1 below. The volume variations after mixing phosphoric acid and water were neglected here.

Table 3.1: Series of concentration of phosphoric acid solutions.

C_{wt} (wt.-%)	C_n (mol / L)	$W_{PA(85\ wt.-%)}(g):W_{H_2O}(g)$	$n_{(PA)} : n_{(H_2O)}$
15	1.66	3 : 14	0.03 : 1
25	2.92	5 : 12	0.06 : 1
35	4.34	7 : 10	0.10 : 1
45	5.94	9 : 8	0.15 : 1
55	7.74	11 : 6	0.22 : 1
65	9.8	13 : 4	0.34 : 1
75	12.11	15 : 2	0.55 : 1
85	14.67	--	1.04 : 1

The membranes used to investigate the temperature and acid concentration effects were Dopozol® membrane M40 supplied by Danish Power Systems. And the membranes used to analyze the crosslinked degree of the membranes were prepared by Professor Dr. Dirk Henkensmeier's group from KIST. The pure PBI membrane is a recast membrane of *m*-PBI, and the crosslinked membrane is cast by *m*-PBI crosslinked with DBX (dibromoxylene) from a DMAc (dimethylacetamide) solution [6]. The reaction mechanism between PBI and DBX is depicted in Figure 3.1 [75, 76].

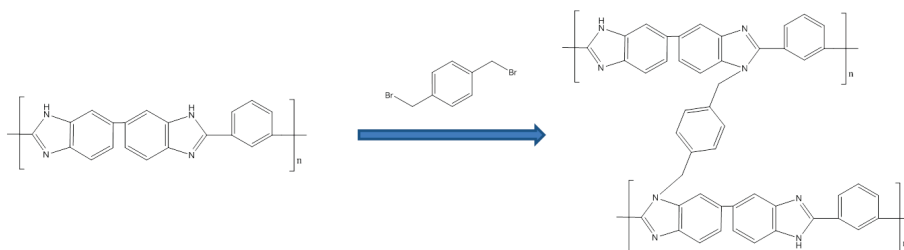


Figure 3.1: Crosslinking mechanism of PBI with DBX.

Before doping, all the membranes were dried at 150 °C for 30 minutes to remove the water inside the membranes. Then, the weight, thickness, length and width of membranes were measured. After that, the membranes were immersed in a phosphoric acid solution with a closed vessel in order to keep the acid concentration constant during the doping process. The parameters of the membranes mentioned before were measured again after doping was finished. The doping temperature (30 °C, 50 °C, 70 °C, 90 °C and 110 °C) was controlled by oil bath. The doping time for all the samples was \approx 18 hours. The doping process is shown in Figure 3.2.

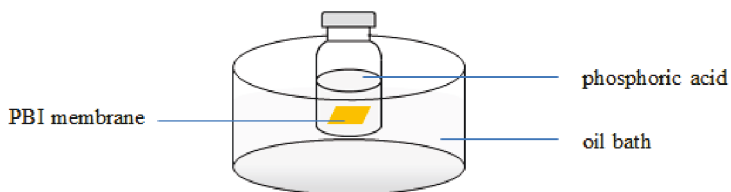


Figure 3.2: Schematic of doping membrane in closed vessel.

3.1.1 Definition and calculation of water uptake and phosphoric acid doping level

Water uptake (WU) and phosphoric acid doping level (ADL) was defined as the number of moles of water molecules and phosphoric acid molecules per mole of repeating unit of PBI membrane respectively. The total absorption (Q) was defined as the ratio of “weight increase of membrane after doping” to “weight of membrane in the dry state”. Acid concentration in polymer ($C_{(PA/H_2O)}$) was

defined as the number of moles of phosphoric acid molecules per mole water molecule in the membrane after doping. The following equations can be used to calculate the above items.

$$WU = \frac{W_{H_2O}/M_{H_2O}}{[W_{dry} \times (1-\theta)]/M_{mPBI}} \quad (3.1)$$

$$ADL = \frac{(W_{doped} - W_{H_2O} - W_{dry})/M_{PA}}{[W_{dry} \times (1-\theta)]/M_{mPBI}} \quad (3.2)$$

$$Q = \frac{W_{doped} - W_{dry}}{W_{dry}} \times 100\% \quad (3.3)$$

$$C_{(PA/H_2O)} = \frac{ADL}{WU} \quad (3.4)$$

W_{H_2O} /g	weight of water absorbed by membranes after doping process And measured by Karl Fischer titration
W_{dry} /g	weight of mPBI membranes at dry state
W_{doped} /g	weight of mPBI membranes after doping process
M_{H_2O} /g mol ⁻¹	molar mass of water, 18 g mol ⁻¹
M_{PA} /g mol ⁻¹	molar mass of phosphoric acid, 98 g mol ⁻¹
M_{mPBI} /g mol ⁻¹	molar mass of repeating unit of mPBI, 308 g mol ⁻¹ , as structure shown in Figure 2.1
θ /%	crosslinking degree of the membrane, as well as the weight percent of DBX in the crosslinked membrane. In the case of pure PBI, it is zero.

In this work, every sample was measured 3 to 5 times at the same conditions. The experimental results are presented as the mean values along with the error bars. The error bars were defined as the standard deviation of the data [77].

3.1.2 Definition and calculation of thickness and volumetric swelling

The thickness swelling of phosphoric acid doped PBI membranes was obtained by measuring the thickness of membranes before and after doping process. In addition, the length and width of the

membranes were also measured by the meter rule in order to calculate the volumetric swelling of membranes after doping process. Thickness swelling (T_s) was defined as the ratio of “the thickness change of membrane after doping process” to “the thickness of membrane in the dry state”. Similarly, volumetric swelling (V_s) was defined as the ratio of “the volumetric change of membrane after doping process” to “the volume of membrane in the dry state”. The thickness swelling and volumetric swelling can be calculated according to the following equations:

$$T_s = \frac{d_{doped} - d_{dry}}{d_{dry}} \quad (3.5)$$

$$V_s = \frac{(d_{doped} \times l_{doped} \times w_{doped}) - (d_{dry} \times l_{dry} \times w_{dry})}{d_{dry} \times l_{dry} \times w_{dry}} \times 100\% \quad (3.6)$$

where d_{doped} , l_{doped} , w_{doped} are the thickness, length and width of membranes after doping process while d_{dry} , l_{dry} and w_{dry} are the thickness, length and width of membranes in the dry state.

3.2 Results and discussion

3.2.1 Ternary system of m -PBI – H_3PO_4 – H_2O

The equilibrium of the m -PBI – H_3PO_4 – H_2O system can be expressed by a ternary phase diagram [78] as shown in Figure 3.3. The data were collected from own doping experiments and were generally in agreement with the data in the literature (see Figure 2 in [78]). In the Figure 3.3, x represents the molar fraction of the components in the system. The molar fraction of a single component is constant along a straight line parallel to a side of the triangle. A constant ratio between two components is found on a straight line going through a vertex of the triangle. The shaded areas represent the two-phase fields in contrast to the white areas related to full miscibility status. As it is showed in Figure 3.3, H_2O and H_3PO_4 are fully miscible; there is also full miscibility along the line between H_3PO_4 and m -PBI due to the full dissolution of m -PBI in highly concentrated phosphoric acid. The dissolution behavior of PBI in phosphoric acid will be discussed in chapter 4. On the other hand, the miscibility between m -PBI and H_2O is limited. A maximum 19 wt.-% of water uptake for m -PBI was gained at room temperature [6]. As illustrated in the ternary phase diagram of the m -PBI – H_3PO_4 – H_2O system, most of the data points concentrate in the regions of higher ratio

than 1:4 of $m\text{-PBI}:\text{H}_3\text{PO}_4$ and 1:4 of $m\text{-PBI}:\text{H}_2\text{O}$, which represent the high interaction between imidazole ring and phosphoric acid molecules compared with this between imidazole ring and water molecules, and the great effects on water absorption with phosphoric acid content in the membranes, respectively.

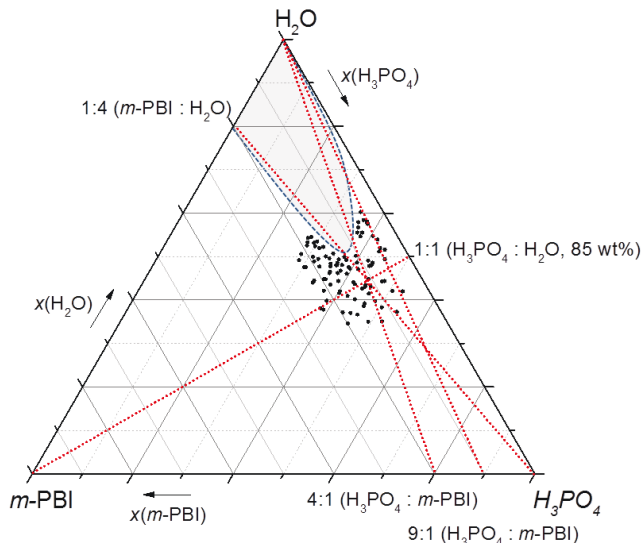


Figure 3.3: Ternary phase diagram of the $m\text{-PBI} - \text{H}_3\text{PO}_4 - \text{H}_2\text{O}$ system, composition is given in molar fraction, grey areas mark the two-phase field.

3.2.2 Doping temperature VS water uptake

As mentioned before, the water content can highly influence the proton conductivity of the PBI membrane doped with phosphoric acid. Li et al. [79] and He et al. [80] also found that the proton conductivity of PBI membranes doped with phosphoric acid increased with the relative humidity.

In order to investigate the water uptake of PBI membranes after doping with phosphoric acid, a series of doping temperature and concentration of acid solution were applied. The doping temperatures were set at 30 °C, 50 °C, 70 °C, 90 °C and 110 °C and controlled by oil bath. The concentration of acid solution for doping was listed in Table 3.1. All the samples were doped in

closed vessel in order to keep the concentration of acid solution stable. The amount of water uptake by *m*-PBI membranes was measured by KFT. The water uptake was calculated according to Equation (3.1).

Figure 3.4 shows an overview of the water uptake of *m*-PBI membranes after doping with a series of different concentrations of phosphoric acid solution at different doping temperature. Generally, a maximum value of water uptake is gained at 70 °C for every acid concentration solution. When the doping temperature is lower than 70 °C, the water uptake of the membranes seemingly stays stable with temperature, while the water uptake decreases with doping temperature from 70 °C to 110 °C. Taking the samples doped in 14.67 M (85 wt.-%) concentrated phosphoric acid solution as examples, the water uptake at low temperature (30 °C and 50 °C) is roughly 12.5 moles per repeating unit of polymer, and it slightly increases to 13.3 moles at 70 °C but then dramatically decreases to about 9 moles at 110 °C.

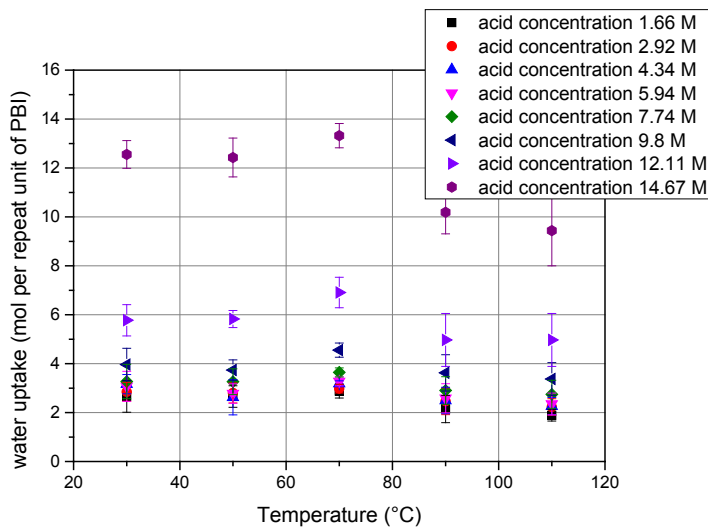


Figure 3.4: Water uptake as the function of doping temperature for *m*-PBI membranes.

3.2.3 Concentration of phosphoric acid solution VS water uptake

In addition, it is worth to note that the water uptake increases dramatically when the solution concentration is higher than 9.8 M in Figure 3.4. Figure 3.5 shows more directly, the effect on water uptake by the concentration of doping solution. As seen from Figure 3.4, the water uptake is almost constant in the low acid concentration ranging from 2-6 M in the solution for each doping temperature. Especially for 30 °C of doping temperature, the water uptake is about 3 moles per repeating unit of *m*-PBI. This is general agreement with the data in literature [6, 81] that a dry *m*-PBI membrane can absorb about 15-19 wt.-% water at room temperature, corresponding to 2.5-3.2 water molecules per repeating unit of the polymer. However, the water uptake increases rapidly when the solution concentration is higher than 8 M. The water uptake of the membranes doped in 14.67 M phosphoric acid solution is about 4 times higher than those doped in 1.66 M acid solution. This indicates that the phosphoric acid content in the membranes has great effect on water absorption [6]. The interaction between water and phosphoric acid molecules will be further discussed in detail in the next section.

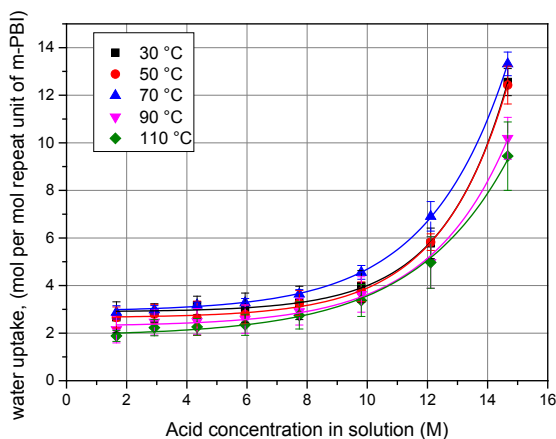


Figure 3.5: Absorption isotherm for water uptake for *m*-PBI membranes. The solid lines are fitted with the data.

3.2.4 Crosslinking degree of *m*-PBI membranes VS water uptake

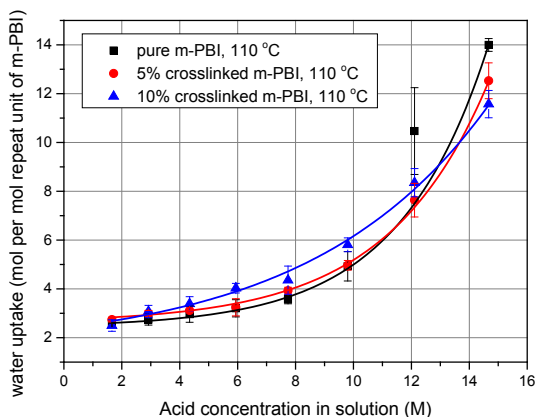


Figure 3.6: Water uptake of membranes with different crosslinked degree doped in a series concentration of phosphoric acid solutions in closed vessels at 110 °C. The solid lines are fitted with the data.

Figure 3.6 shows the water uptake of membranes with different crosslinked degree doped in a series concentrated phosphoric acid solutions in closed vessels at 110 °C. In this figure, the absorption isotherms can be divided into three segments: 0 – 4 M, 4 – 10 M and 10 – 16 M. In the range of 0 – 4 M acid concentration in solution, there is no obvious difference with the crosslinked degree of the membrane. At this low acid concentration range, the absorption of water and phosphoric acid molecules is relatively small compared to the adequate amount of active sites or spaces in the membranes. When the acid concentration (in the range of 4 – 10 M) goes higher, remarkably high water uptake by the high crosslinked PBI membrane was obtained. In this acid concentration range, the active sites on the polymer chains were more or less occupied by phosphoric acid molecules entirely. The water absorbed in this case mainly stored in the gaps among polymer chains. The addition of DBX in the polymer may increase the gaps which provide more space for water (as well as phosphoric acid) absorption. However, with increasing acid concentration, more acid and water would be absorbed generally. This requires high swelling or expansion of the membranes. But the swelling of the crosslinked membranes is restricted due to the strong bonding between polymer backbones by DBX. Thus, when doped in concentrated phosphoric acid solution (14.67 M), the water uptake of crosslinked membranes is lower than that of pure PBI

membranes. Furthermore, it can be noticed that the high crosslinking degree generally cause low water uptake when doped in 14.67 M acid solution.

3.2.5 Temperature and acid concentration effect on ADL

Phosphoric acid is the main proton conductor in a HT-PEFC, the content of which strongly effects the proton conductivity of the membrane. The formation of dynamic hydrogen bonding networks, in which protons can readily transfer by hydrogen bond breaking and forming processes, seems to be the determining step for high proton conduction. However, with low acid doping level, there is insufficient hydrogen bonding networks. As it is mentioned in chapter 2, the proton transport via hopping mechanism through the hydrogen bonding networks is much faster than the transport via vehicle mechanism by a water or phosphoric acid molecule. In the case of low acid doping level, the proton transfer between one hydrogen networks to another hydrogen networks is relatively slow via vehicle mechanism, which limits the whole transfer speed in membrane and results in low proton conduction.

Here, the acid doping level of membranes is indirectly measured by measuring water uptake. It can be calculated according to the equation (3.2).

The acid doping level (ADL) of membranes after doping at a series of doping temperature and concentration of acid solution was obtained. Figure 3.7 shows the ADL of pure *m*-PBI membranes as a function of the doping acid concentration in solution at several doping temperatures. Comparing the water uptake shown in Figure 3.5, in low acid concentration range (2 -6 M), the acid doping level increases with the acid concentration while the water uptake is stable. This indicates that the interaction between phosphoric acid and polymer is stronger than it is between water and polymer. As mentioned before, phosphoric acid has the priority to occupy the active sites for absorption on the polymer chains. In the case of low acid concentration, the active sites on the polymer chains are not fully occupied by phosphoric acid molecules. With the increase of acid concentration, more active sites are occupied by phosphoric acid molecules, while the water molecules disconnect with polymer chains but reconnect with phosphoric acid molecules. Thus, it showed an increase of acid doping level but a constant water uptake. When the acid doping level exceed 4 moles per repeating unit of *m*-PBI (there are 4 active sites (2 sites of =N- will be protonated by phosphoric acid molecules, and the other 2 sites of -NH- will be hydrogen bonded with phosphoric acid molecules

as explained in [82]) per repeating unit of *m*-PBI), the absorption of phosphoric acid is no longer restricted by the number of active sites on the polymer chains. The exceeding phosphoric acid molecules will indirectly connect with polymer chains by the hydrogen bonded phosphoric acid molecules (which directly bond with N or NH groups on polymer chains as shown in Figure 2.2 (b)). The hydrogen bonded phosphoric acid molecules provide more opportunities for absorbing free phosphoric acid molecules. This results in a very fast increase of acid doping level in high acid concentration as shown in Figure 3.7.

On the other hand, generally, the acid doping level of the membrane increases with the doping temperature. However, in the case of low acid concentration (0 – 6 M), the temperature effect is not evident; while a significant difference of the acid doping level can be observed at high acid concentration. As it is shown in Figure 3.7, about 2 moles per repeating unit of polymer of acid doping level was gained between 30 °C and 110 °C.

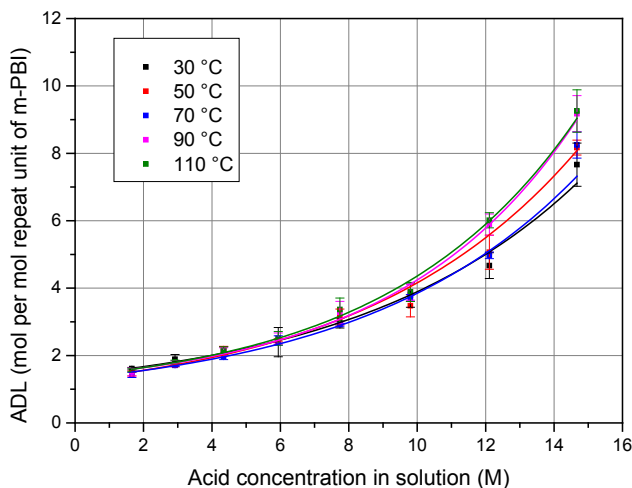


Figure 3.7: Acid doping level of pure *m*-PBI as a function of acid concentration in solution at a series doping temperature. The solid lines are fitted with the data.

3.2.6 ADL of crosslinked *m*-PBI membranes

Figure 3.8 shows the acid doping level of membranes with different crosslinked degree doped in a series concentrated phosphoric acid solutions in closed vessels at 110 °C. Comparing the results of acid doping level and water uptake (shown in Figure 3.6) of crosslinked *m*-PBI membranes, similar absorption isotherms of phosphoric acid was found with them of water. In the range of 0 – 4M of acid concentration, the difference of acid doping level of crosslinked or non-crosslinked membranes is very small; in the range of 4 – 10 M acid concentration, the crosslinked membranes had higher acid doping level; and when the acid concentration is higher than 10 M, the pure membranes absorb more phosphoric acid. The explanation of the results of water uptake can be also applied here to explain the effect of crosslinked degree on acid doping level.

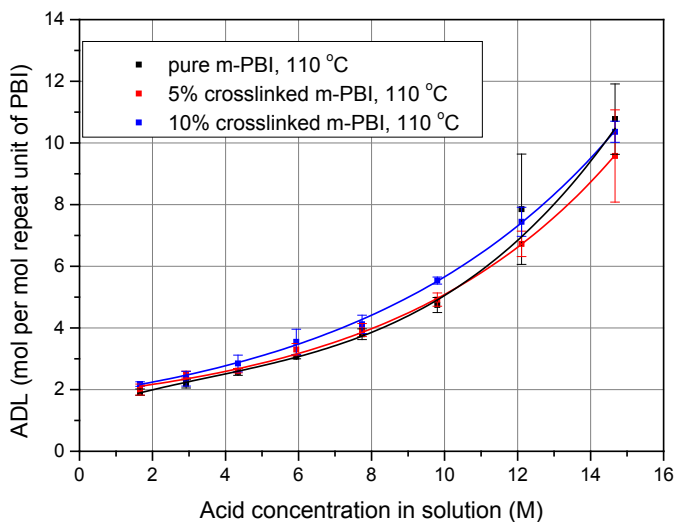


Figure 3.8: The acid doping level of crosslinked *m*-PBI and non-crosslinked *m*-PBI membranes as the function of acid concentration in solution at 110 °C. The solid lines are fitted with the data.

3.2.7 Acid concentration in polymer

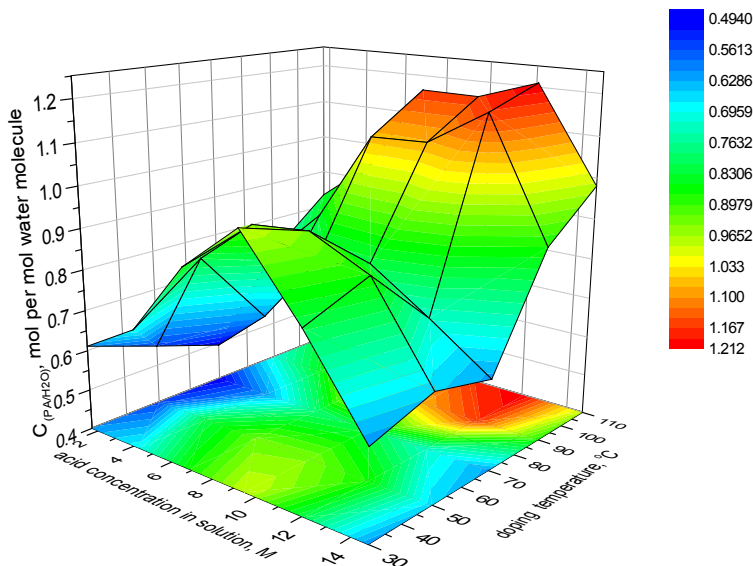


Figure 3.9: The 3D mapping surface of acid concentration in polymer of pure *m*-PBI regarding the acid concentration in solution and doping temperature.

The acid concentration in polymer ($C_{(PA/H_2O)}$) was defined as the number of moles of phosphoric acid molecules per mole water molecule in the membrane after doping. It refers to the equilibrium of phosphoric acid and water in membranes and can be calculated by the equation (3.4). Figure 3.9 shows the acid concentration in polymer of the pure *m*-PBI membranes doped in a series concentration of acid solutions at various doping temperature. It is obvious that at 70 °C, doped membranes had the lowest acid concentration in themselves despite the concentration of doping solutions. This is due to the highest amount of water content at this temperature, which was discussed in the section of 3.2.2. When discussing the effect of acid concentration in solution, the highest acid concentration in polymer can be obtained in the range of 8 – 12 M of acid in solution at all doping temperature. This phenomenon was also found in the literature [70, 83]. In [70], Asensio et al. found that, with the increase of acid concentration in solutions, the acid concentration in polymers first increased and then decreased for both AB-PBI and *m*-PBI membranes. In [83], Glipa et

al. immersed m-PBI membranes into phosphoric acid solution for 1 h and 16 h separately. They found that the acid concentration in polymer was similar to the acid concentration in solution when the membranes were only immersed for 1h. But in the case of 16 h immersion, the acid concentration in polymer was always higher than that in solutions for the acid concentration range of 0 -10 M in solution. Furthermore, the acid concentration in polymer also first increased and then decreased a little bit with the acid concentration in solution. However, referring to the data from Li et al. [79, 84], the acid concentration in polymer first increased and then kept more or less stable when the acid concentration in solution was in an range from 3 M to 12 M.

In this work, the phenomenon of acid concentration in polymer increasing first and then decreasing was also found with the crosslinked membranes. In the case of pure m-PBI, this is due to the faster phosphoric acid absorption increase from about 1.5 M ADL at 1.66 M of acid solution to about 3.4 M ADL at 7.74 M of acid solution, while water absorption increases by about 0.5 M, as shown in Figure 3.7 and Figure 3.5 respectively. Simultaneously, a faster water uptake of nearly 6 M from 12.11 – 14.67 M of acid solution was obtained, while it was only 3 M for phosphoric acid adsorption.

In addition, when the membranes doped in 1.66 M concentration of acid solution (i.e. $n(\text{PA}) : n(\text{water}) = 0.03 : 1$), the acid concentration in membrane is higher than the acid concentration in solution as shown in Figure 3.9. This indicates the strong interaction between phosphoric acid and polymer chains.

3.2.8 Dimension variations of pure *m*-PBI

The dimension variations of membrane after doped with phosphoric acid are associated with the mechanical strength. It was easy to observe that the membranes become softer with the total absorption increase. This indicates a loss of mechanical strength of the membranes after being doped with phosphoric acid. According to Glipta et al. [83] and Brooks et al. [81], the loss in mechanical properties in doped PBI was explained by the separation of PBI backbones by phosphoric acid and water molecules, which results in the reduction in van der Waals forces and hydrogen bonding interactions between polymer chain.

Additionally, the durability and lifetime of HT-PEFCs are influenced by the different dimension variations at in-plane and through-plane direction (i.e. thickness swelling and area swelling

respectively). For example, in the case of different membranes at the same doping level, one membrane has higher swelling than others, which means this membrane will have higher shrinkage during dehydration or phosphoric acid loss. Zhang et al. [85] demonstrated that the shrinking and cracking of membranes (e.g., Nafion) in classical PEFC accelerates the gas crossover, resulting in dire consequences to the cell's performance. Additionally, crossover also compromises safety due to the exothermic combination of H_2 and O_2 on Pt catalyst generating local hot spots that lead to pinholes, which in turn accelerates gas crossover, initiating a destructive loop of increased crossover and membrane degradation. Furthermore, the higher shrinkage produces more tension at the boundary between membrane and gaskets. During cycling test (hydration/dehydration), membranes at the boundary will very easily break, which will cause high gas crossover. Figure 3.10 shows the failures of membrane at the boundary between membrane and gaskets. Thus, the studies on the dimension variations of membranes after doped with phosphoric acid are quite important. Equation (3.5) and (3.6) can be used to calculate the dimension variation of PBI membranes.

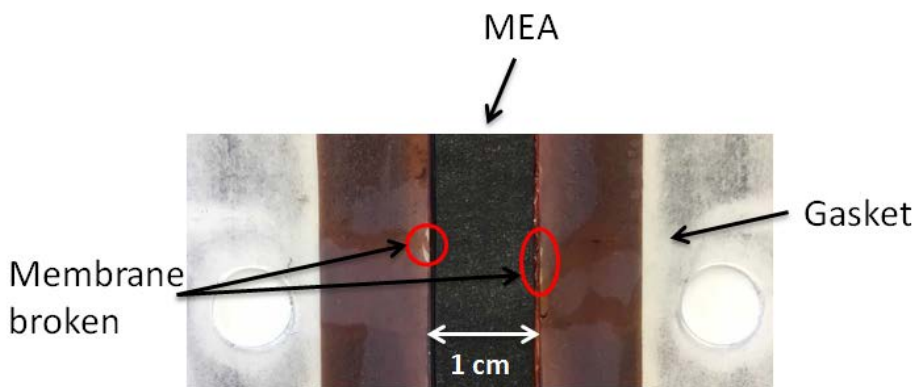


Figure 3.10: The failures of membrane at the boundary between membrane and gaskets.

Figure 3.11 shows the thickness swelling of pure *m*-PBI membrane after doping with phosphoric acid as a function of acid doping level and water uptake. As shown, the thickness of *m*-PBI membranes has been greatly enlarged after being doped with phosphoric acid. At the end, nearly 120 % thickness swelling was gained. Comparing Figure 3.11 (a) and (b), it was found that, in a range of 20% - 60% of thickness swelling, acid doping level is in the range of 1.5 – 3 moles per repeating unit of *m*-PBI, but the water uptake of the acid doped membranes is almost constant with 3 moles per

repeating unit of *m*-PBI. This means the swelling of *m*-PBI membranes resulted primarily from the doping acid in low acid doping level. The phenomenon was also found in the literature [83], in which the total volume swelling is about 80-118 % with 55-90 % due to the doping acid and 25 -30 % due to the absorbed water in an acid doping level range from 3 – 5 moles per repeating unit of *m*-PBI. In a thickness swelling range from 60% - 110%, the thickness swelling should be caused by a collective effect of absorbed phosphoric acid and water.

In addition, as shown in Figure 3.11 (a), in an acid doping level range from 1.5 to 5, the value of thickness swelling increased almost linearly with the increase of acid doping level by 25% to 80%. In an acid doping level range from 5 – 9, the thickness swelling increased more and more slowly with the increase of acid doping level. In this range, only 30% of thickness swelling was acquired.

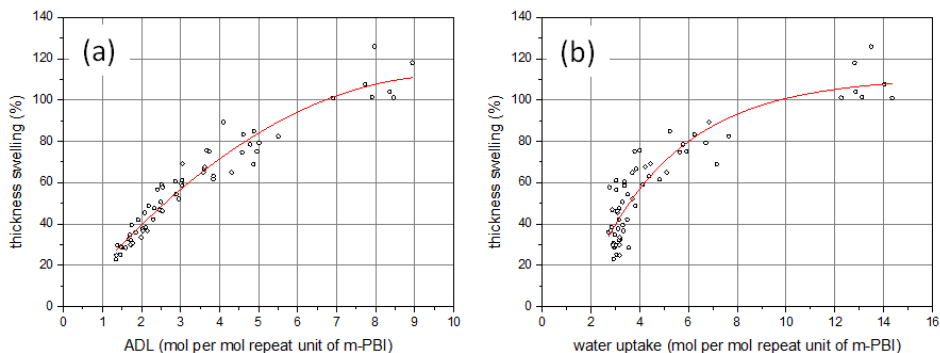


Figure 3.11: The influence of acid (a) and water uptake (b) on the thickness swelling for acid doped *m*-PBI membranes.

3.2.9 Dimension variations of crosslinked *m*-PBI membranes

Figure 3.12 shows the volume swelling of crosslinked/non-crosslinked *m*-PBI membranes as a function of acid doping level. It can be seen that the volumetric swelling of membranes increases almost proportional to the increase of the acid doping level. The volumetric swelling of 10 % crosslinked PBI membranes is about 50 % to 250 % in the range of acid doping level from 2 to 10 moles per repeating unit of polymer. The corresponding increases in the thickness and area are 35-135 % and 13-45 %, respectively. This indicates that the dimension increase of membranes takes

more significantly in thickness than in area. Also it demonstrates anisotropy of PBI membranes at in-plane and through-plane direction.

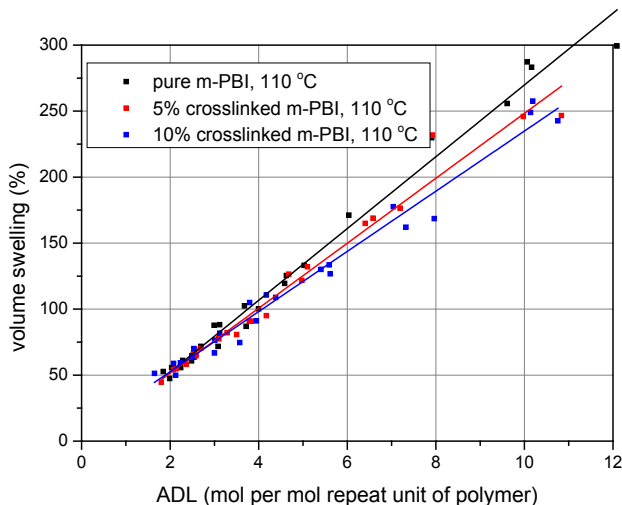


Figure 3.12: Volumetric swelling of PBI membranes with different crosslinked degree as a function of acid doping level.

Furthermore, the volumetric swelling of non-crosslinked PBI and crosslinked PBI membranes is quite close in a range of acid doping level from 2 to 4 moles per repeating unit of polymer. When acid doping level continues to increase, the volumetric swelling of pure PBI is larger than the crosslinked PBI membranes. This can be due to the mobility of polymer chains of pure PBI membranes is better than crosslinked membranes. Moreover, the existence of DBX in PBI membranes can bond part of the polymer chains and restrict the expansion of the membrane. This proved again the results of acid doping level and water uptake of membranes affected by crosslinked degree showing in Figure 3.6 and 3.8.

On the other hand, it is interesting to find that the thickness swelling of crosslinked PBI membranes is higher than this of non-crosslinked PBI membranes shown in Figure 3.13. Moreover, with higher crosslinked degree, the membranes have higher thickness swelling. Wannek et al. [5] found that the acid distribution of membranes in the steady state as well as the cell performance were independent of how the acid was introduced (via pre-doping of the membrane or GDEs). Maier et al.

[55] observed roughly 20 % thickness swelling of AB-PBI membrane in an operating HT-PEFC when the operation condition changed from OCV to 140 mA cm⁻² current density. However, the influence of different swelling on cell performance, membrane mechanical integrity and structure of catalyst layer at the interface of catalyst and membrane is not known yet.

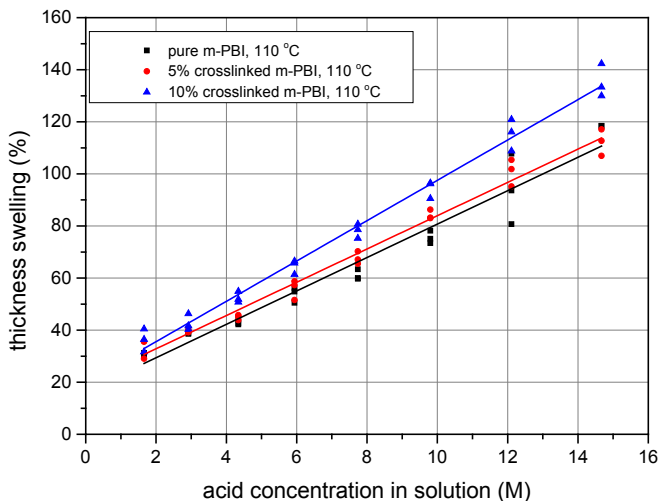


Figure 3.13: The thickness swelling of crosslinked/non-crosslinked m-PBI membranes as a function of acid concentration in solutions.

3.2.10 Single cell performance

The cell performance is highly influenced by the phosphoric acid content in the MEA of a HT-PEFC. When talking about the acid content in membranes, the improved acid content increases the proton conductivity of membranes. However, the high acid uptake in the membranes causes low mechanical strength and high gas permeability [6], which has a strong impact on the durability and lifetime of HT-PEFCs. The mechanical strength of PBI membranes decreases from 100 MPa to 10 MPa with an increase of acid doping level from 0 – 5 moles per repeating unit of the polymer at 180 °C in nitrogen atmosphere [86]. Additionally, the gas permeability increases by 2-3 orders of

magnitude in the acid doping level range from 0 - 6 moles per repeating unit of the polymer at 150 °C.

On the other hand, nevertheless how the cell is assembled, the catalyst layer of the cell would have some amount of phosphoric acid due to the phosphoric acid redistribution [5]. Maier et al. [87] prepared the MEAs by assembled un-doped membrane with pre-acid doped gas diffusion electrodes (GDEs). They estimated that after the assembly the acid doping level in the membrane was about 2 molecules phosphoric acid per repeating unit of the polymer. The rest phosphoric acid existed in the catalyst layer. In addition, they found that the total resistance of the MEAs decreased with the increase of current density. Kwon et al. [88] assembled MEAs with doped membranes and dry GDEs. They found that after assembly at room temperature a total amount of about 40 % phosphoric acid moved into catalyst layers for cathode and anode. By comparing the flooded cell (with 50% phosphoric acid in catalyst layers) and non-flooded cell (with 40% phosphoric acid in catalyst layers), they further found that the charge transfer resistance of the flooded cell was larger than that of the non-flooded cell. Chen et al. [89] investigated the charge transfer resistance of fuel cells as functions of current density and operating temperature. They found that the charge transfer resistance decreased with the increase of the temperature and current density. The effect of temperature on charge transfer resistance was also found by Zhang et al. [90]. Souise et al. [91] reported the current density at 0.4V of HT-PEFCs as a function of phosphoric acid loading in catalyst layers at 150 °C. They demonstrated that the current density increased between a volume fraction of 5% and 30% of phosphoric acid in catalyst layers. The optimum current density was estimated to be reached between 30% and 55%, and for the phosphoric acid content in catalyst layer above 55% the current density started to fall caused by the flooding effect of phosphoric acid.

In general, a high phosphoric acid content is beneficial for the electrochemical reaction and the proton transfer in the catalyst layer and the proton conductivity in the membrane; however, on the other hand, the high phosphoric acid content will result in loss of mechanical strength and high gas crossover, and the excess phosphoric acid in the catalyst layer can block the pathway of reactant gases to reach the catalyst surface, as well as the flooding effect.

In this work, several cells were assembled with the Fumapem® AM-55 membranes from Fumatech with different total absorption and operated on a standard test-rig built up by IEK-3, Forschungszentrum Jülich. The values of the total absorption which can be calculated by equation

(3.3) of membranes after doping with phosphoric acid are displayed as the weight percentage due to the indistinguishable acid and water uptake. Moreover, the structure of this membrane is not known due to commercial confidentiality. The relation between acid doping level and total absorption of the Fumapem® AM-55 membranes can be expressed by the empirical equation (3.7) shown below according to Korte et al. [92].

$$ADL = (0.0406 \pm 0.0005) \times Q - (0.45 \pm 0.1) \quad (3.7)$$

Based on this equation, the relation of ADL and Q can be plotted as shown in Figure 3.14.

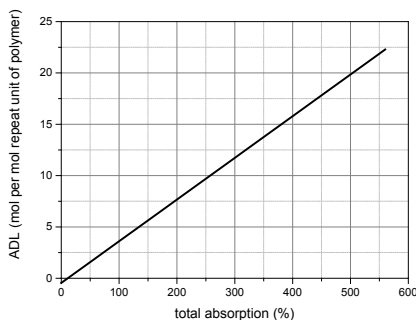


Figure 3.14: Acid doping level (ADL) of Fumapem AM-55 at 110 °C as a function of the total absorption (Q) of the polymer.

The detail preparation process of doped membranes and GDEs is shown in the section of 5.1. The Platinum loading was $1.00 \pm 0.05 \text{ mg cm}^{-2}$. The test temperature was 160 °C. The active area of MEA was 17.64 cm². Hydrogen was fed to anode and air was fed to cathode and stoichiometry was set as 2/2. The dew point of hydrogen and air were -50 °C and -58 °C respectively. Before the polarization curve measurement, a break-in process [77] was applied.

As is shown in Figure 3.15, the cell with a total absorption of 423 wt.-% of membrane (corresponding an acid doping level of about 16.6 M) had the highest performance in general. With the decrease of the acid doping level, the cell performance decreased. However, it is worth to notice that the open cell voltage (OCV) of cell with the highest acid doping level is lowest for a value of only 0.75 V. It was reported [93] that the OCV can be affected by the gas-crossover through membranes, solubility of gaseous reactants in phosphoric acid in the catalyst layers. According to this literature, OCV of a HT-PEFC was estimated in a range of 0.96 to 1.00 V. In this work, the OCV of the cell with a

total absorption of 423 wt.% of membrane is less than the estimated value. Based on the statements above, one possible reason for the low OCV value was recognized to be due to the high gas permeability with high acid doping level; the other possible reason was the membrane failure (pinholes or breaks as shown in Figure 3.10) causing by the loss of mechanical strength with high acid doping level.

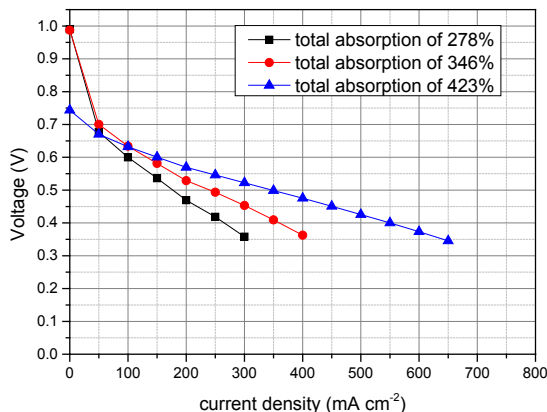


Figure 3.15: The polarization curves of HT-PEFCs based on m-PBI membranes with different acid doping levels.

3.3 Summary

The present chapter discussed the effect of doping temperature, acid concentration in solutions and crosslinked degree of membranes on the phosphoric acid absorption and water uptake of PBI membranes. The following results were observed:

- The water uptake of the membrane slightly increased in a range of 30 – 70 °C but dramatically decreased in the range of 70 – 110 °C, while the acid doping level increased in the whole range of doping temperature.
- The acid doping level and water uptake increased in the whole range of acid concentration in solutions. The water uptake is independent of acid absorption in an acid concentration range of 0 – 6 M. But in the case of high acid concentration in solutions, the water uptake is associated with the acid absorption.

- Crosslinking with DBX of PBI membranes generally benefit to the acid doping level and water uptake. The restriction of volumetric swelling makes the acid absorption and water uptake of crosslinked membranes lower than these of non-crosslinked membranes at high acid concentration.
- The cell performance increased with the total absorption of phosphoric acid of membranes.

4 Dissolution of PBI membranes in phosphoric acid solution

Despite its advantages, the lifetime of a HT-PEFC is a major concern for the commercialization. The main degradation modes of HT-PEFCs are listed in Table 4.1[94]. In the case of membrane thinning, there are two mechanisms: chemical degradation and physical degradation. For the chemical degradation, it was proved that the $\text{HO}\cdot$ and $\text{HOO}\cdot$ free radicals which were suggested to be produced by the incomplete reduction of oxygen on the cathode side of fuel cells can attack the polymer chains of PBI and cause the polymer backbone to break at the benzene rings [95]. However, this work was performed in a simulated environment of HT-PEFCs. In the case of classical PEFCs, Panchenko et al. [96] and Vogel et al. [97, 98] proved the existence of the free radicals by in-situ electron spin-resonance spectroscopy (EPR) measurement of classical PEFCs. However, Vogel et al. [97] demonstrated that the degradation of Nafion membrane in classical PEFCs was not dominated by the attack of free radicals. Furthermore, in the case of HT-PEFCs, the existence of the free radicals is still not proven. On the other hand, as mentioned in section 3.2, phosphoric acid and PBI membrane can be fully miscible, which is suggested to be the reason of physical degradation for membrane thinning. In addition, the dissolved PBI can migrate to the catalyst layers and reduce the electrochemical surface area of the catalyst [99].

Table 4.1: Main degradation modes in HT-PEFCs [94].

component	cause	effect
Membrane	Pinhole formation	Gas crossover
	Membrane thinning	Gas crossover, shortcuts
	PA evaporation from membrane	Decrease of proton conductivity
Electrodes	Pt particle agglomeration	Decrease of reaction kinetics
	Pt dissolution/alloy dissolution	Decrease of reaction kinetics
	PA evaporation from catalyst layer	Decrease of reaction kinetics
	Carbon corrosion	Decrease of reaction kinetics
GDL	GDL corrosion	Increase of mass transport resistance
Note: PA Phosphoric acid, Pt Platinum, GDL Gas diffusion layer		

In this chapter, the dissolution behaviors of AB-PBI and crosslinked AB-PBI in concentrated phosphoric acid solutions will be investigated. The experimental work was mainly performed by Xi Wu, and a part of the content has been included in her bachelor thesis [100].

4.1 Experimental setup

4.1.1 Materials

In this work, the AB-PBI membranes and crosslinked AB-PBI membranes were supplied by FuMA-Tech. The various concentrated phosphoric acids were prepared by the phosphoric acid with a concentration of 85 wt.-%. Phosphoric acid with a concentration of 100 wt.-% was prepared by evaporating the water of 85 wt.-% phosphoric acid. The 90 and 95 wt.-% phosphoric acid were diluted by 100 wt.-% phosphoric acid with distilled water. The concentration of various phosphoric acids was determined by the density of the solution as shown in table 4.2 [101], and confirmed by Karl Fischer Titration. In order to remove all the phosphoric acid in the remaining membranes after dissolution test, sodium hydroxide (NaOH) solution with a concentration of 1 mol/L was applied to wash the doped membranes.

Table 4.2: Density of phosphoric acid (over 85 wt.-%) [101].

Concentration		Temperature, °C							
		25	30	40	50	75	100	125	150
H ₃ PO ₄ /wt.-%	P ₂ O ₅ /wt.-%	Density (g cm ⁻³) at indicated							
85.61	62	1.693	1.689	1.681	1.673	1.653	1.633	1.613	1.593
88.37	64	1.725	1.722	1.714	1.706	1.686	1.667	1.647	1.627

91.13	66	1.758	1.754	1.746	1.739	1.719	1.700	1.681	1.661
91.58	66.33	1.763	1.760	1.752	1.744	1.725	1.706	1.686	1.667
93.89	68	1.791	1.787	1.779	1.772	1.753	1.734	1.715	1.696
96.65	70	1.823	1.820	1.812	1.805	1.786	1.767	1.748	1.73
99.41	72	1.856	1.852	1.845	1.838	1.819	1.801	1.782	1.764
100.00	72.43	1.863	1.859	1.852	1.845	1.826	1.808	1.789	1.771
102.17	74	1.889	1.885	1.878	1.871	1.852	1.834	1.816	1.798
104.94	76	1.921	1.918	1.911	1.903	1.886	1.868	1.850	1.832

4.1.2 Determination of the weight loss of membranes after dissolution

In this work, the remaining membranes after dissolution test were washed by NaOH solution first, and then washed by distilled water 3 times under the temperature of 80 °C, and finally dried at 150 °C in an oven for half an hour. For all the washing by NaOH solution, the 3 times subsequent washing by distilled water was needed. In general, the weight loss of membranes after dissolution test can be calculated as following:

$$\delta = \frac{W_0 - W_1}{W_0} \times 100\% \quad (4.1)$$

δ % weight loss of membranes after dissolution;

W_0 g weight of initial membranes at dry state;

W_1 g weight of membranes after dissolution test at dry state

NOTE: “initial membrane” means the membrane was not used for any treatments (doping, heating or washing et al.)

However, the interaction between membranes and NaOH solutions is not taken into account. In order to eliminate the impact of NaOH solutions on membranes, the initial membranes were first washed by NaOH solutions and distilled water separately. The weight loss of initial membranes washed by NaOH solutions and distilled water are presented in Table 4.3.

Table 4.3: The weight loss of initial membranes washed by NaOH solutions and distilled water.

Membrane type	Washed by	Weight loss – mean (%)	Weight loss – standard deviation (%)
AB-PBI	H ₂ O	6.48	0.30
AB-PBI	NaOH	6.87	0.04
Crosslinked AB-PBI	H ₂ O	0	0
Crosslinked AB-PBI	NaOH	0	0

As can be seen from Table 4.3, the weight loss of AB-PBI washed by distilled water is about 6.48 % with a standard deviation of 0.30 %, while the value of AB-PBI washed by NaOH solutions is about 6.87 % with a relatively small standard deviation of 0.04 %. The tiny difference of the weight losses indicates that NaOH causes no significant effect on the weight losses of AB-PBI membranes. The lost weight of AB-PBI membranes washed by NaOH solutions or distilled water was attributed to the residual solvent of membrane casting process. It is also interesting to note that there is no obvious weight loss of crosslinked AB-PBI membranes after washing by NaOH solution and distilled water.

In order to make sure that the NaOH solution is a better detergent for removing the phosphoric acid in a doped membrane, several pieces of membranes with same doping level were prepared and washed by NaOH solution and distilled water separately. The membranes were immersed in 85 wt.-% phosphoric acid at 110 °C for 20 minutes in a closed vessel. Half of the membranes were washed by

distilled water for 3 times, and the other half were washed by NaOH solution first and subsequently by distilled water for 3 times as mentioned before. The weight losses of doped membranes after washing are shown in the Table 4.4.

Table 4.4: The weight loss of doped membranes washed by NaOH solutions and distilled water.

Membrane type	Washed by	Weight loss – mean (%)	Weight loss – standard deviation (%)
AB-PBI	H ₂ O	9.67	1.65
AB-PBI	NaOH	14.71	0.23
Crosslinked AB-PBI	H ₂ O	6.37	1.74
Crosslinked AB-PBI	NaOH	7.70	0.10

As shown in Table 4.4, the weight loss of membranes washed by NaOH solution is always higher than it of membranes washed by distilled water. This indicates that some amount of phosphoric acid in doped membranes is very hard to remove by water. Furthermore, from the standard deviation of the weight loss, it can be deduced that NaOH solution washing process can produce more stable and reliable data for detecting the dissolution behavior of membranes in phosphoric acid. On the other hand, comparing the weight loss of initial membranes and doped membranes, the higher weight loss of doped membranes indicates that slight dissolution of membranes occurred during the doping process.

Thus, the equation (4.1) should be calibrated as following:

$$\delta' = \frac{W_0' - W_1}{W_0} \times 100\% \quad (4.2)$$

δ' % weight loss of membranes caused by dissolution;

W_0 g weight of initial membranes at dry state;

W'_0 g weight of initial membranes after washing by NaOH solution;

W_1 g weight of membranes after dissolution.

4.2 Results and discussions

4.2.1 Dissolving membranes in open vessel

In this section, membranes were first washed by NaOH solution to eliminate the effect by residual solvent inside the membranes, and then they were immersed into phosphoric acid solution with a starting concentration of 85 wt.-% in open vessels under various temperatures. Due to the open system, the concentration of phosphoric acid solution would increase with time. The dissolution process was observed at different periods of time.

Figure 4.1 shows the dissolution phenomenon of AB-PBI membrane in phosphoric acid at 90 °C. The membrane which immersed under the temperature of 90 °C did not dissolve thoroughly in a relatively long period of time, approximately one week. The remaining polymer of the undissolved membrane was gained through filtration, washing and drying process, as shown in Figure 4.1 (d). It is clear that the membrane broke into very small pieces. The dissolution process can be seen from Figure 4.1 (a) – (b) and depicted as follows: the membrane became swollen gradually, then broke into big pieces after 2 days and broke into very small pieces eventually.

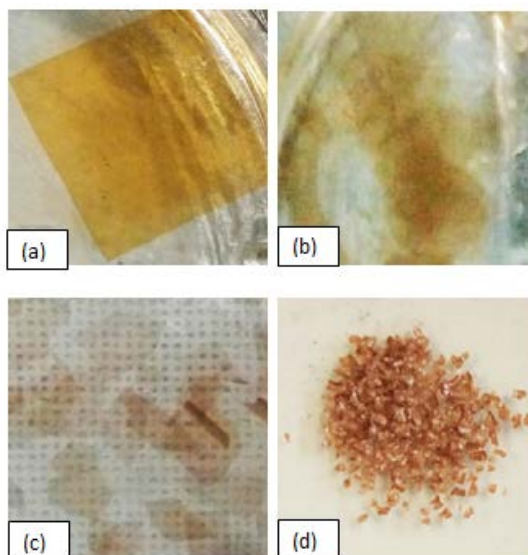


Figure 4.1: The photographs of AB-PBI dissolution process at 90°C (a) the swollen state of the membrane after 4hours (b) the state of the membrane at the breaking time, i.e. 24h (c) the state of the membrane breaking into small pieces after 2 days (d) the state of the dried membrane after 5 days.

In the case of 110 °C, the dissolution phenomenon of AB-PBI membrane was similar as at 90 °C. However, the membrane at 110 °C dissolved into phosphoric acid solution completely as shown in Figure 4.2 (d). The time for membrane break down and dissolving completely is much shorter than membrane at 90 °C. It took the membrane 4.5h and 24h to break down and dissolve completely, as shown in Figure 4.2 (b) and (d) respectively.

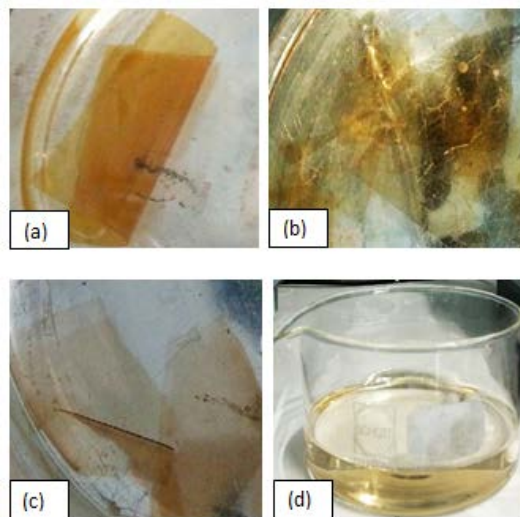


Figure 4.2: The photographs of AB-PBI dissolution process at 110°C (a) the swollen state of the membrane after 1.5h (b) the state of the membrane at the breaking time, i.e.4.5h (c) the swollen states of every broken pieces of the membrane after 5h (d) the state of the solution with the membrane completely dissolving.

The dissolution process of membranes which dissolved at 130°C is almost the same as membranes dissolved at 110°C, besides the shorter breaking and complete dissolution time, which is not shown here.

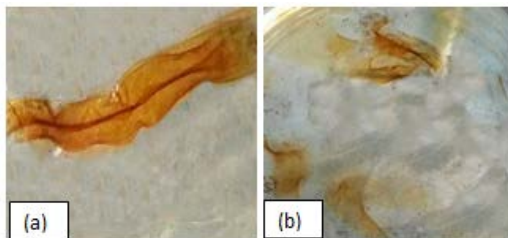


Figure 4.3: The photographs of AB-PBI dissolution process at 160°C (a) the swollen state of the membrane after only 2min (b) the state of the membrane at the breaking time, i.e. 10min.

For the AB-PBI membrane at 160 °C, the dissolution phenomenon is somewhat different from the membrane at 110 °C. The membrane became particularly soft as soon as immersed in phosphoric acid solution and broke rapidly as shown in Figure 4.3 (a) and (b) respectively. The breaking time of

the membrane at this temperature was only 10 minutes, which is much shorter than the membrane at 110 °C.

In order to quantify the dissolution behavior of AB-PBI membranes at various temperatures, the breaking time and dissolution time of membranes were recorded as shown in Table 4.5.

Table 4.5: The breaking time and dissolution time of membranes dissolving at different temperatures.

Dissolution Temperature / °C	Breaking Time / h	Dissolution Time / h
90	24	--
110	4.5	24
130	0.5	1.33
160	0.17	0.67

Here, the dissolution time was defined as the time of membranes dissolving into the solution entirely. It is noted that membranes at temperature above 110°C are capable of dissolving into phosphoric acid solution, while membranes at 90°C are unable to dissolve thoroughly during the experimental time. Additionally, the breaking time was defined as the time point of the membrane starting to break into small pieces. As it shown in Table 4.5, less time was required for the membrane to break at higher temperature. Membranes dissolved at 160 °C got extremely swollen and soft only in 2 minutes shown in Figure 4.3 (a) while it took the membrane 4 hours to become a little bit swollen at 90 °C shown in Figure 4.1 (a). In addition, it also took much less time for the membranes from the swollen state to the broken state or from the broken state to the dissolving state at high temperature. This is coincident with the doping behaviors of membranes that less time was required to approach the equilibrium doping level [77]. From the thermodynamic point of view, the process of membrane dissolving in acid can be regarded as an endothermic reaction [102], which means high temperature can accelerate the rate of dissolution. Also, as it was discussed in the last chapter, more phosphoric acid absorption of membranes can cause higher swelling and further cause the decrease of mechanical strength of membranes, which makes the membranes easily break into pieces.

In the case of crosslinked AB-PBI, the membranes could not entirely dissolve into phosphoric acid solution at all temperatures. All the membranes in phosphoric acid solution showed a crimping phenomenon after some period as shown in Figure 4.4. The crimping time of each membrane at

various temperatures was recorded and shown in Figure 4.5. The crimping time was defined as the time consumed by membranes starting from its original state to the curly state.



Figure 4.4: The curly state of the crosslinked AB-PBI membranes at various temperatures.

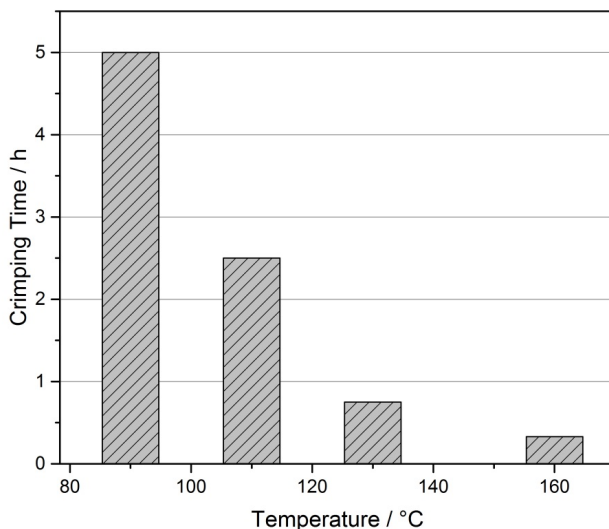


Figure 4.5: The crimping time of crosslinked AB-PBI membranes immersed at various temperatures in an open vessel.

As shown in Figure 4.5, the crimping time of the membrane decreased with increasing temperature. The crimping time of membranes immersed at 90 °C was 15 times longer than it of membranes immersed at 160 °C. The high mobility of phosphoric acid molecules and polymer chains at high temperature explain this result quite well.

Furthermore, in this work, the membranes were doped with phosphoric acid first and subsequently washed by NaOH solution and distilled water and further dried at 150 °C for half hour. All these treatments can cause a reconstruction of the polymer structure. The reconstruction of the polymer structure (forming crystalline structure) was even observed in aged AB-PBI which was stored at room temperature over long periods [103]. Additionally, Aili et al. [104] investigated the effect of heat-treatment on PBI membranes. They found that after heat-treatment, the degree of crystallinity of PBI membranes increased. The mechanical strength and chemical stability of the membranes in Fenton solution increased and solubility of the membranes in DMAc solution decreased after heat-treatment. Additionally, they demonstrated that the membrane of higher crystallinity exhibited higher proton conductivity, it was suggested that the phosphoric acid was forced into the amorphous regions creating highly proton conducting pathways through the membrane cross-section. The degree of crystallinity can be further increased by heat treatment or by stretching the membrane in order to enhance the polymer chain orientation [105]. Thus, in this work, after first washing process, the reconstruction of the polymer structure was recognized to be a process of forming crystalline structure in the membrane. The existence of crystallinity inside membranes increased the mechanical strength and decreased the solubility of membranes. This could explain the inconspicuous weight loss of membranes after first washing process, showing in Figure 4.6 and 4.8.

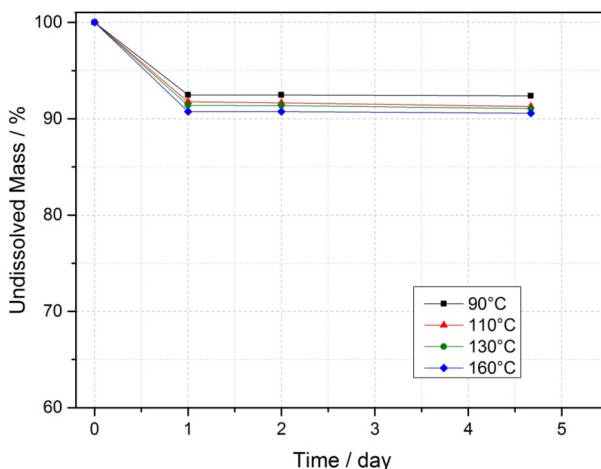


Figure 4.6: The weight loss of crosslinked AB-PBI membrane at various temperatures as a function of time in an open vessel.

As shown in Figure 4.6, the weight loss of crosslinked AB-PBI membranes increased with temperature. This is generally in agreement with what was found in non-crosslinked AB-PBI membranes. However, compared with non-crosslinked AB-PBI which can entirely dissolve into phosphoric acid at most of experimental temperature, maximum of about 10% weight loss of crosslinked AB-PBI was obtained in this experiment, which indicates better stability of crosslinked membranes in phosphoric acid.

4.2.2 Dissolving membranes in closed vessel

In this section, membranes were immersed into various phosphoric acid solutions of various concentrations in a closed vessel at 160 °C to investigate the dissolution behaviors of membranes. The dissolution phenomenon of AB-PBI membranes immersed in 85 wt.-%, 95 wt.-% and 100 wt.-% phosphoric acid solutions were observed as shown in Figure 4.7. The membrane immersed in 100 wt.-% phosphoric acid solution first became extremely swollen and then gradually diffused into the solution (showing in Figure 4.7 (b)), while membranes immersed in 85 wt.-% and 95 wt.-% phosphoric acid solution were able to maintain their integrity after half a month (shown in Figure 4.7 (a)). The membrane immersed in 95 wt.-% phosphoric acid solution was much more swollen and soft than that immersed in 85 wt.-% phosphoric acid solution.

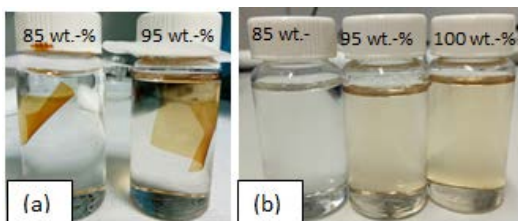


Figure 4.7: (a) The photographs of membranes in 85 wt.-% and 95 wt.-% phosphoric acid solutions for half a month; (b) The photographs of phosphoric acid with various concentrations after membranes being taken out at the fifth day.

Figure 4.7 (b) displays the states of solutions with membranes being taken out after 5 days. It is clear that the acid solution turned more yellow with the concentration, which indicated that more amount of polymer molecules were dissolved into acid solution at higher concentration.

For crosslinked AB-PBI membranes, the dissolution phenomenon was not observable with naked eyes. All crosslinked membranes curled as they were put in the open vessel as shown in Figure 4.4.

The weight loss of AB-PBI and crosslinked AB-PBI membranes in various phosphoric acid solutions at 160 °C was recorded as showing in Figure 4.8. From Figure 4.8 left, it can be seen that the membrane immersed in 100 wt.-% phosphoric acid solution dissolved entirely into the solution within only 40 minutes. The weight loss of membranes immersed in 95 wt.-% and 85 wt.-% phosphoric acid solution after 40 h was approximately 13% and 7% respectively. It was found that the phosphoric acid doping level of AB-PBI increased dramatically when the acid concentration exceeded 85 wt.-% [77]. In high concentration acid solution, the polymer chains would like to be separated more by the high amount of acid absorption which will cause a high dissolution rate of the membranes.

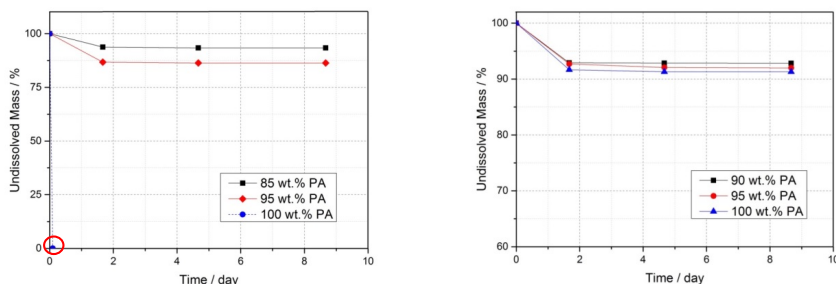


Figure 4.8: The weight loss of AB-PBI membranes (left) and crosslinked AB-PBI membranes (right) in various concentrations of phosphoric acid as a function of time at 160 °C.

The concentration effect on dissolution rate was also found in crosslinked AB-PBI as shown in Figure 4.8 right. However, the difference of weight loss in various concentrations of phosphoric acid was not evident.

In addition, no further weight loss of membranes can be observed after the first washing process at 40 hours. This was suggested to be due to the reconstruction of polymer chains which increased the degree of crystallinity of membranes and further increased mechanical strength and decreased the solubility of membranes in phosphoric acid, as discussed in the last section.

To compare the dissolution behaviors between AB-PBI and crosslinked AB-PBI, the results were shown in Figure 4.9. It can be seen that the weight loss of non-crosslinked AB-PBI membranes is always higher than that of crosslinked AB-PBI at each concentration of acid solution. As discussed in section 3.2.9, the crosslinked membrane had smaller volume swelling than the non-crosslinked membrane. The membrane swelling was strongly restricted by the crosslinking materials. Thus, it can help polymer chains to bond together instead of separating too much and being dissolved by phosphoric acid.

In a HT-PEFC, the normal operating temperature is 160 °C or even higher [6]; the phosphoric acid concentration is approximately up to 100 wt.-%. When non-crosslinked AB-PBI membrane was applied in a HT-PEFC, the risk of membrane failure, as well as membrane dissolution, should be taken into account, as discussed before.

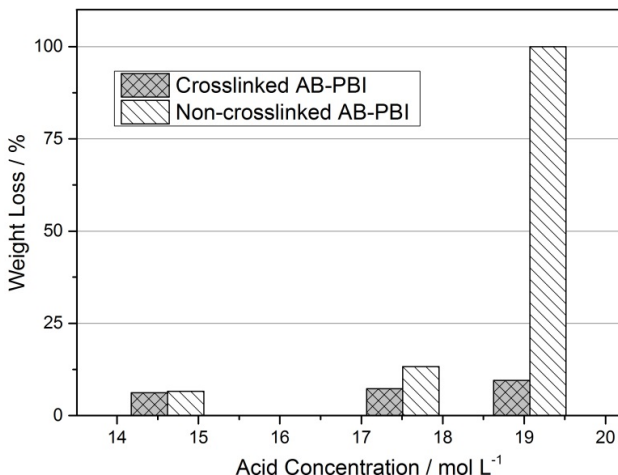


Figure 4.9: The weight loss of non-crosslinked AB-PBI membranes and crosslinked AB-PBI membranes in various concentrations of phosphoric acid solution after 40 h.

4.3 Summary

The present work focuses on the dissolution behavior of AB-PBI and crosslinked AB-PBI membranes at various temperatures and concentrations of phosphoric acid solutions. The results were listed as following:

- Both membranes can partially or entirely dissolve into phosphoric acid solution. The dissolution rate of membranes increases with temperature and phosphoric acid concentration.
- Crosslinked AB-PBI membranes are much more stable, especially in high concentration (approximately 100 wt.-%) of phosphoric acid solution, than non-crosslinked AB-PBI membranes which entirely dissolve into acid solution.
- In HT-PEFC application, solubility of membranes in phosphoric acid should be generally taken into account in order to obtain stable and long-life performance.

5 Long-term single cell test and post-mortem analysis

In this chapter, two HT-PEFCs were tested at same operating conditions for different running period. The cells showed good stability for long-term operation up to 950 hours. Post analysis of the used membranes was done by SEM (scanning electron microscope) and EDX (Energy Dispersive X-Ray Spectroscopy). The experimental results show that the membranes became thinner after long-term test and the polymers of membranes are dissolved into the catalyst layers.

5.1 Experimental setup

5.1.1 MEA assembly

The MEAs used in this work were assembled by two pieces of GDEs (Gas diffusion electrodes) and one piece of phosphoric acid doped membrane in the middle.

The membranes were supplied by FuMA-Tech with a commercial name of “Fuampem[®] AM-55”. The initial thickness of the membranes is about $40 \pm 1 \text{ }\mu\text{m}$. For doping the membranes, they were immersed in phosphoric acid solution with a concentration of 85 wt.-% for 18 h at $110 \text{ }^{\circ}\text{C}$ in open vessels. After doping, the membranes were taken out of the solution and wiped off the aqueous phosphoric acid on their surface. A final total absorption of about $420 \pm 10 \text{ }\%$ (corresponding an acid doping level of $16.6 \pm 0.4 \text{ M}$) of the membranes was obtained. The thickness of the doped membranes was about $86 \pm 2 \text{ }\mu\text{m}$.

The GDEs used for anode and cathode of the MEAs were identical. For the preparation of GDEs, the doctor blade technique was used. The GDL (Freudenberg FCCTKG, H2315, with a thickness of about $250 \text{ }\mu\text{m}$) is composed of carbon paper with microporous layer on one side. The catalyst ink was prepared with platinum catalyst powder (20 wt.-%, HisPEC Johnson Matthey), PTFE dispersion (60 wt.-%, Dyneon), water and organic solvent (propanol: isopropanol = 1: 1, vol. ratio), and dispersed with an ultrasonic horn. After that, the ink was coated onto the microporous layer of GDLs. Then the

GDEs were dried at room temperature in a fume hood overnight and heated in an oven at 60 °C for 30 minutes in order to eliminate the solvent. The final thickness of the GDEs had a range from 360 μm to 390 μm , and the average platinum loading was $1.00 \pm 0.05 \text{ mg cm}^{-2}$. The GDEs were cut into small pieces with the size of $4.2 \times 4.2 \text{ cm}^2$.

5.1.2 Single cell tests and EIS measurements

The membrane and the GDEs prepared before were assembled inside cells without a preceding hot-pressing. A sub-gasket with a hollow area of $3.8 \times 3.8 \text{ cm}^2$ was introduced into the interface of the GDE and membrane during the cell assembly, which refers to an active area of 14.44 cm^2 for the cells. The total compression rate of the whole MEAs was about 15% during the cell assembly. The cells were tested on a standard test-rig built up by IEK-3, Forschungszentrum Jülich. Hydrogen and air were fed into the cells as anodic and cathodic gases with a stoichiometry of $\lambda_{(\text{An/Ca})} = 2/2$. The dew point of hydrogen and air were -50 °C and -58 °C, which were considered as dry gases. The operating temperature was always 160 °C. A break-in procedure [77] was applied for every cell. After the break-in procedure, further measurement of the cells can be conducted. In the current density range of 0 – 200 mA cm^{-2} , the gas flow rates of anode and cathode were the same as at current density of 200 mA cm^{-2} .

For the long-term test, the cells were operated with a constant current density of 200 mA cm^{-2} , excluding some intermittent measurements of polarization curves of the cells.

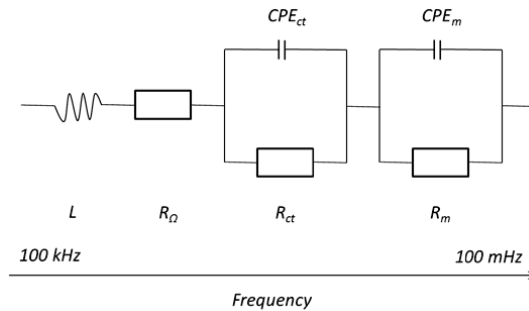


Figure 5.1: Equivalent circuit of HT-PEFC for Nyquist plots fitting.

To quantify resistances of HT-PEFCs, simultaneous electrochemical impedance spectroscopy (EIS) was used to analyze the cells. The EIS was measured by a Zahner Zennium electrochemical workstation (ZAHNER-Elektrik GmbH & Co.KG), with an additional power booster for the high current application at the operating condition of 200 mA cm^{-2} and $\lambda_{\text{An/Ca}}=2/2$. The setup for the impedance spectroscopy measurements consisted of a conventional two-electrode setup, with the anode serving as a quasi-reference and counter electrode and the cathode working as a sense electrode. A frequency range of $10^{-1} - 10^5 \text{ Hz}$ and AC signal voltage amplitude of $\pm 5 \text{ mV}$ was chosen. From the high-frequency intercept of the EIS spectra with the real axis in the Nyquist plot (i.e., no phase shift between current and voltage), the ohmic resistance of cells was given. The obtained Nyquist plots were fitted with an equivalent circuit as shown in Figure 5.1. The meaning of each element shown in Figure 5.1 is presented in Table 5.1.

Table 5.1: The physical meaning of each element shown in Figure 5.1.

Element	Unit	Physical meaning
L	Henry	cable inductance
R_Ω	mohm cm^2	ohmic resistance
R_{ct}	mohm cm^2	charge transfer resistance (kinetic resistance)
CPE_{ct}	Farad cm^{-2}	constant phase element of ORR kinetic
R_m	mohm cm^2	mass transport resistance
CPE_m	Farad cm^{-2}	constant phase element of mass transport

5.1.3 Sample preparation for post-mortem analysis

The cells used for long-term test were disassembled and the MEAs were taken out. A rectangular part of the MEAs was cut off. The long edge of the rectangle was perpendicular to the flow channel of the flow field as shown in Figure 5.2.

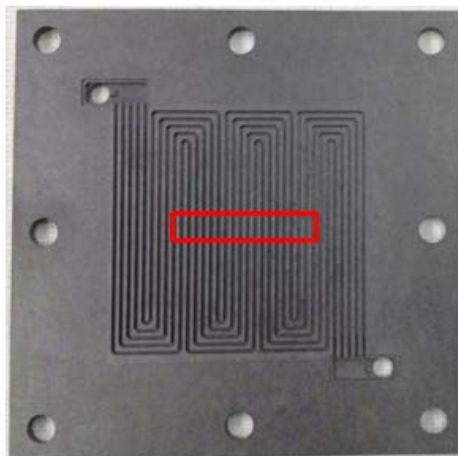


Figure 5.2: The flow field of the bipolar plate used in this work. The red rectangle represents how the samples of MEAs were cut.

The rectangular samples were immersed in distilled water with an ultrasonic horn. This process was repeated 3 times. After that, the GDLs and majority of catalyst layers were separated from the membrane. Then, the membranes were taken out of the water and washed by flowing water for 5 minutes. Later, the membranes were dried in an oven at 150 °C for 30 minutes. Finally, the dried samples were blown by pressurized nitrogen flow. In order to make a comparison of the membrane which was not used for long-term test, another cell was made with the same conditions of the cells used for long-term test but only operated for break-in procedure. The sample preparation of this cell was same as described before. The samples were named as sample #0, sample #1 and sample #2 for the cell only operated for break-in procedure, cell #1 and cell #2 respectively. The outlook of the samples is shown in Figure 5.3. Additionally, an initial membrane was doped with the same amount of phosphoric acid and washed with distilled water to remove the phosphoric acid again. This membrane was used for blank comparison. The thickness of the dried membrane after pre-doping and pre-washing process was $55 \pm 1 \mu\text{m}$.

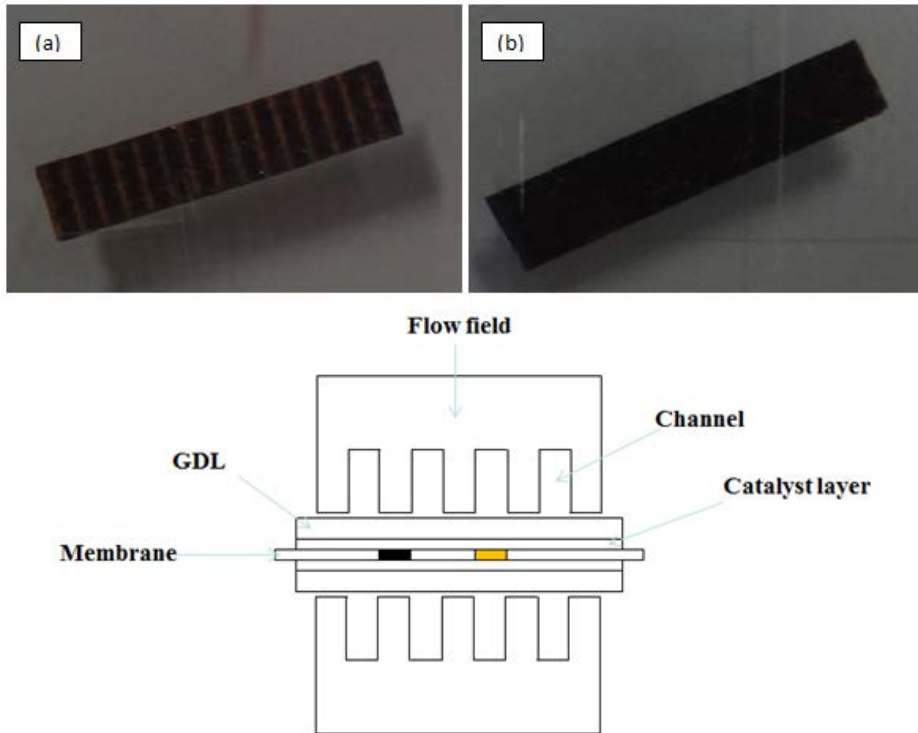


Figure 5.3: (a) and (b) are the photographs of sample #0 and sample #2 respectively. The bottom schematic is the cross-section of MEA with bipolar plates.

Figure 5.3 (a) and (b) show the outlook of sample #0 and sample #2. As illustrated, there were some black and yellow stripes occurring alternately on the surface of the membrane for sample #0. The black stripes were recognised as the adhered catalyst on the membrane surface. However, these alternate changes of color could not be observed on sample #2. Since sample #1 had similar outlook with sample #2, the photograph of sample #1 is not displayed here. The bottom schematic of Figure 5.3 can be used to explain the reason of the alternate changes of color. As mentioned in the section 5.1.2, the MEAs were compressed by 15% during cell assembling. However, the flow field was not a flat plate but with some ribs and channels. The MEAs under the ribs would accept the completely 15% compression, but those under the channel would accept much less compression of 15% due to the soft materials of each component of MEAs. These uneven stresses of MEAs under ribs and channels caused the different penetration rate of catalyst and polymer. However, for sample #2, the yellow

stripes disappeared, indicating much larger penetration between membrane and catalyst even under the channels of the flow field after long-term test.

5.2 Results and discussions

5.2.1 Single cell test results

In this work, two cells were used for the long-term test. One cell (marked as cell #1) was run for 600 hours and the other (marked as cell #2) was run for 950 hours. The results of single cell test of these two cells are shown in Figure 5.4.

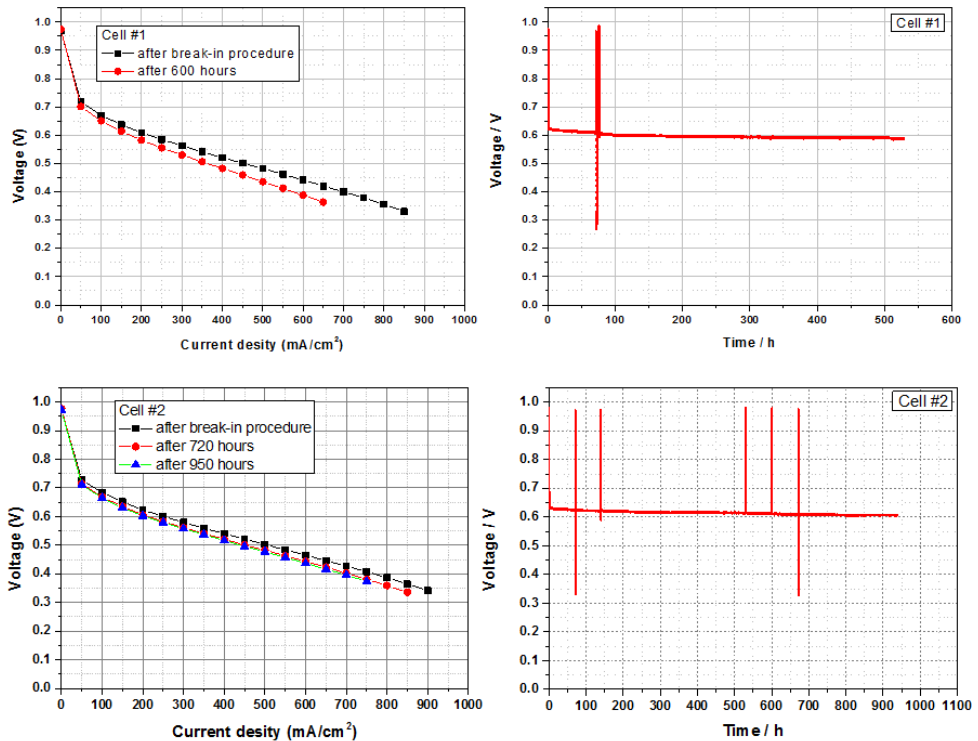


Figure 5.4: The results of single cell test. (Upper left) the polarization curves of cell #1 before and after long-term test; (Upper right) the durability test of cell #1 at 200 mA cm^{-2} ; (Bottom left) the polarization curves of cell #2 before and after long-term test; (Bottom right) the durability test of cell #2 at 200 mA cm^{-2} . Testing condition: $\lambda_{\text{An/Ca}}=2/2$, $T = 160^\circ\text{C}$.

As can be seen from Figure 5.4, the cell voltage at 200 mA cm^{-2} of cell #1 was slightly lower than it of cell #2 immediately after the break-in procedure. It was due to the minor variations of acid doping level of membranes, the Pt loading of catalyst layers and even the cell assembling process.

From the polarization curves, it can be seen that both cells degraded after long-term test. From cell #2, the degradation rate was higher, as the operating time increased. In the results of durability test, the first 70 h for both cells represented the break-in procedure. The cell voltage of cell #1 at 200 mA cm^{-2} was 0.61 V after the break-in procedure and 0.59 V after 600 hours running. The average degradation rate was $37.7 \mu\text{V h}^{-1}$. For cell #2, some fast stop/restart operations of the cell were done at 130 h, 520 h and 600 h in order to record all the data. The stop/restart operations seemed to have no evident effect on the cell performance from the voltage drop in Figure 5.4 bottom right. The cell voltage of cell #2 at 200 mA cm^{-2} was 0.62 V after the break-in procedure and 0.60 V after 950 hours. The average degradation rate was $22.7 \mu\text{V h}^{-1}$, which was slightly lower than it was for cell #1, indicating better performance of cell #2.

5.2.2 EIS results

The electrochemical impedance spectroscopies (EIS) of both cells were taken immediately after the first polarization curve measurement and after finishing the long-term test. The results are shown in Figure 5.5.

From the results shown in Figure 5.5, the ohmic resistance and total resistance of cell #1 were slightly higher than them of cell #2. This was in good agreement with the slightly lower performance of cell #1 shown in Figure 5.4. Additionally, the ohmic resistance of both cells decreased a little bit after long-term test, while both cells had an increase of the total resistance. To quantify the resistances of the two cells, the EIS results were fitted with the equivalent circuit shown in Figure 5.1. The fitting results of each element are shown in Table 5.2.

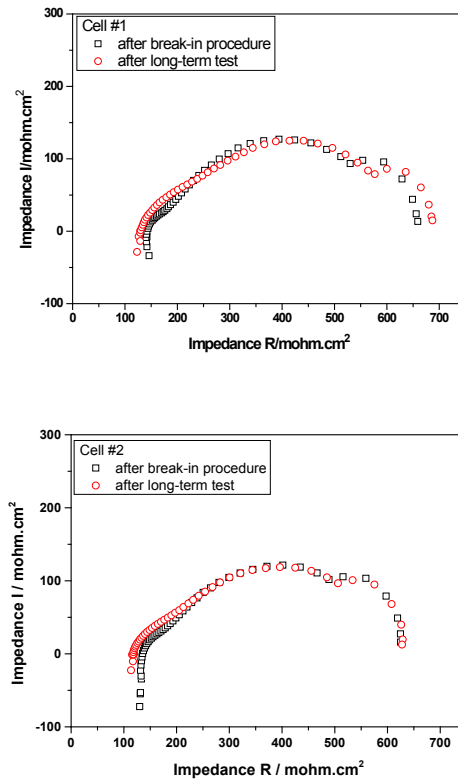


Figure 5.5: The EIS results of cell #1 and #2 after break-in procedure and long-term test at 200 mA cm⁻², $\lambda_{\text{Air}/\text{Ca}}=2/2$, T = 160 °C. The frequency range was from 100 kHz to 100 mHz and AC signal voltage amplitude was ± 5 mV.

Table 5.2: The fitting result of each resistor of the cells at 200 mA cm^{-2} with the equivalent circuit shown in Figure 5.1.

Cells	status	$R_\Omega/\text{mohm cm}^2$	$R_{ct}/\text{mohm cm}^2$	$R_m/\text{mohm cm}^2$	Fitting error
#1	Before	127.751	98.900	456.593	2.67%
#1	After	122.841	108.748	470.022	2.58%
#2	Before	123.332	74.453	461.214	2.55%
#2	After	113.253	96.993	448.795	2.46%

*note: The “Before” means the status of the cell was before long-term test, as well as immediately after break-in procedure; the “After” means the status of the cell was after the long-term test.

From Table 5.2, it can be seen that the ohmic resistances (R_Ω) of both cells decreased after long-term test, while the charge transfer resistances (R_{ct}) and the mass transport resistances (R_m) of both cells increased generally. It was noticed that the mass transport resistance of cell #2 after long-term test was lower than before long-term test. This was due to the fitting error. The decrease of R_Ω and increase of R_{ct} and R_m were suggested to be caused by membrane thinning as well as the dissolution of the membrane.

Moreover, the ohmic resistance R_Ω of cell #1 decreased by 3.84 % after the long-term test (600 hours), while it decreased by 8.17 % for cell #2 after the long-term test (950 hours). In the case of charge transfer resistance R_{ct} , after long-term tests, it increased by 10.00 % and 30.27 % for cell #1 and cell #2 respectively. This demonstrates that longer operation time of HT-PEFC can cause higher dissolution of the membrane and make the membrane thinner. More discussion about this phenomenon will be given in the post-mortem analysis results in the next section.

5.2.3 Post-mortem analysis -- SEM results

Figure 5.6 shows the SEM images of the cross-sections of sample #0, sample #1 and sample #2. Figure 5.6 (a), (c) and (e) represent the membranes under the channels of flow field for sample #0, sample #1 and sample #2 respectively. And Figure 5.6 (b), (d) and (f) are the membranes under the ribs of flow field for sample #0, sample #1 and sample #2 respectively.

It can be seen from Figure 5.6 that, for every sample, the part of the membranes under channels of flow field were thicker than those under the ribs. It was generally due to the uneven stress on the membranes. There was higher pressure on the membranes under ribs, which resulted in a higher penetration rate between membrane and catalyst layer.

Comparing sample #0, sample #1 and sample #2, it was found that the thicknesses of the membranes both under channels and ribs of flow field decreased with the increase of operating time of the cells. This membrane thinning effect was also found in the literature. Kerr et al. [106] tested a cell for 17000 h at 240 mA cm^{-2} and found that the membrane showed thinning from an undoped $40 \text{ }\mu\text{m}$ to $18 \text{ }\mu\text{m}$ in some areas of the membrane after testing. Liu et al. [107] did a 600 h lifetime test of a HT-PEFC and found that the thickness of the doped PBI membrane after the life test decreased from $38.5 \text{ }\mu\text{m}$ to $30.3 \text{ }\mu\text{m}$. Oono et al. [99] compared the degradation of the cells with PBI membrane and crosslinked ABPBI membrane. They found that the thickness of the PBI membranes after long-term test was roughly 1/4 of it before long-term test, while nearly no obvious thickness change can be found for crosslinked ABPBI membranes. Previously, it was suggested that the mechanism of the membrane thinning after long-term test was due to chemical degradation. It means the $\text{HO}\cdot$ and $\text{HOO}\cdot$ free radicals which were suggested to be produced by the incomplete reduction of oxygen on the cathode side of fuel cells can attack the polymer chains of PBI and cause the polymer backbone to break at the benzene rings [95]. However, there was no further evidence to prove the existence of the $\text{HO}\cdot$ and $\text{HOO}\cdot$ free radicals in an operating HT-PEFC. In this work, the membrane thinning was suggested to be due to the physical degradation mechanism, as well as the dissolution of membranes in phosphoric acid. As discussed in Chapter 4, PBI type membranes can partially or entirely dissolve into phosphoric acid solution depending on the phosphoric acid concentration, temperature, as well as time. In a HT-PEFC, the membranes were first dissolved into phosphoric acid. Then the mobility of the polymer chains was highly increased by the polymer

change from solid status to liquid status. After that, the polymer molecules would like to move with the movement of phosphoric acid molecules and finally diffuse into catalyst layers [99].

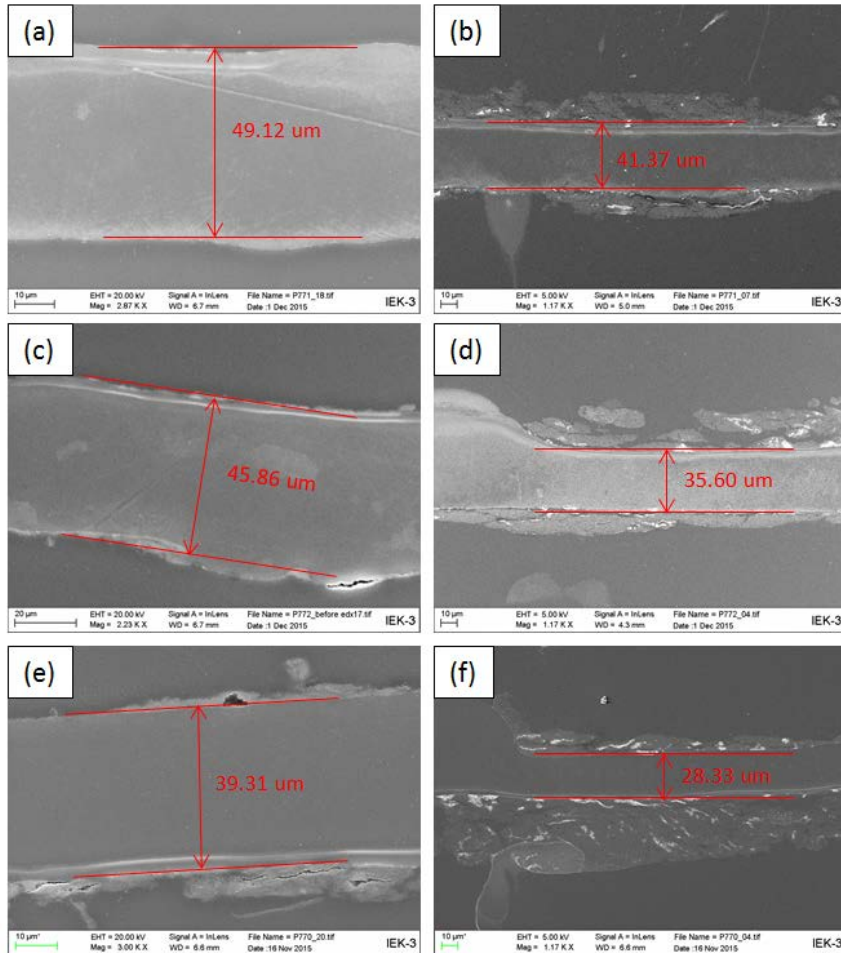


Figure 5.6: The SEM images of cross-section of used membranes. (a) and (b) were the membrane under the channel of flow field and it under the rib of flow field for sample #0, as well as after 70 h operation; (c) and (d) were the membrane under the channel and the rib for sample #1, as well as after 600 h operation; (e) and (f) were the membrane under the channel and the rib for sample #2, as well as after 950 h operation.

However, one can notice that the thicknesses of sample #0 and sample #1 under channel were higher than that of the undoped membrane which is $40 \pm 1 \mu\text{m}$. But the thicknesses of all the samples

were lower than that of the dried membrane after pre-doping and pre-washing which was $55 \pm 1 \mu\text{m}$. The comparison of thickness of different membranes is shown in Figure 5.7. Comparing the membrane after pre-doping and pre-washing process and the membranes used for single cell test, even the membrane used only for break-in procedure was thinner, indicating a certain amount of membrane dissolution. Comparing the EIS results, the membrane thinning effect well explained the decrease of ohmic resistance after long-term test. And the thinner membrane resulted in a higher decrease of ohmic resistance for longer operation time.

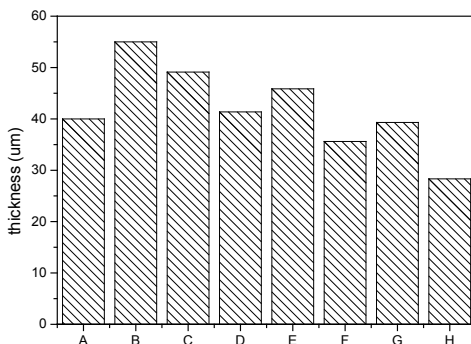


Figure 5.7: The thicknesses of different membranes. A): the initial membrane; B): the dried membrane after pre-doped and pre-washed process; C): the membrane under channel for sample #0; D): the membrane under rib for sample #0; E): the membrane under channel for sample #1; F): the membrane under rib for sample #1; G): the membrane under channel for sample #2; H): the membrane under rib for sample #2.

Furthermore, the amount of catalyst adhering on the surface of membranes increased with the operation time as shown in Figure 5.6. The reason for the catalyst adhering on the surface of membranes was suggested to the immigration of the dissolved membranes into catalyst layer. Then the polymers of the membranes inside catalyst layer acted as a strong binder for catalyst particles, which made the catalyst hard to be removed from the surface of the membranes even under the condition of ultrasonic dispersion. On the other hand, it was suggested that the dissolved polymer of the membrane in catalyst layer could reduce the active area of catalyst, resulting in a decrease of the kinetics of the oxygen reduction reaction (ORR) and hydrogen oxidation reaction (HOR) [99]. Thus, the more membranes dissolved into catalyst layer, the more active areas of the catalyst would be covered. This can accurately explain the increase of charge transfer resistance after long-term

test. And the increase of charge transfer resistance can be related to more dissolution of membrane materials after longer operation time.

In Figure 5.6 (d) and (f), it can be noticed that there was a convex shape of the membrane shown on the right side of the images. These convex shapes of the membranes can be found in the whole length of the membranes in every sample under polarizing microscope as shown in Figure 5.8 (a). These convex shaped membranes were due to the unevenness of the catalyst layer on GDEs. After finishing the preparation of the GDEs, there were a lot of cracks in the catalyst layer as shown in Figure 5.8 (b). During the cell assembly, the MEAs were compressed. The soft membranes were forced to move into the cracks, which resulted in the convex shaped part of the membranes.

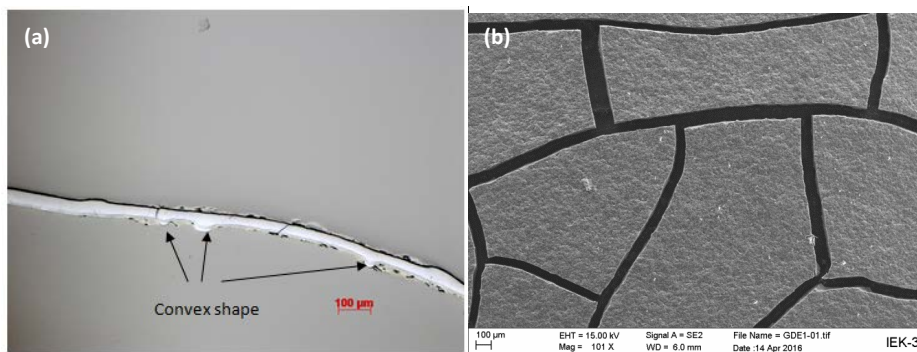


Figure 5.8: (a) The cross section image of sample #0 under polarizing microscopy; (b) The SEM image of the surface of catalyst layer.

In addition, it can be further seen in Figure 5.6 that there were some bright bands inside the membranes for each sample, such as the upper side of the membranes in Figure 5.6 (a) to (d) and the bottom side of the membranes in Figure 5.6 (e) and (f). This phenomenon can be further observed with FIB-SEM as shown in Figure 5.9.

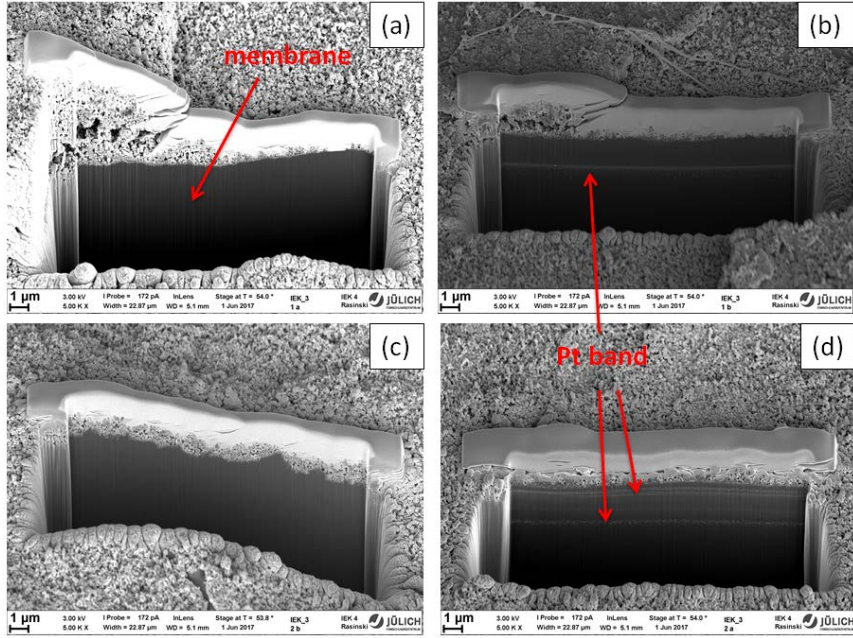


Figure 5.9: Cross-sectional FIB-SEM images. (a) and (b) were the two sides of the membrane used for break-in procedure; (c) and (d) were the two sides of the membrane used for 300 h at various current density.

The samples used in the FIB-SEM were prepared by Shuai Liu (IEK-3); the images were taken by Dr. Rasinski (IEK-4). The bright bands were recognized as the diffused platinum, which was widely found and discussed in Nafion based membranes used in classical PEFC. Yu et al. [108] did the cycling test of classical PEFC with PtCo/C and Pt/C cathode catalyst and found the bright and dense Pt band at the interface of cathode and membrane for both catalyst. Ferreira et al. [109] also found the Pt band near the cathode/membrane interface after 2000 h OCV operation for classical PEFC. This Pt band at the interface of cathode and membrane was also found by Mailiard et al. [110]. Yasuda et al. [111] studied the platinum dissolution and deposition in classical PFEC by potential cycling with a gas supply of H_2 and N_2 for anode and cathode side respectively. They could not observe the Pt band in the region of the membrane and even in the region quite near the cathode interface. Another work by Bi et al. [112] also proved that there was no Pt moving into the membrane with the gas supply of H_2 and N_2 for anode and cathode side respectively. However, when they changed the cathodic gas to air, a clear Pt band was found at the interface of cathode and membrane. Furthermore, Kocha [113] (page 172) demonstrated that the location of the Pt band was a function of the partial pressures of

hydrogen and oxygen on the anode and cathode. The band was formed closer to the anode when the partial pressure of hydrogen is lower. In contrast it formed in the vicinity of the cathode if air is used on the cathode side instead of pure oxygen. In this work, the anodic and cathodic gases were pure H_2 and air respectively. Thus it can be deduced that the location of platinum bands in HT-PEFC represented the cathode side of the membranes. As shown in Figure 5.9 (a) and (c), there was no platinum band inside the membranes, indicating that these were the anode side of the membranes. In contrast, Figure 5.9 (b) and (d) represented the cathode side of the membranes.

Therefore, based on the position of the platinum band in Figure 5.6, the anode and cathode side of the membranes can be determined. Furthermore, it can be found that more catalyst adhered on the cathode side than on the anode side of the membranes, which was especially obvious in Figure 5.6 (f). The reason of higher amount of catalyst adherence on the cathode side of the membranes is not clear yet. But it is known that the morphology of the cathode catalyst layer changes due to carbon corrosion and Pt agglomeration and dissolution [114, 115]. This is related to the high cathode potential. The result in the present work and in literature demonstrates that the anode catalyst layer is more stable than cathode catalyst layer.

5.2.4 Post-mortem analysis -- EDX results

Energy dispersive X-Ray spectroscopy (EDX) was used to detect the elements of carbon (C), fluorine (F) and platinum (Pt). The X-Ray scanning spectrums of each sample are shown in Figure 5.10. The scanning spectrum 2 in Figure 5.10 (a), the scanning spectrum 6 in Figure 5.10 (b) and the scanning spectrum 5 in Figure 5.10 (c) were used to analysis the atom ratio of C/Pt in catalyst layers. The scanning results are shown in Table 5.3.

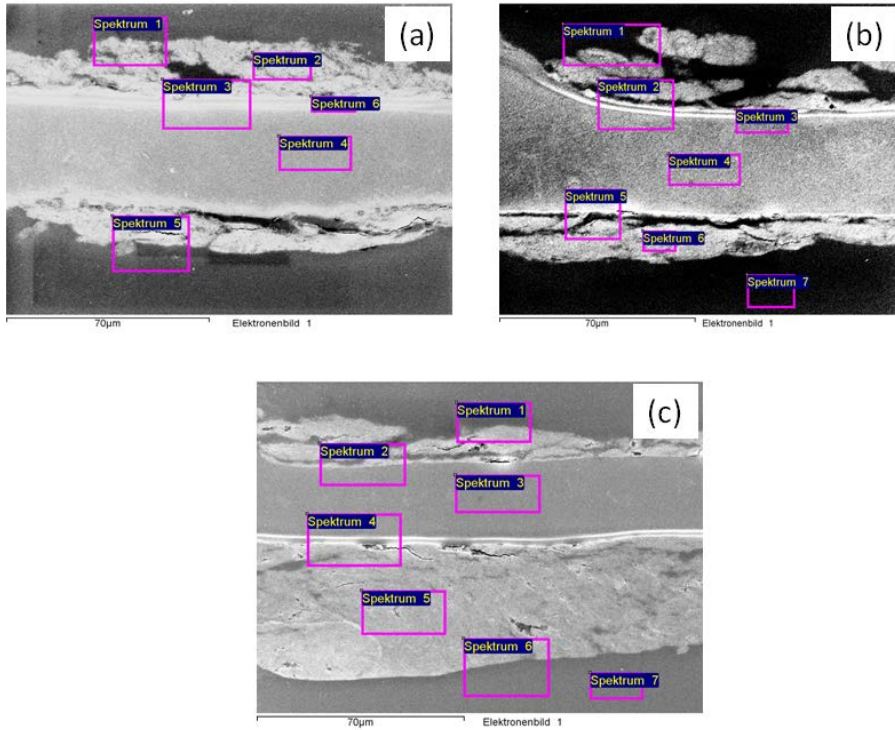


Figure 5.10: The SEM images of the cross-section of the membranes of sample #0 (a), sample #1 (b) and sample #2 (c) used for the EDX analysis.

Table 5.3: The atom fractions of C, F, and Pt in the adhered catalyst layers.

Samples	C / %	F / %	Pt / %
#0	92.24	6.90	0.54
#1	72.85	10.14	0.47
#2	89.37	13.97	0.56

As it was mentioned in the GDEs preparation, there was some amount of PTFE inside the catalyst layer. To eliminate the carbon atom introduced by the PTFE, the atom ratios of C/Pt in the adhered catalyst layers can be calculated as following:

$$C/Pt = \frac{C/\% - \frac{1}{2}F/\%}{Pt/\%} \quad (5.1)$$

where the C/%, F/% and Pt% are the atom fractions of C, F, and Pt in the adhered catalyst layers respectively. The fraction of $\frac{1}{2}$ comes from the atom fractions of C and F in the PTFE molecules.

In addition, in order to compare with the initial catalyst layer, the atom ratio of C/Pt can be calculated based on the composition of the catalyst power (20 wt.-% of platinum in carbon black) as follows:

$$C/Pt = \frac{80\%/M_C}{20\%/M_{Pt}} \quad (5.2)$$

where M_C and M_{Pt} are the molar weight of the C atom and Pt atom respectively, as well as 12.01 g mol^{-1} and $195.05 \text{ g mol}^{-1}$.

The results of the atom ratios of C/Pt are listed in the Table 5.4. As can be seen, the atom ratios of C/Pt in the adhered catalyst layers were nearly in the same range. This indicates the saturated absorption of dissolved membranes in the pores of the catalyst layers. The slight difference of the atom ratios of C/Pt of various samples was due to the slight variations of porosity during the preparation of the catalyst layers. Comparing with the initial catalyst layer, the atom ratios of C/Pt in the adhered catalyst layers were 2.2-2.5 times of that in the initial catalyst layer. The high excess content of carbon in the adhered catalyst layer was suggested to be mainly caused by the dissolved membranes, of which the polymer molecules are mainly carbon based structures as shown in Figure 2.1 and Table 2.1.

Table 5.4: The atom ratios of C/Pt in the adhered catalyst layers for different samples, as well in the initial catalyst layer.

Samples	#0	#1	#2	Initial catalyst
C/Pt	164.4:1	144.2:1	147.1:1	65.0:1

In other words, more carbon atoms found in the adhered catalyst layers than in the initial catalyst layer indicated that lots of polymers of the membrane was dissolved into the catalyst layers and bound with the catalyst particles.

5.3 Summary

In this chapter, several single cells were tested for different operating time. Post analysis of the used membranes was made. The main results were listed as following:

- The ohmic resistance of the cells decreased while the charge transfer resistance and mass transport resistance generally increased after long-term test.
- The decrease of ohmic resistance was recognized to be due to the membrane thinning effect causing by the dissolution of the membranes into phosphoric acid; the increase of the charge transfer resistance was due to the immigration of the dissolved membranes into catalyst, which reduced the active area of the catalyst layer.
- After long-term test, the catalyst layers partly adhered to the both side of the membranes and formed a semi-CCM structure due to the strong binding effect of the dissolved polymers of the PBI typed membrane inside the catalyst layers.
- Furthermore, more amount of catalyst adhered to the cathode side of the membranes comparing with the anode side.
- Additionally, with the increase of operating time, the membranes were getting thinner and more catalyst adhered on the membranes, indicating more membrane material can be found in the catalyst layer.

6 Local current density analysis of the operando cell

Local current density can be affected by various factors, such as oxygen concentration along the channel, local water vapor partial pressure which results in different phosphoric acid concentration and further proton conductivity inside the membrane, local temperature, local catalyst loading and thickness of the membrane as well. In order to characterize the cell used for neutron operando visualization (Chapter 7), the temperature as well as the current density distribution was determined. In this chapter, the flow-field chosen consists of five parallel channels to assume well defined flow properties.

6.1 Experimental setup

6.1.1 Cell design

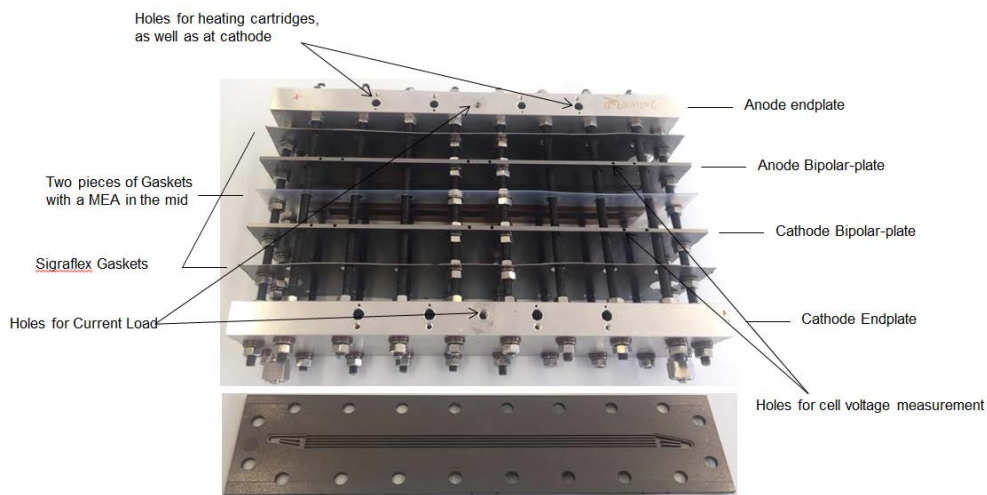


Figure 6.1: Long cell design with five straight parallel gas channels.

As is shown in Figure 6.1, a long cell with five straight parallel gas channels for the flow field and active area is 21.5 cm^2 (width \times length = $1 \text{ cm} \times 21.5 \text{ cm}$) [116] was used for the presented measurements. By using this cell, gas crossover under the bars between neighboring channels can be avoided, inducing well-defined gas transport properties in the cell. The sensor plate of current scan shut (as shown in Figure 2.5) is inserted between bipolar plate and Sigraflex gasket at anode side as shown in Figure 2.6. Hydrogen and air were fed into the cells as anodic and cathodic gases. The operating temperature was always 160°C . A break-in procedure [77] was applied for every cell before current density distribution measurement.

6.1.2 MEA preparation

In this work, the MEA preparation was generally similar to the preparation mentioned in Chapter 5 but with different dimension values for membrane and GDEs size. In the case of GDEs preparation, there was a thickness gradient of $390 \mu\text{m}$ to $360 \mu\text{m}$ of the GDEs from coating start and end due to the doctor blade technique. This indicates a thickness gradient of catalyst layer of about $140 \mu\text{m}$ to $110 \mu\text{m}$. The GDEs were finally cut into piece with the size of $1 \text{ cm} \times 21.5 \text{ cm}$. The cutting lines of the length of the GDEs were parallel with the coating orientation. Due to the relatively high length of the GDEs, the thickness gradient of the catalyst layer from one side to another side cannot be neglected. During the cell assembly, in order to avoid the inhomogeneous compression of the membrane, the MEA was assembled as shown in Figure 6.2. In the cathode side, the thickness of the catalyst layer decreases from left to right, while it increases from left to right in the anode.

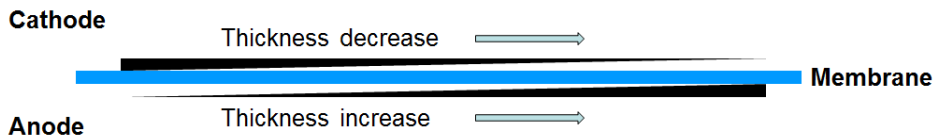


Figure 6.2: Scheme of the MEA assembling.

As shown in Figure 2.5 (in Chapter 2), there are 70 segments on the sensor plate of the current scan shut. Each segment can measure the corresponding local current when the sensor plate is assembled in a cell shown in Figure 2.6 (in Chapter 2). In order to obtain comparable local current corresponding to the local condition of the MEA, the segments on the sensor plate were marked as 0-69 from the left side to the right side of the cell.

6.2 Results and discussion

Temperature affects the kinetics of the oxygen reduction reaction and the phosphoric acid concentration. The inhomogeneous temperature distribution can result in an inhomogeneous current distribution. Additionally, there are 4 holes for the heating cartridges on both sides of the endplates as shown in Figure 6.1. Thus, two heating methods were applied here to investigate the effect of temperature on the local current density distribution. For heating method #1, two heating cartridges were inserted in the two holes in the mid for both sides of the endplates. And in the case of heating method #2, two heating cartridges were inserted in the two holes at the edge of the both side endplates. The results of temperature distribution are shown in Figure 6.3.

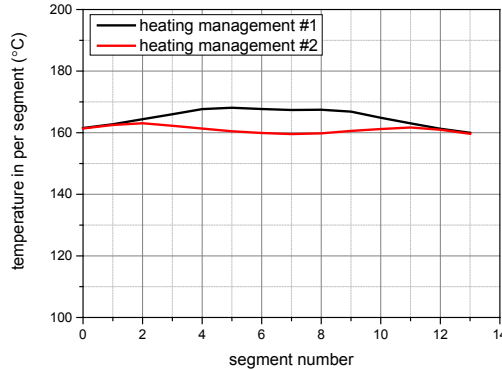


Figure 6.3: Temperature distribution along the channel for different heating managements.

As shown in Figure 6.3, at the middle part of the cell, higher temperature is observed for heating method #1 than heating method #2. The corresponding current density distributions were also measured with co-flow gases ($\lambda_{\text{An/Ca}}=2/2$) which were fed in at left side of the cell and shown in Figure 6.4. It is clear that local current density along the gases orientation at each average current density of the cell decreases first and then increases slightly. The higher local current density at gases inlet than at gases outlet can be observed. Considering the different heating methods, a slightly higher local current density at the middle of the cell with heating method #1 can be observed, which corresponds the higher temperature at the middle of the cell. Moreover, it can be

noted that, with the increase of average current density, the temperature effect is magnified. At an average current density of 200 mA cm^{-2} , there was no pronounced temperature effect.

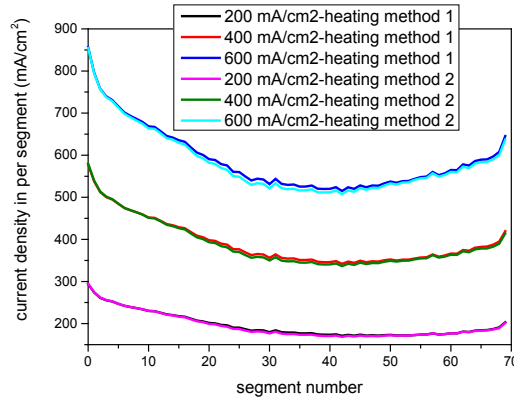


Figure 6.4: Local current density distribution along the channel of the cell at various average current densities with two different heating methods. $\lambda_{\text{An/Ca}}=2/2$, co-flow, gas orientation from left to right.

In addition, a strong increase of the current at the left and right side of the cell can be observed. This is due to the fact that the real active cell area exceeds the size of the sensor plate[117]. Despite the strong increase of the current at the edges of the active area of the cell, the local current density decreased first and then increased along the gas flow orientation in all cases of average current densities. However, according to Kvesić et al. [117] and Kulikovskiy et al. [118], the local current density decreases along the gas flow orientation without an increase at gas outlet region. Another simulation work of current density distribution by Chippar and Ju [119] demonstrated that the local current density had an increasing trend along the flow direction due to the substantial temperature increases which enhanced the ORR kinetics and proton conductivity of membrane. This work proved the significant influence of the local ohmic resistance (proton conductivity) on the local current density distribution affected by temperature effect. However, the proton conductivity of phosphoric acid is not only affected by temperature but also the water vapor partial pressure as demonstrated in [43].

In the present work, the temperature has no contribution for the current density distribution as mentioned above. Thus, in order to explain the unexpected current density distribution, the

superposition of two effects, a) oxygen depletion and b) water vapor partial pressure (proton conductivity) along the flow direction, should be taken into account. In the following section, an asymmetric solution of the current density distribution affected by the two effects independently is be given by simulation.

6.3 Model

6.3.1 Oxygen concentration effect

In this case, it is assumed that the local current density is only dependent on oxygen consumption. Some basic assumptions for this case are given in advance as following:

- Constant gas density / ideal mixed gases
- Activation overpotential constant
- No anodic losses
- No ohmic losses
- Isothermal along the channel

Based on Kulikovsky's model [118], the oxygen concentration is the function of the coordinate along the gas flow direction when the gas flow rate of cathode gas is constant as shown in Equation (6.1):

$$c_x = c^0 \left(1 - \frac{1}{\lambda}\right)^{x/L} \quad (6.1)$$

where c_x is the oxygen concentration along the channel, c^0 is the oxygen concentration at gas inlet (in air, it is approximately 21% in volume fraction), λ is the stoichiometry of cathode gas, x is the coordinate along the gas flow direction, L is the length of the channel. Thus, when the stoichiometry of cathode gas is 2, the oxygen concentration along the channel can be illustrated in Figure 6.5.

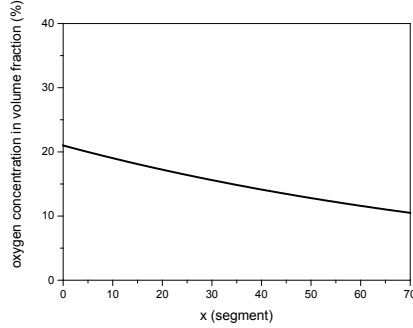


Figure 6.5: Oxygen concentration along the channel, calculated via Eq. (6.1). $\lambda_{\text{air}}=2$.

The local current density along the gas flow direction is related to the consumption of oxygen, which can be expressed as following:

$$j_x = \bar{j} \left(-\lambda \ln \left(1 - \frac{1}{\lambda} \right) \right) \left(1 - \frac{1}{\lambda} \right)^{x/L} \quad (6.2)$$

where j_x is the local current density, \bar{j} is the average current density. The local current density plot is shown in Figure 6.6. As illustrated in Figure 6.5 and 6.6, the local current density decreases with the decrease of oxygen concentration. Comparing with the simulated and experimental results in Figure 6.6, the local current density in real case is lower at gas inlet but higher at gas outlet. This is due to the water vapor partial pressure gradient along the channel, which affects the proton conductivity as well as the ohmic resistance of the membrane.

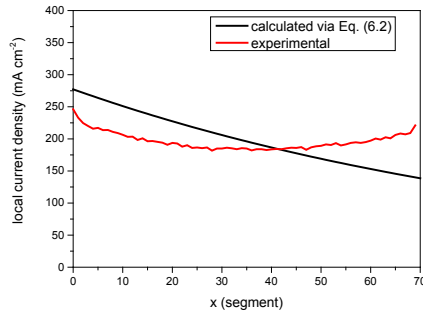


Figure 6.6: Local current density along the channel. Black line is the results calculated via Eq. (6.2), red line is the experimental results (heating method #2). Average current density is 200 mA cm^{-2} , $\lambda_{\text{air}}=2$.

6.3.2 Water vapor partial pressure effect

In this case, it is assumed that the local current density is only dependent on water vapor partial pressure (as well as proton conductivity or ohmic resistance). Some basic assumptions for this case are given in advance as following:

- Constant gas density / ideal mixed gases
- Activation overpotential constant
- No anodic losses
- No cathodic losses
- Isothermal along the channel

Based on the reaction (1.2), the water generation rate is related to the oxygen consumption rate. The relation can be expressed as following:

$$\frac{dc'_x}{dx} = -2 \frac{dc_x}{dx} \quad (6.3)$$

where c'_x is the water vapor concentration in volume fraction along the channel. It is assumed that the generated water will not transport to the anode side through the membrane but stay on the cathode side. Thus, combining with equation (6.1), the water vapor concentration along the channel at the cathode side can be demonstrated as following:

$$c'_x = -2c^0(1 - \frac{1}{\lambda})^{x/L} + b \quad (6.4)$$

It is assumed that at gas inlet, the water vapor concentration is zero, due to the dry gas feed-in. Thus, the equation 6.4 can be rewritten as following:

$$c'_x = -2c^0(1 - \frac{1}{\lambda})^{x/L} + 2c^0 \quad (6.5)$$

Assuming that there is no volume change in the gas channel, thus the water vapor partial pressure under ambient pressure can be calculated as following:

$$P_{H_2O} = P(-2c^0(1 - \frac{1}{\lambda})^{x/L} + 2c^0) \quad (6.6)$$

where P_{H_2O} is the water vapor partial pressure along the channel, P is the ambient pressure (here is 1000 mbar). The result is shown in Figure 6.7.

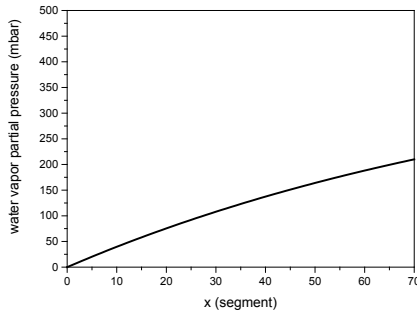


Figure 6.7: Water vapor partial pressure along the channel, calculated via Eq. (6.6). Average current density is 200 mA cm^{-2} , $\lambda_{\text{air}}=2$.

As shown in Figure 6.7, the water vapor partial pressure along the gas flow direction has a range from 0-210 mbar. This can result in a composition range of phosphoric acid in the membrane at temperature of 160 °C from about 76 wt.-% of P_2O_5 to 68 wt.-% of P_2O_5 (seeing Figure 12.2 in [43]). Further within this composition range, the proton conductivity of phosphoric acid at 160 °C decreases with the concentration increasing (seeing Figure 12.7 in [43]).

Assuming that the ohmic resistance of the doped membrane is a linear function of the water vapor partial pressure, thus:

$$R_{mem} = AP_{H_2O} + B \quad (6.7)$$

where R_{mem} is the ohmic resistance of the membrane along the gas flow orientation, A and B are the coefficients of the linear equation.

According to the literature [87], the ohmic resistance of the membrane at dry condition (near 0 mbar of P_{H_2O} at gas inlet) is estimated to be 0.20 Ohm cm², and at wet condition (near 200 mbar of P_{H_2O} at gas outlet) is estimated to be 0.12 Ohm cm². Thus, the coefficients of A and B can be calculated and the equation (6.7) can be rewritten as:

$$R_{mem} = -4 \times 10^{-4} P_{H_2O} + 0.2 \quad (6.8)$$

Assuming the local current distribution along the channel is only controlled by the ohmic resistance of the membrane, therefore based on Ohm's Law, the local current density can be expressed as following:

$$j_x = \frac{k}{R_{mem}} \quad (6.9)$$

where k is a coefficient related to the average current density.

When the average current density is 200 mA cm⁻², k can be calculated by the equation shown below:

$$\bar{j} = \frac{k}{71} \sum_{x=0}^{70} j_x \quad (6.10)$$

Based on equations (6.6), (6.8), (6.9) and (6.10), the local current density distribution along the gas orientation affected by water vapor partial pressure can be expressed by the following equation, and the plot of the local current density distribution is presented in Figure 6.8.

$$j_x = \frac{29.88}{-4 \times 10^{-4} \left(P \left(-2c^0 \left(1 - \frac{1}{\lambda} \right)^{\frac{x}{L}} + 2c^0 \right) \right) + 0.2} \quad (6.11)$$

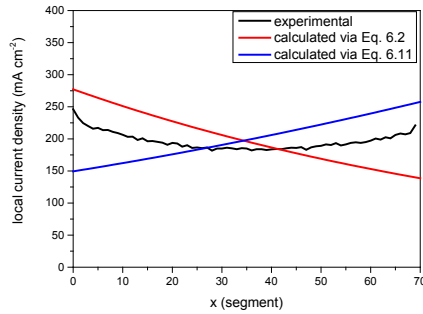


Figure 6.8: Local current density along the channel. Average current density is 200 mA cm^{-2} , $\lambda_{\text{air}}=2$.

As illustrated in Figure 6.7 and 6.8, the local current density increases with the increase of water vapor partial pressure. Comparing with the simulated (via Eq. 6.11) and experimental results in Figure 6.8, the local current density in real case is higher at gas inlet but lower at gas outlet.

Combining with the oxygen concentration effect, at gas inlet, the local condition of the MEA is with the highest oxygen concentration but the lowest water vapor partial pressure. The highest oxygen concentration provides the largest amount of oxygen consumption. However, the lowest water vapor partial pressure can lead to a dehydration of phosphoric acid which restricts the proton transport and contributes a limitation for local current density. Finally, at gas inlet, the oxygen concentration effect dominates and makes the local current density is higher than the average current density.

Similarly, at gas outlet, the local condition of the MEA is with the lowest oxygen concentration but the highest water vapor partial pressure. The highest water vapor partial pressure can cause a hydration of phosphoric acid which is beneficial to proton transport. The faster proton transport pathway can promote more oxygen consumption at gas outlet. Finally, it causes an increase of local current density at gas outlet compared to the local current density at middle part of the channel.

In other words, the co-effect of oxygen concentration and water vapor partial pressure finally makes the local current density along the gas flow orientation decrease first and then increase.

6.4 Summary

In this chapter, the local factors of oxygen concentration and water vapor partial pressure of the cell and their effects on local current density distribution were discussed. The main results are listed as follows:

- In the measurement range, the temperature fluctuation has very slight influence on the current density distribution.
- Despite the effect by cell design and operating conditions, the current density distribution can also be effected by oxygen concentration and water vapor partial pressure. At gas inlet, the local condition of the MEA is with the highest oxygen concentration and lowest water vapor partial pressure, which is opposite at gas outlet. This makes the local current density along the gas flow orientation decrease first and then increase.

7 Operando Neutron radiography of HT-PEFC

In this chapter, a HT-PEFC based on a phosphoric acid-doped PBI membrane with five straight long gas channels on the flow field was investigated under different operating conditions by neutron radiography using the deuterium contrast method. The experimental results showed that uptake of deuterium is faster than the discharge of deuterium in the MEA under the same conditions, indicating that the proton transfer mechanism is dominated by the hopping mechanism rather than the vehicle mechanism.

A part of this work was submitted for publication [120].

7.1 Experimental setup

The MEA preparation was the same as mentioned in Chapter 6. The platinum loading of the electrodes was $1.00 \pm 0.05 \text{ mg cm}^{-2}$. The acid doping level of the doped membrane with a thickness of $85 \pm 2 \text{ }\mu\text{m}$ was $15 \pm 1 \text{ mg cm}^{-2}$ (corresponding to a total absorption of about 420 wt.-% or 16.6 M). The cell assembly was the same as mentioned in Chapter 6. Before recording the polarization curve and performing the in-operando neutron radiography and impedance spectroscopy, a classical break-in procedure was carried out [77]. Subsequently, the cell was used at the Helmholtz Center Berlin for in-operando neutron radiography. Figure 7.1 shows how the cell was located in the beam. The cell was operated at a different current density (200 mA cm^{-2} , 400 mA cm^{-2} and 600 mA cm^{-2}) and stoichiometry ($\lambda_{\text{an/ca}} = 2/2$, $2/4$ and $2/6$). Its operating temperature was $160 \text{ }^{\circ}\text{C}$ with ambient pressure at the exit. In this work, dry gasses (dew point $-40 \text{ }^{\circ}\text{C}$) were supplied, and co-flow was used for all experiments.

During the in-operando measurements, a mobile single cell test station which was built at the Forschungszentrum Jülich with the electronic load ZS1806 (Höcherl & Hackl GmbH) applied to monitor and control the operating condition of the cell. During the experiment with a neutron beam, the supplied anode gas was changed between H_2 and D_2 from time to time. To be more specific, the

gas was switched between H_2 and D_2 every 30 minutes at 200 mA cm^{-2} , every 20 minutes at 400 mA cm^{-2} and every 15 minutes at 600 mA cm^{-2} . The experimental setup of the in-operando neutron radiographic measurement of the cell is depicted in Figure 2.8.

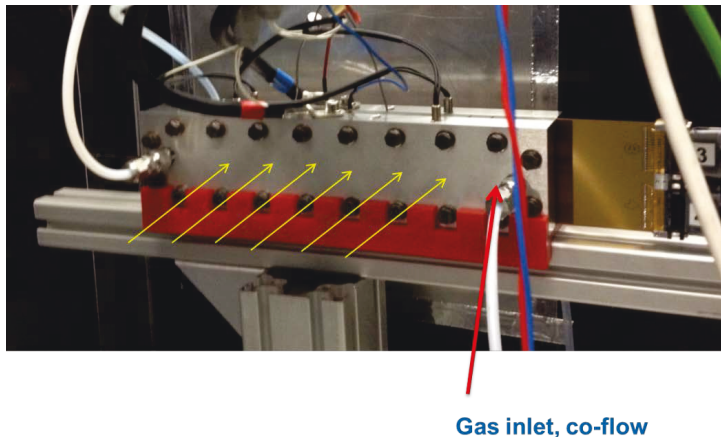


Figure 7.1: The photograph of the cell located in the neutron beam. Yellow arrows represent the beam direction which was in-plane of the cell. The gas flow orientation was from right to left.

The EIS measurement of the cell was conducted as mentioned in Chapter 5 except that AC signal voltage amplitude of $\pm 10 \text{ mV}$ was chosen.

7.2 Results and discussions

7.2.1 Cell performance and EIS

Figure 7.2 shows the overview of cell voltage changes by switching from H_2 to D_2 and back under various current densities and cathode stoichiometries. At 200 mA cm^{-2} , the cell at the operating condition with deuterium shows a higher voltage, but lower voltages at 600 mA cm^{-2} . At 400 mA cm^{-2} , changes in the cell voltage cannot be observed. Moreover, an additional increase of the cell voltage was noted after increasing the stoichiometry of the cathode, as expected.

Figure 7.3 shows the polarization curves of the cell with hydrogen and deuterium as the anode gas supply separately measured at $\lambda_{\text{an/ca}} = 2/2$, $T=160^\circ\text{C}$. The polarization curve of the cell at the operating condition with deuterium gas is similar to that at the operating condition with hydrogen

as the anode gas. This is due to the isotopes (H and D) having very similar physical and chemical properties, which leads fuel cells to behave in an almost identical manner. However, when the cell was in the low current density range ($0 - 400 \text{ mA cm}^{-2}$), its voltage with deuterium is higher than that of the cell with hydrogen, which is converse when in the high current density range ($500 - 800 \text{ mA cm}^{-2}$). Especially, at open cell voltage (OCV), the voltage of the cell with deuterium is 0.034 V higher than that with hydrogen.

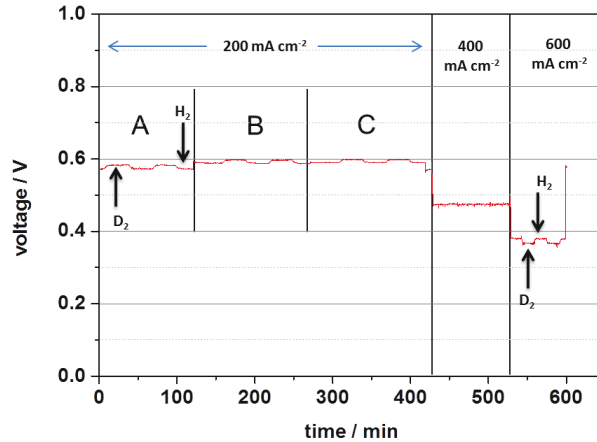


Figure 7.2: Changes in the cell voltage during the measurement time. Operating conditions for each part: 200 mA cm^{-2} (A): $\lambda_{\text{an}}/\text{ca}=2/2$; 200 mA cm^{-2} (B): $\lambda_{\text{an}}/\text{ca} = 2/4$; 200 mA cm^{-2} (C): $\lambda_{\text{an}}/\text{ca} = 2/6$; 400 mA cm^{-2} : $\lambda_{\text{an}}/\text{ca} = 2/2$; 600 mA cm^{-2} : $\lambda_{\text{an}}/\text{ca} = 2/2$.

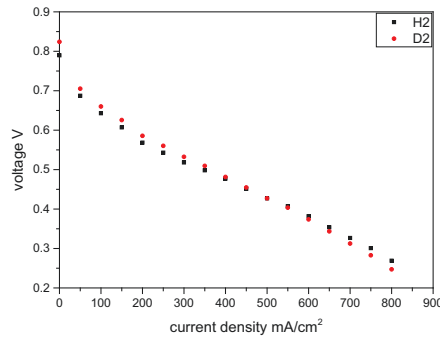


Figure 7.3: Polarization curves of the cell with H_2 and D_2 as anode gas supply at $\lambda_{\text{an}}/\text{ca} = 2/2$, $T = 160^\circ \text{C}$.

The different polarization curves between with H₂ and D₂ can be explained by the following equation:

$$E_{cell} = E_{Nernst} - R_{\Omega}j - \eta_{act} - \eta_{trans} \quad (7.1)$$

where E_{cell} is the cell voltage, E_{Nernst} is the Nernst voltage, R_{Ω} is the ohmic resistance of the cell, j is the current of the cell, and η_{act} and η_{trans} are the voltage loss by the activation and mass transport separately. At low current conditions, the voltage loss is mainly dominated by the activation polarization. With increasing current, the ohmic loss dominates and the mass transport limitations can be observed at very high current densities. In the visualization experiments presented here, the current density range spanned from 200 mA cm⁻² to 600 mA cm⁻². The mass transport losses did not play a major role and were neglected in further considerations (see Figure 7.3 for measured polarization curves) [121] (Page 102-104). When the current is zero, the cell voltage corresponds to the open cell voltage.

Furthermore, the theoretical open cell voltage can be calculated by the Nernst equation as follows:

$$E_{Nernst} = E_0 - \frac{RT}{2F} (\ln X_{H_2O} - \ln X_{H_2} - 0.5 \ln X_{O_2}) \quad (7.2)$$

where E_0 is the standard potential of the reaction (1.3); X_{H_2O} , X_{H_2} and X_{O_2} are the mole fractions of product and reactants in gas phase; R and F are the gas constant and Faraday constant respectively, T (K) is the cell temperature.

Additionally, the standard potential can be calculated by the equation as following:

$$E_0 = -\frac{\Delta G}{nF} \quad (7.3)$$

where ΔG is the Gibbs free energy, F is the Faraday constant and n is the molar value of the transferred electrons (here, $n = 2$). Based on the equation (7.3) and thermodynamic data [122-124], the standard potentials of the electrochemical reaction (1.3) can be calculated as shown in Table 7.1. In addition, due to the isotope effect, the mole fractions of product and reactants of H₂/¹/₂O₂ reactions and D₂/¹/₂O₂ reactions are identical. The cell temperature was stable at 160 °C. Thereby, the OCV of the cell would be only influenced by the standard potential based on the equation (7.2). It can be seen from Table 7.1 that the standard potential of D₂/¹/₂O₂ reactions is always around 0.030 V higher than the potential of H₂/¹/₂O₂ reactions, independent of the phase of the production. This

means the OCV of the cell with deuterium should be around 0.030 V higher than that with hydrogen at 25 °C and atmospheric pressure, which is in a good agreement with the measured data shown in Figure 7.3.

Table 7.1: Thermodynamic data [122-124] and calculated standard voltages of different reactions for 25 °C and ambient pressure.

Reaction	$\Delta G / \text{KJ mol}^{-1}$	E_0 / V
$\text{H}_2 + 0.5 \text{O}_2 \rightarrow \text{H}_2\text{O (liq.)}$	-237.18	1.229
$\text{H}_2 + 0.5 \text{O}_2 \rightarrow \text{H}_2\text{O (gas)}$	-228.59	1.185
$\text{D}_2 + 0.5 \text{O}_2 \rightarrow \text{D}_2\text{O (liq.)}$	-243.44	1.262
$\text{D}_2 + 0.5 \text{O}_2 \rightarrow \text{D}_2\text{O (gas)}$	-234.54	1.215

In equation (7.1), when the current is not zero, the ohmic resistance of the cell should be taken into account. Based on the EIS results which were separately recorded for the cell at 200 mA cm⁻² and 160 °C with H₂ and D₂ as shown in Figure 7.4, the ohmic resistance of the cell with H₂ is about 101.65 mohm cm² and the value with D₂ is roughly 115.80 mohm cm². The higher ohmic resistance of the cell with D₂ could contribute a bigger slope of the polarization curve based on the equation (7.1) as shown in Figure 7.3.

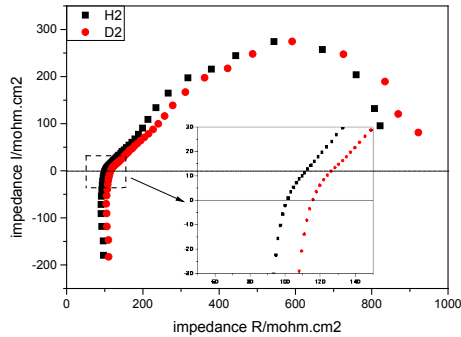


Figure 7.4: Impedance spectra of the cell measured at 200 mA cm⁻², $\lambda_{an}/ca = 2/2$, $T = 160^\circ\text{C}$, frequency range from 100 kHz to 100 mHz, the AC amplitude is 10 mV.

7.2.2 Determination phosphoric acid content

As shown in Figure 7.2, the anode gas supply was switched between H_2 and D_2 twice at different operating conditions of the cell. The second switchover was used to check the repeatability of the experiment and thereby the reliability of the presented results. With the different attenuation coefficient of phosphoric acid and deuterated phosphoric acid, radiographs of the cell operated with H_2 show different transmittances than those of the cell while operating with D_2 . The attenuation coefficients for different materials are displayed in Table 7.2 [125].

Table 7.2: The attenuation coefficients for different materials [125].

Materials	μ / cm^{-1}
H_3PO_4	2.972
D_3PO_4	0.075
$H_4P_2O_7$	2.182
$D_4P_2O_7$	0.056

The thickness of the phosphoric acid layer in the MEA can be calculated by using Beer-Lambert law. The equation is shown below:

$$I_t = I_0 \exp(-\sum_i \mu_i z_i) \quad (7.4)$$

where I_t is the transmitted intensity of the beam, I_0 is the incident intensity of the beam, i represents different layer of various materials, μ_i is the attenuation coefficient of each layer and z_i is the corresponding thickness of each layer.

During the switchover between H_2 and D_2 , the only change in the cell was that H was replaced by D and vice versa. It was assumed that there was only H_3PO_4 inside the cell and the thickness of H_3PO_4

layer would not change during the switchover. Therefore, the thickness of H_3PO_4 can be finally calculated by the contrast of H and D based on the equation (7.4) as follows:

$$z = \frac{1}{\mu_D - \mu_H} \ln \frac{I_H}{I_D} \quad (7.5)$$

where z is the thickness of H_3PO_4 layer, μ_H and μ_D are the attenuation coefficients of H_3PO_4 (2.972 cm^{-1}) and D_3PO_4 (0.075 cm^{-1}) respectively, I_H and I_D are the average transmitted intensity of the beam for H_2 and D_2 operation respectively. I_H and I_D can be read from Figure 7.5 as 0.243 a.u. and 0.250 a.u. respectively. The calculated thickness of phosphoric acid layer is $98.03 \text{ }\mu\text{m}$, which is in a good agreement with the membrane thickness of $85 \pm 2 \text{ }\mu\text{m}$ as measured before cell assembly. As mentioned in Section 3.2.5, the PBI typed membrane can be protonated by doping with phosphoric acid [82]. Thus, during the exchange from H_2 operation to D_2 operation, the membrane can be deuterated as well. The extra $10 \text{ }\mu\text{m}$ phosphoric acid layer can be contributed by the deuterated membrane or the phosphoric acid in the catalyst layer.

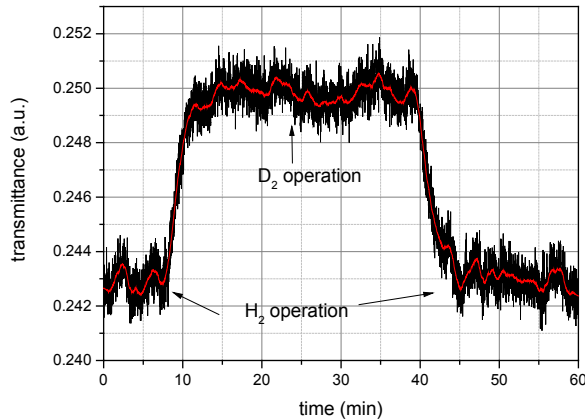


Figure 7.5: The transmittance of the cell at the first switching circle (H_2 - D_2 - H_2). The red line is the smoothed result of the transmittance.

All neutron images displayed here were normalized with respect to a cell operating with H_2 . Consequently, areas where H^+ is exchanged by D^+ , especially those areas that contain phosphoric acid or liquid water, are visible. The time signature shown in the radiographs represents the time

interval between the moment of switching the anode gas at the 3-way valve and the moment of the radiograph's exposure.

7.2.3 Overall H/D exchange process in the MEA

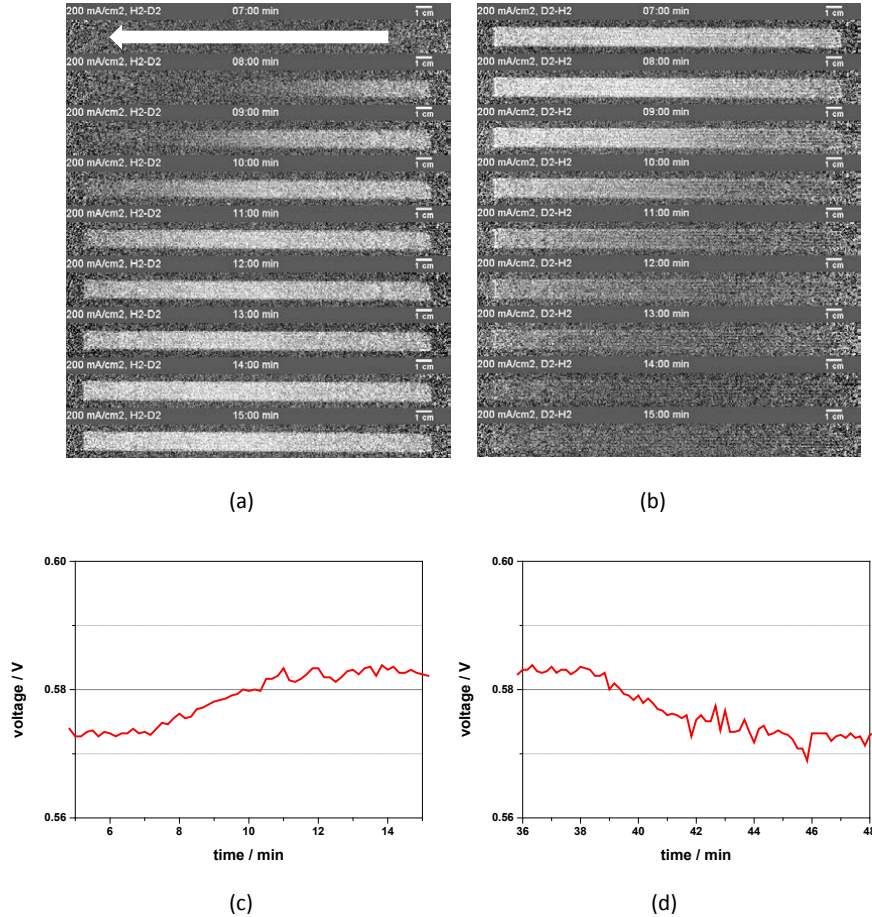


Figure 7.6: (a) and (b) show radiographs of the cell after the switchover from H-to-D and D-to-H, respectively. The direction of the white arrow in (a) is the gas flow orientation; (c) and (d) show the changes of cell voltage after the exchange of H-to-D and D-to-H (magnification of Figure 7.2) corresponding to the radiographs, above.

Figure 7.6 gives an overview of the impact of the changeover between H₂ and D₂ within the cell operating at 200 mA cm⁻² and $\lambda_{\text{an}}/\text{ca}=2/2$. The time shown in the first image of Figure 7.6 (a) and (b)

indicates that it takes roughly 7 minutes for the anode gas to flow through the cell from the 3-way valve, which is determined by the gas flow rate and length of the gas tube. In Figure 7.6 (a), from top to bottom, it can be observed that the exchange of H-to-D (images getting brighter) occurs along the gas orientation (from right to left) gradually. After 5 minutes, the changeover from H-to-D has almost finished. In contrast, 5 minutes after the first visible effects due to the exchange of D-to-H (shown in Figure 7.6 (b)), some parts of the active area are still brighter than the non-active area, which implies that there remains some deuterium in the MEA. Furthermore, simultaneous changes of the cell voltage (Figure 7.6 (c) and (d)) can be observed, which also indicates the exchange time of H-to-D and D-to-H. In general, the H-to-D exchange proceeds faster (5-6 minutes) than the D-to-H exchange (7-8 minutes). Additionally, in the previous work [66], the cell performance was poor and the H/D exchange time was short (time of H-to-D exchange process was 108-138s; time of D-to-H exchange process was 144-174s), which can be explained by the lower phosphoric acid content (up to 70 μm of the phosphoric acid layer) in the cell.

7.2.4 Models of the substitution between H and D

In order to quantitatively explain the different exchange time of H-to-D and D-to-H, some models were built. Before building the models, some general theory, assumptions and calculations should be made.

Firstly, as mentioned in the section of 2.1.3, phosphoric acid is recognized as the main electrolyte in the PBI/ H_3PO_4 system. Two types of proton transport mechanisms in phosphoric acid were recognized [43, 45, 47, 126, 127], the Grotthuss mechanism and the vehicular mechanism. However, in the case of the vehicular mechanism, the exchange process between H and D should have no obvious difference, because of the very small change in the total mass of the phosphoric acid molecule (vehicle). Thus, the Grotthuss mechanism should be mainly considered for the description of the proton transport inside the phosphoric acid-doped PBI membrane.

Additionally, it is assumed that all the H in phosphoric acid molecules would be replaced by D after the exchange finishes, and vice versa. In the following models, the water effect is not be taken into account. It is assumed that only pure phosphoric acid exists in the active area of the cell. Also, the current density is assumed to be homogeneous in the whole active area.

Furthermore, based on the above assumptions, the amount of positive charge carriers (protons or deuterons) in 1 cm^2 of the active area can be calculated by the amount of phosphoric acid uptake as follows:

$$N = \frac{3m_{PA}N_A}{M_{PA}} = 2.764 \times 10^{20} \text{ cm}^{-2} \quad (7.6)$$

N	cm^{-2}	the amount of positive charge carriers in 1 cm^2
m_{PA}	g cm^{-2}	the mass of phosphoric acid uptake (nearly 0.015 g cm^{-2})
M_{PA}	g mol^{-1}	the molar mass of phosphoric acid (98 g mol^{-1})
N_A	mol^{-1}	the Avogadro constant ($6.02 \times 10^{23} \text{ mol}^{-1}$)

In addition, the total amount of electric charge exchanged in 1 s at 200 mA cm^{-2} can be calculated as follows:

$$N' = IC = 1.248 \times 10^{18} \text{ cm}^{-2} \text{ s}^{-1} \quad (7.7)$$

N'	$\text{cm}^{-2} \text{ s}^{-1}$	the amount of exchanged electric charges
I	A cm^{-2}	current density (0.2 A cm^{-2})
C	$\text{A}^{-1} \text{ s}^{-1}$	the constant of the amount of electrons in 1 A current within 1 s ($6.24 \times 10^{18} \text{ A}^{-1} \text{ s}^{-1}$)

Model 1

For model 1, there are some assumptions which are listed below:

- The exchanges of H-to-D and D-to-H are identical
- Until H is replaced by D completely, no D transports to cathode side of the cell (stable displacement)

Based on the assumptions, the exchange process of H-to-D in a small area of phosphoric acid layer can be illustrated as shown in Figure 7.7. The exchange process of D-to-H is identical.

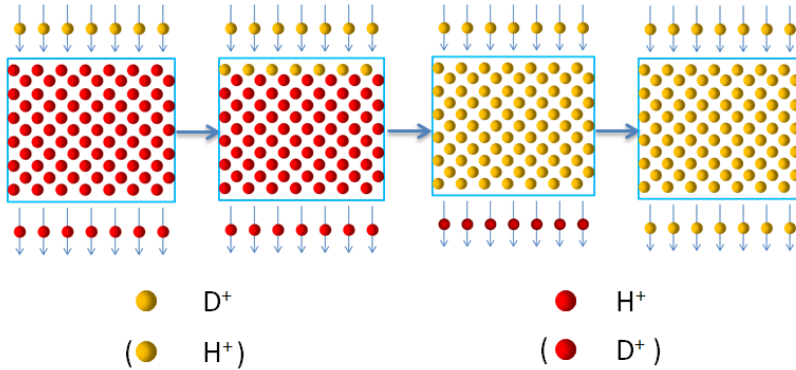


Figure 7.7: The scheme of the exchange process of H-to-D and D-to-H in model 1.

Therefore, the exchange time of H-to-D or D-to-H at 200 mA cm^{-2} can be calculated as follows:

$$t = \frac{N}{N'} \quad (7.8)$$

Combining equations (7.6) and (7.7), the exchange time can be calculated to be 3.68 minutes for 200 mA cm^{-2} . However, in a phosphoric acid molecule, there are three options of releasing the proton. When a phosphoric acid molecule is partially deuterated, the deuteron in the phosphoric acid replaced by incoming deuteron has no contribution for the total exchange of H-to-D, and vice versa. Thus, a further model should be built up.

Model 2

In this model, some further assumptions were made as following:

- The exchanges of H-to-D and D-to-H are identical as well.
- The effect of the H or D transport caused by the environment is neglected.
- Three steps of the substitution of a proton by a deuteron in a phosphoric acid molecule are assumed, and vice versa. Taking the exchange process of H-to-D as an example, the three steps are: (step 1) the molecule of H_3PO_4 accepts a deuteron and donates a proton simultaneously; (step 2) the molecule of DH_2PO_4 accepts a deuteron and donates a proton simultaneously; (step 3) the molecule of D_2HPO_4 accepts a deuteron and donates a proton simultaneously.

Based on the assumptions, some D would reach the cathode before all the H replaced by D as shown in Figure 7.8. Also, since the exchanges of H-to-D and D-to-H are identical, the exchange process of D-to-H is same as that of H-to-D.

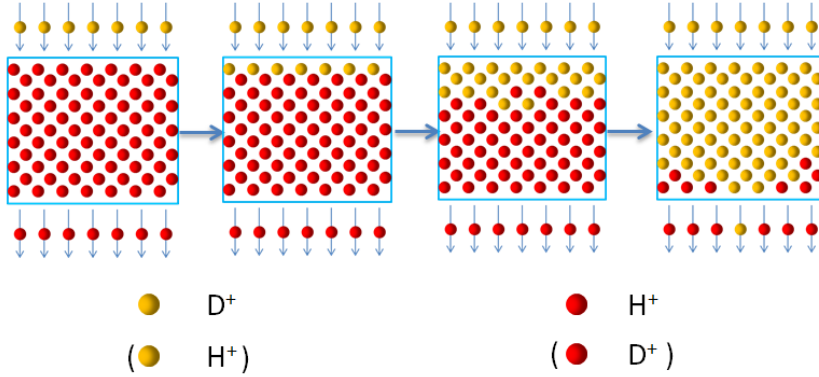


Figure 7.8: The scheme of the exchange process of H-to-D and D-to-H in model 2.

Furthermore, the substitution efficiencies of each step can be simply calculated based on statistical principles. For step 1, the efficiency of the substitution of a proton by a deuteron should be 100%. However, for steps 2 and 3, the efficiencies of the substitution are no longer 100%, because of the deuterons in the molecule may also be substituted by the deuteron, which has no contribution for the exchange process of H-to-D. Without taking the isotope effect into account, the efficiencies of the substitution for steps 2 and 3 should be 2/3 and 1/3 respectively.

Thus, the exchange times of H-to-D or D-to-H at 200 mA cm^{-2} for each step can be calculated as following:

$$t_{step1} = \frac{\frac{1}{3}N}{N' \times 100\%} \quad (7.9)$$

$$t_{step2} = \frac{\frac{1}{3}N}{N' \times \frac{2}{3}} \quad (7.10)$$

$$t_{step3} = \frac{\frac{1}{3}N}{N' \times \frac{1}{3}} \quad (7.11)$$

The total exchange time is the sum of each step, which is 6.75 minutes in this model. Without considering the substitution between H and D, this time also means the time which is needed to refresh all the H in the MEA at 200 mA cm^{-2} .

However, due to the isotope effect, the activation energy of deuteron transport is higher than that of proton transport. According to Mesmer et al. [128], the ionization coefficients of H_2PO_4^- and H_2O are about 2.9 times and 6.2 times higher than that of D_2PO_4^- and D_2O respectively at 150°C . Nowick et al. [129] measured the conductivities on various high temperature proton conductors by isotope effect and found that the activation energy of deuteron transfer was always 0.03-0.06 eV higher than that of proton transfer. Sluyters et al. [130] estimated the zero point energies of H^+ and D^+ in liquid water (or heavy water) along quantum mechanical routes and found the zero point energy of H^+ was around 2 times of the zero point energy of D^+ . Furthermore, Heres et al. [131] found the activation energy of deuteron transfer was always higher than that of proton transfer with varying water content in phosphoric acid, and additionally, the difference of the activation energy of proton and deuteron transferring increased with the water content. Additionally, the lower conductivity of deuterons transport compared to protons transport was proved in previous text (Figure 7.4). Thus, a further model should be made in order to distinguish the exchange processes of H-to-D and D-to-H.

Model 3

Compared with model 2, the exchanges of H-to-D and D-to-H are no longer identical. The transports of protons and deuterons are affected by the energy of OH and OD oscillators. The exchange process of this model should be similar as that of model 2, but with different exchange speed.

In this model, taking the exchange of H-to-D as example, the efficiency of the substitution of step 1 should be 100 % as well. However, for steps 2 and 3, the efficiencies are no longer 2/3 and 1/3 respectively due to the different probabilities of proton and deuteron transfer. According to the quantum tunneling principle and statistical principles, the probabilities of a proton being replaced by a deuteron in steps 2 and 3, as well as the efficiencies of steps 2 and 3, can be calculated as follows by equations (7.12) and (7.13) respectively.

$$p_{\text{step}2} = \frac{2Q_{\text{OH}}}{Q_{\text{OD}} + 2Q_{\text{OH}}} \times 100\% \quad (7.12)$$

$$p_{\text{step}3} = \frac{Q_{\text{OH}}}{2Q_{\text{OD}} + Q_{\text{OH}}} \times 100\% \quad (7.13)$$

where Q_{OH} and Q_{OD} are the energy of the OH and OD oscillators respectively.

Thus, the equations (7.10) and (7.11) can be rewritten as following:

$$t'_{step2} = \frac{\frac{1}{3}N}{N' \times p_{step2}} \quad (7.14)$$

$$t'_{step3} = \frac{\frac{1}{3}N}{N' \times p_{step3}} \quad (7.15)$$

Additionally, it was reported [126] that the energy of OH oscillator is about 60 meV higher than that of OD oscillator. Especially, the zero-point energy of the OH and OD oscillators are about 190 meV and 130 meV respectively. Applying the zero-point energy into the above equations, the total exchange time of H-to-D at 200 mA cm⁻² can be calculated and is about 5.73 minutes. Similarly, the exchange time of D-to-H is about 8.31 minutes. The results are in general agreed with the measured data (5-6 minutes for H-to-D and 7-8 minutes for D-to-H).

This model can explain the different exchange time of H-to-D and D-to-H processes very well based on the hopping mechanism. In future, the conductivities of natural phosphoric acid and deuterated phosphoric acid will be measured ex-situ at high-temperature (up to 180 °C) and the activation energies of proton and deuteron transport will be calculated separately, in order to make this model more accurate.

7.2.5 Local H/D exchange process of MEA

Figure 7.9 (a) shows the temporal evolution of the transmittance changes at the gas inlet region, the middle part of the active area and gas outlet region. Figure 7.9 (b) shows the local transmittance change rates of the H-to-D exchange process along the gas channel.

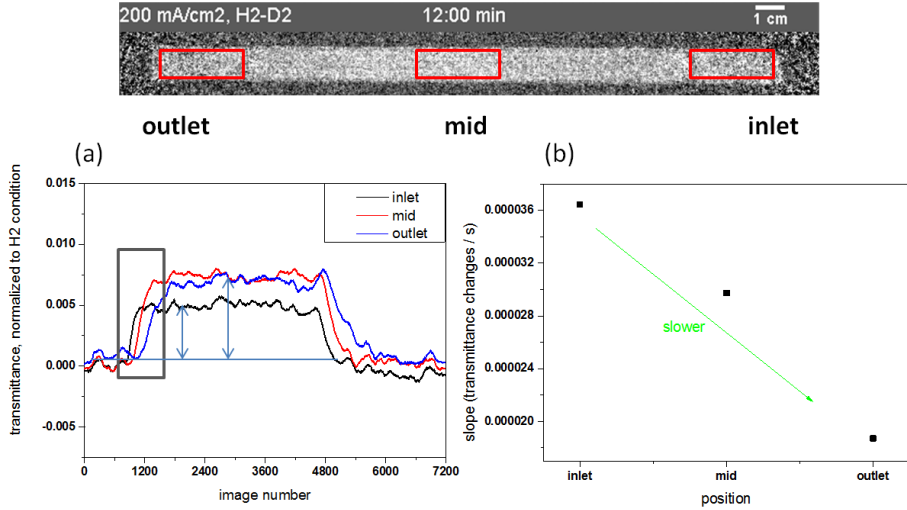


Figure 7.9: (a) The transmittance (average transmittance of the selected red rectangular area on the above radiograph) changes over time at the different position of the cell at 200 mA cm⁻², $\lambda_{\text{an}}/c_{\text{a}}=2/2$. (b) The transmittance changes rate of the H-to-D exchange process fitted by the curves in gray rectangle shown in (a).

In Figure 7.9 (a), it can be seen that the transmittance change due to H₂ and D₂ operation at the gas inlet region is smaller than that at the gas outlet region. This can be due to the local water vapor partial pressure along the channel, which was mentioned in chapter 6 and literature [132]. The water vapor partial pressure increases from inlet to outlet, which can cause the hydration and dehydration of phosphoric acid at the outlet and inlet, respectively. Equation (7.16) shows the dehydration (from left to right) and hydration (from right to left) processes of phosphoric acid.



If there was only H₃PO₄ (no water and H₄P₂O₇) in the MEA, the thickness of phosphoric acid at gas inlet region and gas outlet region can be calculated to be approximately 88 μm and 102 μm respectively based on the Beer-Lambert law. As mentioned before, the average thickness of phosphoric acid layer is about 98 μm. Assuming that there was no phosphoric acid redistribution along the membrane plane and the dehydration/hydration of phosphoric acid would not change the thickness of phosphoric acid, the calculated local thickness of phosphoric acid can be only affected by the dehydration/hydration of phosphoric acid. In the case of dehydration (at gas inlet region), the difference of attenuation coefficients of H₄P₂O₇ and D₄P₂O₇ is smaller than that of H₃PO₄ and D₃PO₄.

as shown in Table 7.2. This makes the difference in transmittance of H_2 and D_2 operation smaller at gas inlet as shown in Figure 7.9 (a). Similarly, in the case of hydration (at gas outlet region), the extra water can cause the increase of the transmittance due to the high contrast between H_2O and D_2O .

Figure 7.9 (b) demonstrates that the transmittance change rate of the H-to-D exchange process decreases along the gas orientation. This is caused by on one hand the local current density and on the other hand the local concentration of D_2 gas in the channel.

As discussed in Chapter 6, the local current density of the long cell decreases first and then increased along the gas flow orientation. And high current accelerates the exchange process, which will be discussed in the next section. In addition, during the exchange, the gas in the flow channel should be a mix of H_2 and D_2 , since there is no clear boundary between the different gas phases. Thus, there should be a D_2 gas concentration gradient (highest concentration at the inlet part and lowest concentration at the outlet part) on the anode side during the exchange. Because of the similar chemical properties of isotopes, the rate of the electrochemical oxidation reactions of $H_2 \rightarrow 2H^+ + 2e^-$ and $D_2 \rightarrow 2D^+ + 2e^-$ are assumed to be the same. Therefore, the higher D_2 concentration leads to a higher amount of D^+ ions, which means that more deuterons can be generated at anode side and transfer into the membrane at the gas inlet region than at the gas outlet region, and further enhance the probability of proton substitution by deuterons. Finally, it causes higher transmittance change rate at gas inlet.

7.2.6 Impact of different current density on H/D exchange process in the MEA

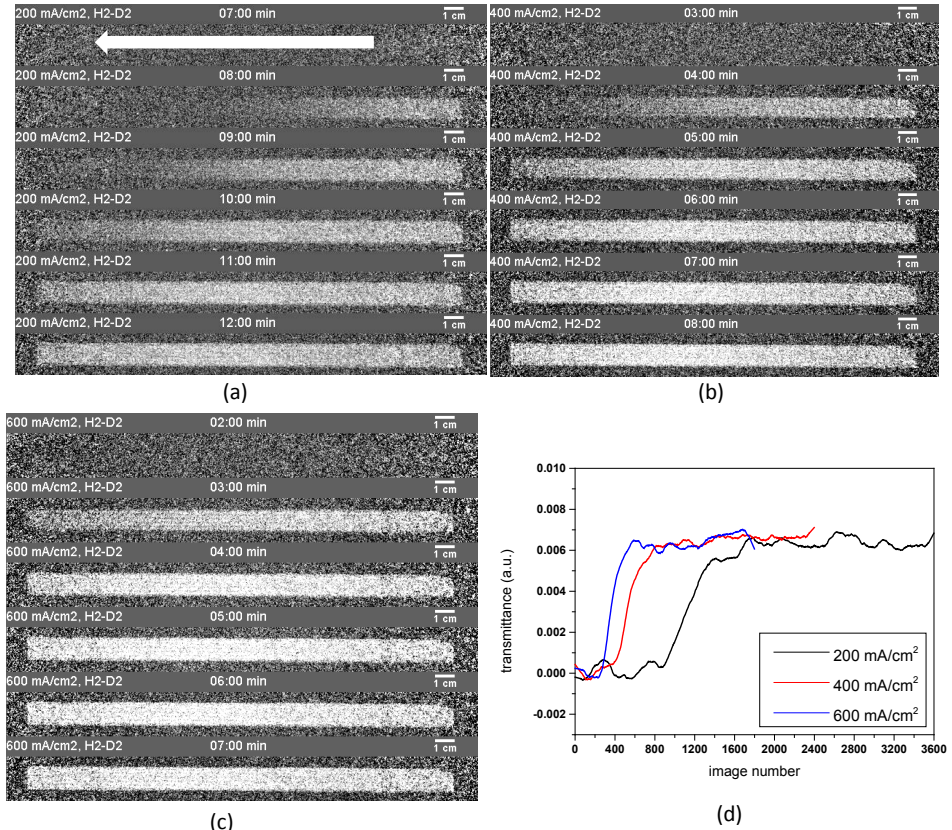


Figure 7.10: (a), (b) and (c) show radiographs of the cell after the switchover from H-to-D at current densities of 200 mA cm⁻², 400 mA cm⁻² and 600 mA cm⁻² respectively, but with identical stoichiometry $\lambda_{an/ca}=2/2$; (d) average transmittance changes for the entire active area of the cell, corresponding to the radiographs displayed here.

Figure 7.10 shows the radiographs and the average transmittance changes of the entire active area of the cell after switching from H₂ operation to D₂ operation at various current densities of 200 mA cm⁻², 400 mA cm⁻² and 600 mA cm⁻². This clearly reveals faster D₂ uptake for the higher current density of the cell, indicating that the current of the cell has a significant effect on the H/D exchange rate because of a higher amount of charge transfer over the same time period at a higher current density. Additionally, it can be noticed that the exchange times of H-to-D process at 200 mA cm⁻², 400 mA cm⁻² and 600 mA cm⁻² are 5-6 minutes, 2-3 minutes and 1-2 minutes, respectively, which

demonstrates an inverse relationship. Moreover, from Figure 7.10 (d), it can be seen that transmittance differences of the cell operated with H_2 and D_2 at various current density are approximately identical. This indicates that there is no significant change of the phosphoric acid amount or composition in the current density range of 200 mA cm^{-2} to 600 mA cm^{-2} . This is in agreement with the in-situ synchrotron X-ray radiography results [55].

7.2.7 Transmittance changes in dependent of different gas flow rates at the cathode

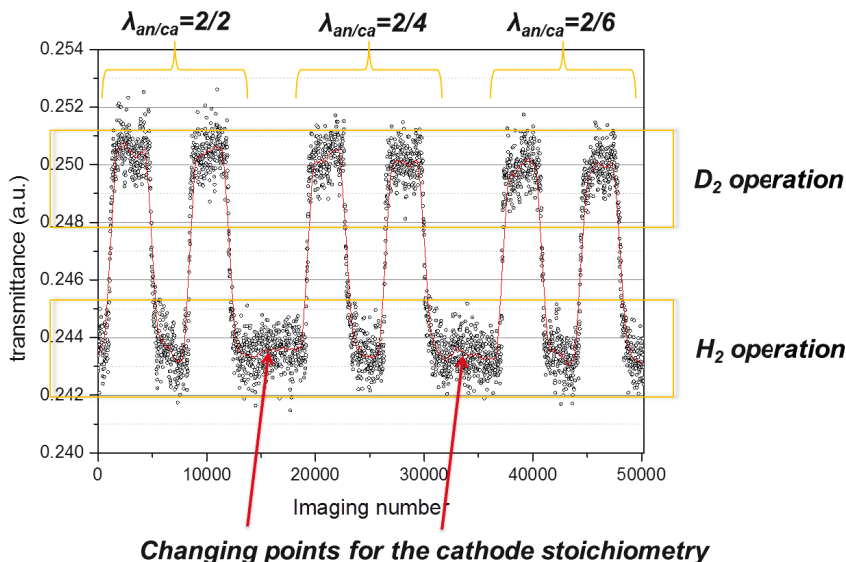


Figure 7.11: Transmittance of the whole active area of the cell over time with various cathode stoichiometries $\lambda_{an/ca}=2/2$, $\lambda_{an/ca}=2/4$ and $\lambda_{an/ca}=2/6$ at 200 mA cm^{-2} .

Figure 7.11 shows the transmittance of the whole active area of the cell over time at 200 mA cm^{-2} . During this, the anode gas was switched between H_2 and D_2 several times and the stoichiometry was set to $\lambda_{an/ca}=2/2$, $\lambda_{an/ca}=2/4$ and $\lambda_{an/ca}=2/6$ separately. The lower level of transmittance represents the H_2 operating condition and the higher level of transmittance represents the D_2 operating condition. With increasing stoichiometry of air at the cathode side, the transmittance of the whole active area of the cell with H_2 operation remained almost stable, but with D_2 operation decreased.

It is well known in literature [38, 55] and also demonstrated by the calculation of the thickness of the phosphoric acid layer in previous section (7.3), that some quantity of phosphoric acid exists in the catalyst layer during cell operation. Maier et al. [55, 56] demonstrated that the phosphoric acid doped membrane had roughly 20% swelling during the hydration/dehydration of phosphoric acid. Eberhardt et al. [133] observed phosphoric acid droplets in anodic gas diffusion layer of an operating HT-PEFC by synchrotron based X-ray tomographic microscopy. Thomas [134] suggested that at high current densities the phosphoric acid migrated from the cathode to anode and back-diffused at low current densities.

In the present work, the increase in the stoichiometry of air at the cathode side had no detectable changes on the transmittance of the cell with H_2 operation, but led to a decrease of transmittance of the cell with D_2 operation. One possible explanation for this phenomenon is that phosphoric acid redistribution took place in parallel to the membrane plane in catalyst layers. The possible phosphoric acid redistribution in the cathodic catalyst layer is shown in the Figure 7.12.

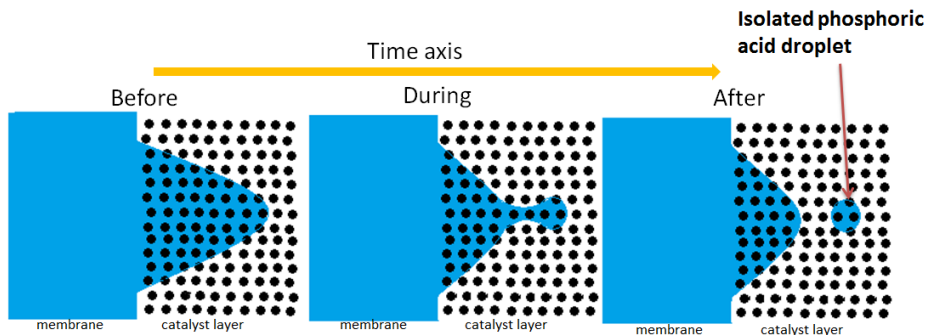


Figure 7.12: The possible phosphoric acid redistribution principle in the cathodic catalyst layer by increasing the gas flow rate at cathode.

After increasing the stoichiometry, the higher flow rate of dry gas will dehydrate the MEA. In the meantime, the membrane sucks phosphoric acid from the catalyst layer in order to fill the voids generated by losing water. However, due to the high viscosity of concentrated phosphoric acid, some acid could not move and then forms a neck-type phosphoric acid path. Finally, the acid path disconnects at the neck part and generates an isolated phosphoric acid droplet for the charge transfer in the catalyst layer. Furthermore, it is worth noting that the stoichiometry at cathode was

increased during H_2 operation. This means that the isolated phosphoric acid droplets were protonated. Thus, the isolated and protonated phosphoric acid droplets have no influence on the transmittance with H_2 operation. However, after switching the anodic gas to D_2 at a higher cathodic gas flow rate, deuterons could hardly be transported to the isolated phosphoric acid droplets. The isolated acid droplets will stay protonated even when the cell is operated with D_2 gas. Due to the higher attenuation coefficient of H_3PO_4 than that of D_3PO_4 , the existence of the protonated phosphoric acid droplets made the transmittance of the cell operated with D_2 at higher cathode stoichiometry lower than that at lower cathode stoichiometry.

7.2.8 Difference of MEA between under channels and ribs of flow field

In order to distinguish the MEA under channels and ribs of the flow field, 3D surface plots were made based on the transmittance of the radiographs of the cell with H_2 and D_2 operation separately. The radiographs were normalized with respect to the cell operating with H_2 . The final surfaces plots of the active area of the cell were shown in Figure 7.13.

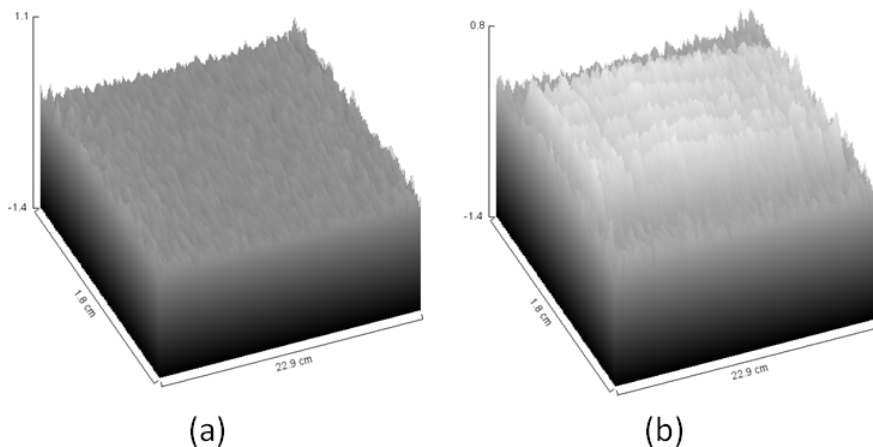


Figure 7.13: 3D surface plots of the radiographs of the cell with H_2 (a) and D_2 (b) operation normalized by H_2 operation condition.

As shown in Figure 7.13 (a), the surface plot of the radiograph of the cell with H_2 operation is almost flat. But, when the cell switched to D_2 operation as shown in Figure 7.13 (b), the active area of the

cell is visible. Furthermore, it can be noted that there are five parallel higher transmittance chains, which should represent the transmittance of the MEA under channels of the flow field. The higher transmittance difference between H_2 and D_2 operation under channels primarily indicates that the thickness of phosphoric acid layer under channels is higher than that under the ribs. Moreover, phosphoric acid mainly exists in the membrane. Thus, it can be deduced that the membrane under channels is thicker than under the ribs of the flow field. This is in a good agreement with the data shown in Chapter 5.

7.3 Summary

In this chapter, a high temperature polymer electrolyte fuel cell based on a phosphoric acid-doped PBI membrane with five straight long gas channels on a flow field was investigated under different operating conditions by neutron radiography using the deuterium contrast method. The main results are listed as follows:

- The uptake of deuterium is faster than the discharge of deuterium during the switchover under same condition. The different substitution rate of H-to-D and D-to-H indicate the hopping mechanism of proton transfer in an operando HT-PEFC.
- The different substitution rate of H-to-D and D-to-H was due to the different activation energies of protons and deuterons transport. The different exchange times were quantitatively explained by self-built models.
- The higher exchange rate of H and D is found at gas inlet than that at gas outlet. The local exchange of H and D is very complex and influenced by the local conditions of the MEA, such as local current density distribution, gas concentration (mixed of H_2 and D_2 during the exchange) at anode side.
- Current density has significant impact on the exchange time. An inversely proportional relationship between the exchange time and current density exists.
- High gas flow rate can cause dehydration of MEA, which results in the phosphoric acid redistribution in the catalyst layer.

8 Discussion

The system of $\text{PBI-H}_3\text{PO}_4\text{-H}_2\text{O}$ was investigated with the ex-situ and in-situ experiments.

In the doping experiments (ex-situ, Chapter 3), m-PBI membranes were used to conduct the experiments at various temperatures and acid concentrations in solution. In the case of temperature variation, it was found that the acid concentration in polymer decreased first and then increased with the increase of temperature in all cases of acid concentration in solution. This is because, with the increase of temperature, the water uptake increases first and then decreases, while the acid doping level increases in the whole range of temperature. In the case of acid concentration variation in solution, it was found that the acid concentration in polymer increased first and then decreased with the increase of acid concentration in solution. This is in good agreement with other reports [70, 83]. The reason of this effect is that the water uptake stays nearly constant in low acid concentration range in solution and increases dramatically in the high acid concentration range in solution, while the acid doping level increases in the whole range of the acid concentration range in solution. The proton conductivity of phosphoric acid doped PBI membrane is not only dependent on the acid doping level, but also the water content inside the membrane. When the phosphoric acid content was constant, the proton conductivity of phosphoric acid was quite sensitive to the water vapor partial pressure. In the local current density distribution measurement (in-situ, Chapter 6), it was found that the water vapor partial pressure which is associated with the acid concentration in the membrane along the channel may have significant effect on the local current density distribution. The water vapor partial pressure along the gas flow orientation was estimated from 0-210 mbar. This is in good agreement with the literature [132], in which the water vapor partial pressure at cathode gas outlet was also estimated to roughly 170 mbar with average current density of 200 mA cm^{-2} and cathodic stoichiometry of 2 when the water transport from cathode to anode through membrane was taken into account. In this work, the water vapor partial pressure from 0-210 mbar corresponds to an acid concentration range of 76 wt.-% of P_2O_5 to 68 wt.-% of P_2O_5 (seeing Figure 12.2 in [43]) at 160°C . At this temperature, the proton conductivity can be highly

affected by the concentration of phosphoric acid. With the increase of acid concentration, the proton conductivity will decrease sharply (seeing Figure 12.7 in [43]). All this is reflected by the significant increase of local current density at gas outlet where the oxygen concentration is lowest but water vapor partial pressure is highest. Additionally, it is worth to mention that one of previous works from our department demonstrated [116] that the local current density of the cell along the gas flow orientation increased first and then decreased (which was the opposite effect to the result in this work) after long-term test (up to 350 h operation), which was attributed to the faster degradation of the MEA at gas inlet and outlet regions.

In the dissolution experiments (ex-situ, Chapter 4), it was found that both non-crosslinked AB-PBI and crosslinked AB-PBI can partially or entirely dissolve into phosphoric acid solution depending on the temperature and phosphoric acid concentration. The dissolution of m-PBI membrane in phosphoric acid solution was also found in the literature [104]. In this report, researchers doped membranes at different temperatures and they found that the thermally cured PBI membranes exhibited good flexibility and sufficient mechanical strength even with high acid doping level while the non-cured PBI membrane was completely dissolved when doping in 85 wt.-% phosphoric acid at 100 °C. They demonstrated that the thermal treatment affected the structural order within the membrane, which made part of membrane change from amorphous to crystalline. Additionally, the solubility of PBI typed materials in phosphoric acid solution proves the possibility of direct casting membranes by a so-called polyphosphoric acid (PPA) process [135]. Membranes obtained by PPA casting had much higher acid doping levels and larger water uptake values than those prepared from a methane sulfonic acid solution (MSA casting) or DMAc casting. Furthermore, the solubility of PBI membrane in phosphoric acid can be related to the degradation of doped membrane in an operando HT-PEFC. Additionally, in this work, it can be noticed that there was no obvious weight loss in subsequent dissolution experiment after the first washing process. One possible reason was the washing process affecting the structural order within the membrane.

In the long-term single cell test experiments (in-situ, Chapter 5), it was found that the ohmic resistance of the cells decreased while the charge transfer resistance and mass transport resistance generally increased after long-term tests. The decrease of ohmic resistance was related to the membrane thinning effect caused by the dissolution of the membranes into phosphoric acid; the increase of the charge transfer resistance might be due to the migration of the dissolved membrane materials into the catalyst, which reduces the active area of the catalyst layer. Further post analysis

by SEM and EDX proved the facts of membrane thinning and catalyst adhering on both side of membrane. By reverse thinking, the existence of water may reduce the dissolution rate of membrane into phosphoric acid. Thus, when a cell was operated with a load cycling (with high load, more water is produced.), the membrane thinning, as well as membrane dissolution, could slow down without resulting in too much phosphoric acid loss [136].

In the operando neutron radiograph experiments (in-situ, Chapter 7), different exchange time of H-to-D and D-to-H was found when the anode gas was switched between H_2 and D_2 . This was also found in the previous work [66]. However, in previous work, due to the high degradation of the cell, the phosphoric acid amount in the MEA was hard to determine. Thus, the quantitative analysis of the H/D exchange processes was not given. In this work, a quantitative model was built to analyze the different exchange processes of H-to-D and D-to-H based on a hopping mechanism rather than a vehicle mechanism for proton transfer in the phosphoric acid doped PBI membrane applied in HT-PEFC. Furthermore, the possible phosphoric acid redistribution, which took place in parallel to the membrane plane on the cathode side during the stoichiometry change, might be the mechanism for phosphoric acid loss. In the catalyst layer, gases diffuses from GDL to three phase boundary where the water is generated. The counter flow of generated water vapor path and is absorbed by the isolated phosphoric acid droplets. The mobility of phosphoric acid is increased by absorbing water and it moves out of the cell with the water vapor. Further experiments of stoichiometry cycling could be done to investigate the phosphoric acid loss rate in future.

9 Conclusion

In the present work, the interactions among the system of PBI-H₃PO₄-H₂O were studied by various ex-situ and in-situ experiments. The doping behavior of the PBI membrane in phosphoric acid, the degradation mechanism of the membrane, the local current density distribution and the proton transport mechanism inside the membrane were investigated. According to previous results and discussions, the following conclusions are obtained:

- i. The doping process of PBI membrane with phosphoric acid can be influenced by doping temperatures and acid concentration in solutions. The water uptake of the membrane slightly increases in a range of 30 – 70 °C but dramatically decreases in the range of 70 – 110 °C, while the acid doping level increases in the whole range of doping temperature. The acid doping level and water uptake increase in the range of acid concentration of 1.66 – 14.67 M in solutions. The water uptake is independent of acid absorption in an acid concentration range of 0 – 6 M. But in the case of high acid concentration in solutions, the water uptake is associated with the acid absorption. Additionally, crosslinking with DBX of PBI membranes generally benefits the acid doping level and water uptake. The restriction of volumetric swelling makes the acid absorption and water uptake of crosslinked membranes lower than those of non-crosslinked membranes at high acid concentration.
- ii. PBI membranes can partially or entirely dissolve into phosphoric acid solution depending on the temperature and phosphoric acid concentration. The dissolution of membranes in phosphoric acid could be one of the degradation mechanisms of the membrane when used in HT-PEFCs.
- iii. The local current density distribution is very complex and can be affected by various local conditions such as temperature, catalyst loading, oxygen concentration and water vapor partial pressure. Despite the effect by cell design and operation condition, the current density distribution can be co-affected by oxygen concentration and water vapor partial pressure. At gas inlet, the local condition of the MEA is with highest oxygen concentration

- and lowest water vapor partial pressure, which is opposite at gas outlet. This finally makes the local current density along the gas flow orientation decrease first and then increase.
- iv. The different exchange time of H-to-D and D-to-H observed by neutron radiographs when the anode gas switching between H_2 and D_2 reflect a hopping mechanism rather than a vehicle mechanism for proton transfer in the phosphoric acid doped PBI membrane used in HT-PEFC. A model was built up to estimate the exchange time of H-to-D and D-to-H processes. The exchange time of H-to-D at 200 mA cm^{-2} was calculated as 5.73 minutes which is 5-6 minutes in experiment; the exchange time of D-to-H at same condition was calculated as 8.31 minutes which is 7-8 minutes in experiment.

Bibliography

- [1] S.A. Montzka, E.J. Dlugokencky and J.H. Butler, *Non-CO₂ greenhouse gases and climate change*. Nature, 2011. **476**: p. 43.
- [2] N. Armaroli and V. Balzani, *The future of energy supply: Challenges and opportunities*. Angewandte Chemie, 2007. **46**(1-2): p. 52-66.
- [3] S. M. J. Zaidi and M. A. Rauf, *Fuel cell fundamentals*, in: S. M. J. Zaidi, T. Matsuura (Eds.), *Polymer Membranes for Fuel Cells*, Springer, New York, 2009.
- [4] F. Barbir, *PEM Fuel Cells*, in : N. Sammes (Ed.), *Fuel Cell Technology: Reaching Towards Commercialization*, Springer, London, 2006.
- [5] C. Wannek, I. Konradi, J. Mergel and W. Lehnert, *Redistribution of phosphoric acid in membrane electrode assemblies for high-temperature polymer electrolyte fuel cells*. International Journal of Hydrogen Energy, 2009. **34**(23): p. 9479-9485.
- [6] Q. Li, J.O. Jensen, R.F. Savinell and N.J. Bjerrum, *High temperature proton exchange membranes based on polybenzimidazoles for fuel cells*. Progress in Polymer Science, 2009. **34**(5): p. 449-477.
- [7] J.S. Wainright, J.-T. Wang, D. Weng, R.F. Savinell and M. Litt, *Acid-doped polybenzimidazoles a new polymer electrolyte*, The Journal of Electrochemical Society, 1995. **42**(7): p. 121-123.
- [8] M. Carmo, D.L. Fritz, J. Mergel and D. Stolten, *A comprehensive review on PEM water electrolysis*. International Journal of Hydrogen Energy, 2013. **38**(12): p. 4901-4934.
- [9] M. Ni, D.Y.C. Leung and M.K.H. Leung, *A review on reforming bio-ethanol for hydrogen production*. International Journal of Hydrogen Energy, 2007. **32**(15): p. 3238-3247.
- [10] J.R. Rostrup-Nielsen, J. Sehested and J.K. Nørskov, *Hydrogen and synthesis gas by steam- and CO₂ reforming*, in *Advances in Catalysis 2002*, Academic Press. p. 65-139.
- [11] G.A. Camara, E.A. Ticianelli, S. Mukerjee, S.J. Lee and J. McBreen, *The CO Poisoning Mechanism of the Hydrogen Oxidation Reaction in Proton Exchange Membrane Fuel Cells*. Journal of the Electrochemical Society, 2002. **149**(6): p. A748.
- [12] H.P. Dhar, L.G. Christner and A.K. Kush, *Nature of co adsorption during H₂ oxidation in relation to modeling for co poisoning*. The Journal of Electrochemical society: Electrochemical Science and Technology, 1987. **134**(12): p. 3021-3026.
- [13] S. Gottesfeld and J. Pafford, *A new approach to the problem of carbon monoxide poisoning in fuel cells*, The Journal of Electrochemical Society: Accelerated Brief Communication, 1988. p. 2651-2652.
- [14] B. Xing and O. Savadogo, *The effect of acid doping on the conductivity of polybenzimidazole PBI*. Journal of New Materials for Electrochemical Systems, 1999. **2**: p. 95-101.
- [15] S.R. Samms, S. Wasmus and R.F. Savinell, *Thermal Stability of Proton Conducting Acid Doped Polybenzimidazole in Simulated Fuel Cell Environments*, The Journal of Electrochemical Society, 1996. **143**(4): p. 1225-1232.
- [16] L. Xiao, H. Zhang, T. Jana, E. Scanlon, R. Chen, W.-W. Choe, L.S. Ramanathan, S. Yu and B.C. Benicewicz, *Synthesis and Characterization of pyridine-based polybenzimidazoles for high temperature polymer electrolyte membrane fuel cell applications*, Fuel Cells, 2004. **5**(2): p. 287-295.

- [17] A. Chandan, M. Hattenberger, A. El-kharouf, S. Du, A. Dhir, V. Self, B.G. Pollet, A. Ingram and W. Bujalski, *High temperature (HT) polymer electrolyte membrane fuel cells (PEMFC) – A review*. Journal of Power Sources, 2013. **231**: p. 264-278.
- [18] H. Vogel and C.S. Marvel, *Polybenzimidazoles, new thermal stable polymers*, Journal of Polymer Science, 1961. p. 511-539.
- [19] Y. Iwakura, K. Uno and Y. Imai, *Polyphenylenebenzimidazoles*, Journal of Polymer Science: Part A, 1964. **2**: p. 2650-2615.
- [20] R. Kovar, F.E. Arnold, *Para-Orderd Polybenzimidazole*, Journal of Polymer Science: Polymer Chemistry Edition, 1976. **14**: p. 2807-2817.
- [21] P.E. Cassidy and N.C. Fawcett, *Thermally Stable Polymers: Polyoxadiazoles, Polyoxadiazole-N-Oxides, Polythiazoles, and Polythiadiazoles*. Journal of Macromolecular Science, Part C: Polymer Reviews, 1979. **17**(2): p. 209-266.
- [22] J.K. Kallitsis and N. Gourdoupi, *Proton conducting membranes based on polymer blends for use in high temperature PEM fuel cells*. Journal of New Materials for Electrochemical Systems, 2003. **6**: p. 217-222.
- [23] M.K. Daletou, N. Gourdoupi and J.K. Kallitsis, *Proton conducting membranes based on blends of PBI with aromatic polyethers containing pyridine units*. Journal of Membrane Science, 2005. **252**(1-2): p. 115-122.
- [24] L. Xiao, h. Zhang, E. Scanlon, L.S. Ramanathan, E.-W. Choe, D. Rogers, T. Apple and B.C. Benicewicz, *High-temperature polybenzimidazole fuel cell membranes via a sol–gel process*, Chemistry of Materials, 2005. **17**: p. 5328-5333.
- [25] A. Carollo, E. Quartarone, C. Tomasi, P. Mustarelli, F. Belotti, A. Magistris, F. Maestroni, M. Parachini, L. Garlaschelli and P.P. Righetti, *Developments of new proton conducting membranes based on different polybenzimidazole structures for fuel cells applications*. Journal of Power Sources, 2006. **160**(1): p. 175-180.
- [26] Q. Li and J.O. Jensen, *Membranes for high temperature PEMFC based on acid-doped polybenzimidazoles*, In: K.-V. Peinemann and S.P. Nunes (Eds.) *Membranes for Energy Conversion*. Wiley Online Library, 2008.
- [27] S. Qing, W. Huang and D. Yan, *Synthesis and characterization of thermally stable sulfonated polybenzimidazoles*. European Polymer Journal, 2005. **41**(7): p. 1589-1595.
- [28] S. Yu and B.C. Benicewicz, *Synthesis and Properties of Functionalized Polybenzimidazoles for High-Temperature PEMFCs*. Macromolecules, 2009. **42**(22): p. 8640-8648.
- [29] D.J. Jones and J. Roziere, *Inorganic/organic composite membranes*, in: W. Vielstich, A. Lamn, H.A. Gasteiger and H. Yokokava (Eds.), *Handbook of Fuel Cells*. Wiley Online Library, 2010.
- [30] T. Ogoshi and Y. Chujo, *Organic–inorganic polymer hybrids prepared by the sol–gel method*, Composite Interfaces, 2005. **11**: p. 539-566.
- [31] A.M. Herring, *Inorganic–polymer composite membranes for proton exchange membrane fuel cells*, Journal of Macromolecular Science, Part C: Polymer Reviews, 2006. **46**: p. 245-296.
- [32] H. Pu, L. Liu, Z. Chang and J. Yuan, *Organic/inorganic composite membranes based on polybenzimidazole and nano-SiO₂*. Electrochimica Acta, 2009. **54**(28): p. 7536-7541.
- [33] E. Quartarone, A. Magistris, P. Mustarelli, S. Grandi, A. Carollo, G.Z. Zukowska, J.E. Garbarczyk, J.L. Nowinski, C. Gerbaldi and S. Bodoardo, *Pyridine-based PBI Composite Membranes for PEMFCs*. Fuel Cells, 2009. **9**(4): p. 349-355.
- [34] G. Nawn, G. Pace, S. Lavina, K. Vezzu, E. Negro, F. Bertasi, S. Polizzi and V. Di Noto, *Nanocomposite membranes based on polybenzimidazole and ZrO₂ for high-temperature proton exchange membrane fuel cells*. Chemsuschem, 2015. **8**(8): p. 1381-93.

- [35] J. Lobato, P. Cañizares, M.A. Rodrigo, D. Úbeda and F.J. Pinar, *A novel titanium PBI-based composite membrane for high temperature PEMFCs*. Journal of Membrane Science, 2011. **369**(1-2): p. 105-111.
- [36] J. Lobato, P. Cañizares, M.A. Rodrigo, D. Úbeda and F.J. Pinar, *Enhancement of the fuel cell performance of a high temperature proton exchange membrane fuel cell running with titanium composite polybenzimidazole-based membranes*. Journal of Power Sources, 2011. **196**(20): p. 8265-8271.
- [37] F.J. Pinar, P. Cañizares, M.A. Rodrigo, D. Úbeda and J. Lobato, *Titanium composite PBI-based membranes for high temperature polymer electrolyte membrane fuel cells. Effect on titanium dioxide amount*. RSC Adv., 2012. **2**(4): p. 1547-1556.
- [38] F.J. Pinar, P. Cañizares, M.A. Rodrigo, D. Úbeda and J. Lobato, *Long-term testing of a high-temperature proton exchange membrane fuel cell short stack operated with improved polybenzimidazole-based composite membranes*. Journal of Power Sources, 2015. **274**: p. 177-185.
- [39] H.-L. Lin, T.L. Yu, W.-K. Chang, C.-P. Cheng, C.-R. Hu and G.-B. Jung, *Preparation of a low proton resistance PBI/PTFE composite membrane*. Journal of Power Sources, 2007. **164**(2): p. 481-487.
- [40] S.S. Kocha, J. Deliang Yang and J.S. Yi, *Characterization of gas crossover and its implications in PEM fuel cells*. AIChE Journal, 2006. **52**(5): p. 1916-1925.
- [41] N.N. Greenwood and A. Thompson, *The mechanism of electrical conduction in fused phosphoric acid and trideuterophosphoric acids*. Journal of the Chemical Society, 1959. p. 3485-3492.
- [42] D.-T. Chin and H.H. Chang, *On the conductivity of phosphoric acid electrolyte*. Journal of Applied Electrochemistry, 1989. **19**: p. 95-99.
- [43] C. Korte, *Phosphoric Acid, an Electrolyte for Intermediate-Temperature Fuel Cells –Temperature and Composition Dependence of Vapor Pressure and Proton Conductivity*, in: D. Stolten, B. Emonts (Eds.), *Fuel Cells Science and Engineering*. Wiley VCH, 2012.
- [44] K.-D. Kreuer, J.C. Lassegues and D. Rodriguez, *Proton conductivity in fused phosphoric acid a $^1\text{H}/^{31}\text{P}$ PFG-NMR and QNS study*. Solid State Ionics, 1993. **61**: p. 41-46.
- [45] L. Vilčiauskas, M.E. Tuckerman, G. Bester, S.J. Paddison and K.-D. Kreuer, *The mechanism of proton conduction in phosphoric acid*. Nature Chemistry, 2012. **4**: p. 461-466.
- [46] S.H. Chung, S. Bajue and S.G. Greenbaum, *Mass transport of phosphoric acid in water: A ^1H and ^{31}P pulsed gradient spin-echo nuclear magnetic resonance study*. The Journal of Chemical Physics, 2000. **112**(19): p. 8515-8521.
- [47] Y. Aihara, A. Sonai, M. Hattori and K. Hayamizu, *Ion conduction mechanisms and thermal properties of hydrated and anhydrous phosphoric acids studied with ^1H , ^2H , and ^{31}P NMR*. Journal of Physical Chemistry B, 2006. **110**: p. 24999-25006.
- [48] D.I. MacDonald and J.R. Boyack, *Density, electrical conductivity, and vapor pressure of concentrated phosphoric acid*. Journal of Chemical and Engineering Data, 1969. **14**(3): p. 380-384.
- [49] G. Merkh, R. Pfaff and H.D. Isengard, *Capabilities of automated Karl Fischer titration combined with gas extraction for water determination in selected dairy products*. Food Chemistry, 2012. **132**(4): p. 1736-1740.
- [50] A. Felgner, R. Schlink, P. Kirschenbühler, B. Faas and H.-D. Isengard, *Automated Karl Fischer titration for liquid samples – Water determination in edible oils*. Food Chemistry, 2008. **106**(4): p. 1379-1384.
- [51] S. Grünke, *The influence of conductivity on the Karl Fischer titration*. Food Chemistry, 2003. **82**(1): p. 99-105.
- [52] S.N. Ronkart, M. Paquot, C. Fougnyes, C. Deroanne, J.C. Van Herck and C. Blecker, *Determination of total water content in inulin using the volumetric Karl Fischer titration*. Talanta, 2006. **70**(5): p. 1006-10.

- [53] https://en.wikipedia.org/wiki/Karl_Fischer_titration
- [54] <http://www.splussplus.com/measurement/en/csshunt.html>
- [55] W. Maier, T. Arlt, C. Wannek, I. Manke, H. Riesemeier, P. Krüger, J. Scholta, W. Lehnert, J. Banhart and D. Stolten, *In-situ synchrotron X-ray radiography on high temperature polymer electrolyte fuel cells*. Electrochemistry Communications, 2010. **12**(10): p. 1436-1438.
- [56] W. Maier, T. Arlt, K. Wippermann, C. Wannek, I. Manke, W. Lehnert and D. Stolten, *Investigation of HT-PEFCs by Means of Synchrotron X-ray Radiography and Electrochemical Impedance Spectroscopy*, ECS Transactions, 2011. **41**(1): p. 1413-1422.
- [57] N. Kardjilov, F. Fiori, G. Giunta, A. Hilger, F. Rustichelli, M. Strobl, J. Banhart and R. Triolo, *Neutron tomography for archaeological investigations*. Journal of Neutron Research, 2006. **14**(1): p. 29-36.
- [58] https://en.wikipedia.org/wiki/Neutron_imaging
- [59] P. Boillat, G.G. Scherer, A. Wokaun, G. Frei and E.H. Lehmann, *Transient observation of 2H labeled species in an operating PEFC using neutron radiography*. Electrochemistry Communications, 2008. **10**(9): p. 1311-1314.
- [60] C. Hartnig, I. Manke, N. Kardjilov, A. Hilger, M. Grünerbel, J. Kaczerowski, J. Banhart and W. Lehnert, *Combined neutron radiography and locally resolved current density measurements of operating PEM fuel cells*. Journal of Power Sources, 2008. **176**(2): p. 452-459.
- [61] K.T. Cho and M.M. Mench, *Investigation of the role of the micro-porous layer in polymer electrolyte fuel cells with hydrogen deuterium contrast neutron radiography*. Physical chemistry chemical physics : PCCP, 2012. **14**(12): p. 4296-302.
- [62] A. Putra, H. Iwase, D. Yamaguchi, S. Koizumi, Y. Maekawa, M. Matsubayashi and T. Hashimoto, *In-situ observation of dynamic water behavior in polymer electrolyte fuel cell by combined method of Small-Angle Neutron Scattering and Neutron Radiography*. Journal of Physics: Conference Series, 2010. **247**: p. 012044.
- [63] I. Manke, C. Hartnig, N. Kardjilov, M. Messerschmidt, A. Hilger, M. Strobl, W. Lehnert and J. Banhart, *Characterization of water exchange and two-phase flow in porous gas diffusion materials by hydrogen-deuterium contrast neutron radiography*. Applied Physics Letters, 2008. **92**(24): p. 244101.
- [64] A. Schröder, K. Wippermann, W. Lehnert, D. Stolten, T. Sanders, T. Baumhöfer, N. Kardjilov, A. Hilger, J. Banhart and I. Manke, *The influence of gas diffusion layer wettability on direct methanol fuel cell performance: A combined local current distribution and high resolution neutron radiography study*. Journal of Power Sources, 2010. **195**(15): p. 4765-4771.
- [65] P. Boillat, J. Biesdorf, P. Oberholzer, A. Kaestner and T. J. Schmidt, *Evaluation of Neutron Imaging for Measuring Phosphoric Acid Distribution in High Temperature PEFCs*, Journal of the Electrochemical Society, 2014. **161**(3): p. F192-F198.
- [66] T. Arlt, W. Lücke, N. Kardjilov, J. Banhart, W. Lehnert and I. Manke, *Monitoring the hydrogen distribution in poly(2,5-benzimidazole)-based (ABPI) membranes in operating high-temperature polymer electrolyte fuel cells by using H-D contrast neutron imaging*. Journal of Power Sources, 2015. **299**: p. 125-129.
- [67] N. Kardjilov, A. Hilger, I. Manke and J. Banhart, *CONRAD-2: The neutron imaging instrument at HZB*. Neutron News, 2014. **25**(2): p. 23-26.
- [68] L. Josic, E.H. Lehmann, D. Mannes, N. Kardjilov and A. Hilger, *Investigation of phase transfer properties of light and heavy water by means of energy selective neutron imaging*. Nuclear Instruments and Methods in Physics Research Section A: Accelerators, Spectrometers, Detectors and Associated Equipment, 2012. **670**: p. 68-72.
- [69] C.A. Schneider, W.S. Rasband and K.W. Eliceiri, *NIH Image to ImageJ: 25 years of image analysis*, Nature Methods, 2012. **9**: p. 671-675.

- [70] J.A. Asensio, E.M. Sanchez and P. Gomez-Romero, *Proton-conducting membranes based on benzimidazole polymers for high-temperature PEM fuel cells. A chemical quest*. Chemical Society Reviews, 2010. **39**(8): p. 3210-39.
- [71] J.A. Asensio, S. Borrós and P. Gómez-Romero, *Polymer Electrolyte Fuel Cells Based on Phosphoric Acid-Impregnated Poly(2,5-benzimidazole) Membranes*. Journal of the Electrochemical Society, 2004. **151**(2): p. A304.
- [72] Y.L. Ma, J.S. Wainright, M.H. Litt and R.F. Savinell, *Conductivity of PBI Membranes for High-Temperature Polymer Electrolyte Fuel Cells*. Journal of the Electrochemical Society, 2004. **151**(1): p. A8.
- [73] J. Xue, *Phosphoric acid-doped polybenzimidazole (PBI) membranes for high temperature proton exchange membrane fuel cells (HT-PEMFCs)*. Bachelor thesis, 2015.
- [74] Y. Qiang, *Discussion of the phosphoric acid-doping behavior of PBI membranes with different crosslinked degree*. Bachelor thesis, 2016.
- [75] I.B. Valtcheva, P. Marchetti and A.G. Livingston, *Crosslinked polybenzimidazole membranes for organic solvent nanofiltration (OSN): Analysis of crosslinking reaction mechanism and effects of reaction parameters*. Journal of Membrane Science, 2015. **493**: p. 568-579.
- [76] I.B. Valtcheva, S.C. Kumbharkar, J.F. Kim, Y. Bhole and A.G. Livingston, *Beyond polyimide: Crosslinked polybenzimidazole membranes for organic solvent nanofiltration (OSN) in harsh environments*. Journal of Membrane Science, 2014. **457**: p. 62-72.
- [77] F. Liu, *Interaction of phosphoric acid with cell components in high temperature polymer electrolyte fuel cells*. PhD thesis, 2014.
- [78] F. Conti, F. Bertasi, J. Wackerl, P. Dams, V. Di Noto, W. Lehnert and C. Korte, *Phase diagram approach to study acid and water uptake of polybenzimidazole-type membranes for fuel cells*. ECS Transaction, 2016. **72**(8): p. 157-167.
- [79] Q. Li, R. He, J.O. Jensen and N.J. Bjerrum, *PBI-based polymer membranes for high temperature fuel cells-Preparation, Characterization and Fuel cell demonstration*. Fuel cells, 2004. **4**(3): p. 147-159.
- [80] R. He, Q. Li, G. Xiao and N.J. Bjerrum, *Proton conductivity of phosphoric acid doped polybenzimidazole and its composites with inorganic proton conductors*. Journal of Membrane Science, 2003. **226**(1): p. 169-184.
- [81] N.W. Brooks, R.A. Duckett, J. Rose, I.M. Ward and J. Clements, *An n.m.r. study of absorbed water in polybenzimidazole*. Polymer, 1993. **34**(19): p. 4038-4042.
- [82] R. He, Q. Li, J.O. Jensen and N.J. Bjerrum, *Doping phosphoric acid in polybenzimidazole membranes for high temperature proton exchange membrane fuel cells*. Journal of Polymer Science Part A: Polymer Chemistry, 2007. **45**(14): p. 2989-2997.
- [83] X. Glipa, B. Bonnet, B. Mula, D.J. Jones and J. Boziere, *Investigation of the conduction properties of phosphoric and sulfuric acid doped polybenzimidazole*. Journal of Materials Chemistry, 1999. **9**: p. 3045-3049.
- [84] Q. Li, *Water uptake and acid doping of polybenzimidazoles as electrolyte membranes for fuel cells*. Solid State Ionics, 2004. **168**(1-2): p. 177-185.
- [85] J. Zhang, Z. Xie, J. Zhang, Y. Tang, C. Song, T. Navessin, Z. Shi, D. Song, H. Wang, D.P. Wilkinson, Z.-S. Liu and S. Holdcroft, *High temperature PEM fuel cells*. Journal of Power Sources, 2006. **160**(2): p. 872-891.
- [86] R. He, Q. Li, A. Bach, J. Jensen and N. Bjerrum, *Physicochemical properties of phosphoric acid doped polybenzimidazole membranes for fuel cells*. Journal of Membrane Science, 2006. **277**(1-2): p. 38-45.

- [87] W. Maier, T. Arlt, K. Wippermann, C. Wannek, I. Manke, W. Lehnert and D. Stolten, *Correlation of Synchrotron X-ray Radiography and Electrochemical Impedance Spectroscopy for the Investigation of HT-PEFCs*. Journal of the Electrochemical Society, 2012. **159**(8): p. F398-F404.
- [88] K. Kwon, J.O. Park, D.Y. Yoo and J.S. Yi, *Phosphoric acid distribution in the membrane electrode assembly of high temperature proton exchange membrane fuel cells*. Electrochimica Acta, 2009. **54**(26): p. 6570-6575.
- [89] C.-Y. Chen and W.-H. Lai, *Effects of temperature and humidity on the cell performance and resistance of a phosphoric acid doped polybenzimidazole fuel cell*. Journal of Power Sources, 2010. **195**(21): p. 7152-7159.
- [90] J. Zhang, Y. Tang, C. Song and J. Zhang, *Polybenzimidazole-membrane-based PEM fuel cell in the temperature range of 120–200°C*. Journal of Power Sources, 2007. **172**(1): p. 163-171.
- [91] T. Sousa, M. Mamlouk and K. Scott, *An isothermal model of a laboratory intermediate temperature fuel cell using PBI doped phosphoric acid membranes*. Chemical Engineering Science, 2010. **65**(8): p. 2513-2530.
- [92] C. Korte, F. Conti, J. Wackerl, P. Dams, A. Majerus and W. Lehnert, *Uptake of protic electrolytes by polybenzimidazole-type polymers: absorption isotherms and electrolyte/polymer interactions*. Journal of Applied Electrochemistry, 2015. **45**(8): p. 857-871.
- [93] W. Lehnert, U. Reimer and H. Janßen, *Hochtemperatur-Polymerelektrolyt-Brennstoffzellen*, in: R. Peters (Ed.), *Brennstoffzellensysteme in der Luftfahrt*, Springer, 2015.
- [94] T.J. Schmidt, *High-Temperature Polymer Electrolyte Fuel cells durability insights*, in: F.N. Büchi, M. Inaba and T.J. Schmidt (Eds.), *Polymer electrolyte fuel cell durability*, Springer, 2009.
- [95] Z. Chang, H. Pu, D. Wan, L. Liu, J. Yuan and Z. Yang, *Chemical oxidative degradation of Polybenzimidazole in simulated environment of fuel cells*. Polymer Degradation and Stability, 2009. **94**(8): p. 1206-1212.
- [96] A. Panchenko, H. Dilger, J. Kerres, M. Hein, A. Ullrich, T. Kaz and E. Roduner, *In-situ spin trap electron paramagnetic resonance study of fuel cell processes*. Physical Chemistry Chemical Physics, 2004. **6**(11): p. 2891.
- [97] B. Vogel, E. Aleksandrova, S. Mitov, M. Krafft, A. Dreizler, J. Kerres, M. Hein and E. Roduner, *Observation of Fuel Cell Membrane Degradation by Ex Situ and In Situ Electron Paramagnetic Resonance*. Journal of the Electrochemical Society, 2008. **155**(6): p. B570.
- [98] B. Vogel, H. Dilger and E. Roduner, *Rapid Radical Degradation Test of Polyaromatic Fuel Cell Membranes by Electron Paramagnetic Resonance*. Macromolecules, 2010. **43**(10): p. 4688-4697.
- [99] Y. Oono, A. Sounai and M. Hori, *Prolongation of lifetime of high temperature proton exchange membrane fuel cells*. Journal of Power Sources, 2013. **241**: p. 87-93.
- [100] X. Wu, *Investigation of the dissolution behavior of the polybenzimidazoles (PBIs) in different concentrations of phosphoric acid solution*. Bachelor thesis, 2016.
- [101] https://www.innophos.com/_sitedocs/innophos-phosphoric-acid-table-9.pdf
- [102] P. Atkins and J. De Paula, *Atkins physical chemistry*. 2006. p. 5-38.
- [103] O. Ivanova, W. Lüke, A. Majerus, M. Krutyeva, N.K. Szekeley, W. Pyckhout-Hintzen, M.S. Appavou, M. Monkenbusch, R. Zorn, W. Lehnert and O. Holderer, *Influence of morphology on physical properties of poly(2,5-benzimidazole) membranes*. Journal of Membrane Science, 2017. **533**: p. 342-350.
- [104] D. Aili, L.N. Cleemann, Q. Li, J.O. Jensen, E. Christensen and N.J. Bjerrum, *Thermal curing of PBI membranes for high temperature PEM fuel cells*. Journal of Materials Chemistry, 2012. **22**(12): p. 5444.
- [105] W.F. Hwang, D.R. Wiff, C.L. Benner and T.E. Helminiak, *Composites on a molecular level: Phase relationships, processing, and properties*. Journal of Macromolecular Science, Part B, 2006. **22**(2): p. 231-257.

- [106] R. Kerr, H.R. García, M. Rastedt, P. Wagner, S.M. Alfaro, M.T. Romero, C. Terkelsen, T. Steenberg and H.A. Hjuler, *Lifetime and degradation of high temperature PEM membrane electrode assemblies*. International Journal of Hydrogen Energy, 2015. **40**(46): p. 16860-16866.
- [107] G. Liu, H. Zhang, J. Hu, Y. Zhai, D. Xu and Z.-g. Shao, *Studies of performance degradation of a high temperature PEMFC based on H3PO4-doped PBI*. Journal of Power Sources, 2006. **162**(1): p. 547-552.
- [108] P. Yu, M. Pemberton and P. Plasse, *PtCo/C cathode catalyst for improved durability in PEMFCs*. Journal of Power Sources, 2005. **144**(1): p. 11-20.
- [109] P.J. Ferreira, G.J. la O' , Y. Shao-Horn, D. Morgan, R. Makharia, S. Kocha and H.A. Gasteiger, *Instability of Pt / C Electrocatalysts in Proton Exchange Membrane Fuel Cells*. Journal of the Electrochemical Society, 2005. **152**(11): p. A2256.
- [110] F. Maillard and M. Chatenet, *Ageing mechanisms of Pt/C nanoparticles in a PEMFC*. In : *Conference fundamentals and developments of fuel cell 2008*, nacy, France, 2008.
- [111] K. Yasuda, A. Taniguchi, T. Akita, T. Ioroi and Z. Siroma, *Platinum dissolution and deposition in the polymer electrolyte membrane of a PEM fuel cell as studied by potential cycling*. Physical chemistry chemical physics : PCCP, 2006. **8**(6): p. 746-52.
- [112] W. Bi, G.E. Gray and T.F. Fuller, *PEM Fuel Cell Pt / C Dissolution and Deposition in Nafion Electrolyte*. Electrochemical and Solid-State Letters, 2007. **10**(5): p. B101.
- [113] M.M. Mench, E.C. Kumbur and T.N. Veziroglu, *Polymer Electrolyte Fuel Cell Degradation*. Academic Press, 2012.
- [114] S. Galbiati, A. Baricci, A. Casalegno and R. Marchesi, *Degradation in phosphoric acid doped polymer fuel cells: A 6000 h parametric investigation*. International Journal of Hydrogen Energy, 2013. **38**(15): p. 6469-6480.
- [115] Z.G. Qi and S. Buelte, *Effect of open circuit voltage on performance and degradation of high temperature PBI-H3PO4 fuel cells*. Journal of Power Sources, 2006. **161**(2): p. 1126-1132.
- [116] L. Lücke, *Analyse des Betriebsverhaltens von Hochtemperatur-Polymerelektrolyt-Brennstoffzellen*, PhD thesis, 2013.
- [117] M. Kvesić, U. Reimer, D. Froning, L. Lücke, W. Lehnert and D. Stolten, *3D modeling of an HT-PEFC stack using reformat gas*. International Journal of Hydrogen Energy, 2012. **37**(17): p. 12438-12450.
- [118] A.A. Kulikovskiy, A. Kucernak and A.A. Kornyshev, *Feeding PEM fuel cells*. Electrochimica Acta, 2005. **50**(6): p. 1323-1333.
- [119] P. Chippar and H. Ju, *Three-dimensional non-isothermal modeling of a phosphoric acid-doped polybenzimidazole (PBI) membrane fuel cell*. Solid State Ionics, 2012. **225**: p. 30-39.
- [120] Y. Lin, T. Arlt, N. Kardjilov, I. Manke and W. Lehnert, *Operando neutron radiography analysis of high temperature polymer electrolyte fuel cell based on a phosphoric acid-doped polybenzimidazole membrane using the hydrogen-deuterium contrast method*. Electrochimica Acta, under review.
- [121] G.G. Scherer, *Fuel cell types and their electrochemistry*, in: K.-D. Kreuer (Ed.), *Fuel cells: selected entries from the encyclopedia of sustainability science and technology*, Springer, 2013.
- [122] http://www1.lsbu.ac.uk/water/water_properties.html#tcoef [accessed on January 9 2017]
- [123] <http://cccbdb.nist.gov/hf0k.asp> [accessed on January 9 2017]
- [124] G. H. Aylward and T. J. V. Findlay, *Datensammlung Chemie in SI-Einheiten*, VCH, edition 2, 1986.
- [125] <https://www.ncnr.nist.gov/instruments/bt1/neutron.html> [accessed on March 10 2017]
- [126] K.-D. Kreuer, *Proton Conductivity-Materials and Applications*, Chemistry of Materials, 1996. **8**: p. 610-641.
- [127] R. Vuilleumier and D. Borgis, *Proton conduction: Hopping along hydrogen bonds*, Nature Chemistry, 2012. **4**: p. 432-433.

- [128] R.E. Mesmer and D.L. Herting, *Thermodynamics of Ionization of D₂O and D₂PO₄⁻*, Journal of Solution Chemistry, 1978. **7**(12): p. 901-912.
- [129] A.S. Nowick and A.V. Vaysleyb, *Isotope effect and proton hopping in high-temperature protonic conductors*. Solid State Ionics, 1997. **97**: p. 17-26.
- [130] J.H. Sluyters and M. Sluyters-Rehbach, *The mechanism of the hydrogen ion conduction in liquid light and heavy water derived from the temperature dependence of their limiting conductivities*. Journal of Physical Chemistry B, 2010. **114**: p. 15582-15589.
- [131] M. Heres, Y. Wang, P.J. Griffin, C. Gainaru and A.P. Sokolov, *Proton Conductivity in Phosphoric Acid: The Role of Quantum Effects*. Physical review letters, 2016. **117**(15): p. 156001.
- [132] U. Reimer, J. Ehlert, H. Janßen and W. Lehnert, *Water distribution in high temperature polymer electrolyte fuel cells*. International Journal of Hydrogen Energy, 2016. **41**(3): p. 1837-1845.
- [133] S.H. Eberhardt, M. Toulec, F. Marone, M. Stampanoni, F.N. Buchi and T.J. Schmidt, *Dynamic Operation of HT-PEFC: In-Operando Imaging of Phosphoric Acid Profiles and (Re)distribution*. Journal of the Electrochemical Society, 2015. **162**(3): p. F310-F316.
- [134] S. Thomas, *Operational strategies for longer durability of HT-PRM fuel cells operating on reformed methanol*, PhD thesis, 2018.
- [135] T.-H. Kim, T.-W. Lim and J.-C. Lee, *High-temperature fuel cell membranes based on mechanically stable para-ordered polybenzimidazole prepared by direct casting*. Journal of Power Sources, 2007. **172**(1): p. 172-179.
- [136] S. Thomas, C. Jeppesen, T. Steenberg, S.S. Araya, J.R. Vang and S.K. Kær, *New load cycling strategy for enhanced durability of high temperature proton exchange membrane fuel cell*. International Journal of Hydrogen Energy, 2017. **42**(44): p. 27230-27240.

Nomenclature

Abbreviation

PEFC	polymer electrolyte fuel cell
HT-PEFC	high temperature polymer electrolyte fuel cell
PBI	polybenzimidazole
GDL	gas diffusion layer
MEA	membrane electrolyte assembly
PPA	polyphosphoric acid
DoE	Department of Energy
AB-PBI	poly(2,5-benzimidazole)
m-PBI	poly[2,2'-(m-phenylene)-5,5'-bibenzimidazole]
p-PBI	poly[2,2'-(p-phenylene)-5,5'-bibenzimidazole]
NMP	N-methylpyrrolidone
DMAc	N,N-dimethylacetamide
PTFE	Poly tetra fluoroethylene
OCV	open cell voltage
PFG-NMR	pulsed field gradient – nuclear magnetic resonance
KFT	Karl Fischer Titration
DBX	dibromoxylene
WU	water uptake
ADL	acid doping level
GDE	gas diffusion electrode

EPR	electron spin-resonance spectroscopy
SEM	scanning electron microscope
EDX	Energy Dispersive X-Ray Spectroscopy
EIS	electrochemical impedance spectroscopy
ORR	oxygen reduction reaction
HOR	hydrogen oxidation reaction

Latin symbols

I_m	A	current need to be measured of the shunt
U_t	V	measured voltage of the shunt
R	Ω	resistance of the shunt
WU		the mole number of water molecules per mole repeating unit of PBI membrane
ADL		the mole number of phosphoric acid molecules per mole repeat unit of PBI membrane
Q	%	the ratio of “weight increased of membrane after doping” to “weight of membrane in the dry state”
$C_{(PA/H_2O)}$		the mole number of phosphoric acid molecules per mole water molecule in the membrane after doping
W_{H_2O}	g	weight of water absorbed by membranes after doping process and measured by Karl Fischer titration
W_{dry}	g	weight of mPBI membranes at dry state
W_{doped}	g	weight of mPBI membranes after doping process
M_{H_2O}	$g\ mol^{-1}$	molar mass of water, $18\ g\ mol^{-1}$
M_{PA}	$g\ mol^{-1}$	molar mass of phosphoric acid, $98\ g\ mol^{-1}$
M_{mPBI}	$g\ mol^{-1}$	molar mass of repeating unit of mPBI, $308\ g\ mol^{-1}$, as structure shown in Figure 2.1
T_s	%	thickness swelling

V_s	%	volumetric swelling
d_{doped}	μm	thickness of membranes after doping process
l_{doped}	cm	length of membranes after doping process
w_{doped}	cm	width of membranes after doping process
d_{dry}	μm	thickness of membranes in the dry state
l_{dry}	cm	length of membranes in the dry state
w_{dry}	cm	width of membranes in the dry state
x		molar fraction of PBI, phosphoric acid and water in the ternary system of $m\text{-PBI} - \text{H}_3\text{PO}_4 - \text{H}_2\text{O}$
W_0	g	weight of initial membranes at dry state
W_1	g	weight of membranes after dissolution test at dry state
W'_0	g	weight of initial membranes after washing by NaOH solution
L	Henry	cable inductance
R_Ω	mohm cm^2	ohmic resistance
R_{ct}	mohm cm^2	charge transfer resistance (kinetic resistance)
CPE_{ct}	Farad cm^{-2}	constant phase element of ORR kinetic
R_m	mohm cm^2	mass transport resistance
CPE_m	Farad cm^{-2}	constant phase element of mass transport
$C/\%$	%	atom fractions of C in the adhered catalyst layers
$F/\%$	%	atom fractions of F in the adhered catalyst layers
$Pt/\%$	%	atom fractions of Pt in the adhered catalyst layers
M_C	g mol^{-1}	molar weight of the C atom
M_{Pt}	g mol^{-1}	molar weight of the Pt atom
c_x	%	oxygen concentration along the channel
c^0	%	oxygen concentration at gas inlet (in air, it is approximately 21% in volume fraction)

x		coordinate along the gas flow direction
L		length of the channel
j_x	mA cm^{-2}	local current density
\bar{j}	mA cm^{-2}	average current density
c'_x	%	water vapor concentration in volume fraction along the channel
$P_{\text{H}_2\text{O}}$	mbar	water vapor partial pressure along the channel
P	mbar	ambient pressure
R_{mem}	mohm cm^2	ohmic resistance of the membrane along the gas flow
		Orientation
E_{cell}	V	cell voltage
E_{Nernst}	V	Nernst voltage
j	A	current of the cell
η_{act}	V	voltage loss by the activation
η_{trans}	V	voltage loss by mass transport
E_0	V	standard potential
$X_{\text{H}_2\text{O}}$	%	mole fraction of H_2O in gas phase
X_{H_2}	%	mole fraction of H_2 in gas phase
X_{O_2}	%	mole fraction of O_2 in gas phase
R	$\text{J mol}^{-1} \text{K}^{-1}$	gas constant
F		Faraday constant
T	K	cell temperature
ΔG	KJ mol^{-1}	Gibbs free energy
n	mol	molar value of the transferred electrons
I_t	a.u.	transmitted intensity of the beam
I_0	a.u.	incident intensity of the beam

μ_i	cm^{-1}	attenuation coefficient of each layer
z_i	μm	thickness of each layer
z	μm	thickness of H_3PO_4 layer
μ_H	cm^{-1}	attenuation coefficients of H_3PO_4
μ_D	cm^{-1}	attenuation coefficients of D_3PO_4
I_H	a.u.	average transmitted intensity of the beam for H_2 operation
I_D	a.u.	average transmitted intensity of the beam for D_2 operation
N	cm^{-2}	the amount of positive charge carriers in 1 cm^2
m_{PA}	g cm^{-2}	the mass of phosphoric acid uptake (nearly 0.015 g cm^{-2})
M_{PA}	g mol^{-1}	the molar mass of phosphoric acid (98 g mol^{-1})
N_A	mol^{-1}	the Avogadro constant ($6.02 \times 10^{23} \text{ mol}^{-1}$)
N'	$\text{cm}^{-2} \text{ s}^{-1}$	the amount of exchanged electric charges
I	A cm^{-2}	current density (0.2 A cm^{-2})
C	$\text{A}^{-1} \text{ s}^{-1}$	the constant of the amount of electrons in 1 A current within 1 s ($6.24 \times 10^{18} \text{ A}^{-1} \text{ s}^{-1}$)
Q_{OH}	eV	energy of the OH oscillator
Q_{OD}	eV	energy of the OD oscillator
Greek symbols		
θ	%	crosslinking degree of the membrane, as well as the weight percent of DBX in the crosslinked membrane. In the case of pure PBI, it is zero.
δ	%	weight loss of membranes after dissolution
δ'	%	weight loss of membranes caused by dissolution
λ		stoichiometry of cathode gas

List of Figures

Figure 1.1: The basic working principle of HT-PEFC	2
Figure 2.1: Chemical structures of the repeating units of PBI (left) and AB-PBI (right).	6
Figure 2.2: Proton migration via hopping mechanism in PBI/H ₃ PO ₄ system. (a) at low concentration of H ₃ PO ₄ in the membrane, protons transfer between free water molecules; (b) at high concentration of H ₃ PO ₄ in the membrane, protons transfer through bonded H ₃ PO ₄ network.....	12
Figure 2.3: Karl Fischer Titration system	14
Figure 2.4: Principle of current scan shunt [53]	16
Figure 2.5: The sensor plate of current scan shunt.....	16
Figure 2.6: The sensor plate in a test cell	17
Figure 2.7: Schematic of Neutron radiography measurement.....	18
Figure 2.8: Experimental setup for this in-operando neutron radiographic measurement of the HT-PEFC. The tube length between 3 way-valve and gas pressure reducing valve is about 10 m, gas pressure inside the tube is about 3 bar; the tube length between pressure reducing valve and mass flow controller is about 1 m, gas pressure inside the tube is about 2 bar; the tube length between mass flow controller and cell inlet is about 1.5 m. gas pressure inside the tube is ambient pressure. The diameter of all the tubes is 0.4 cm.	19
Figure 3.1: Crosslinking mechanism of PBI with DBX.	23
Figure 3.2: Schematic of doping membrane in closed vessel.	23
Figure 3.3: Ternary phase diagram of the <i>m</i> -PBI – H ₃ PO ₄ – H ₂ O system, composition is given in molar fraction, grey areas mark the two-phase field.	26
Figure 3.4: Water uptake as the function of doping temperature for m-PBI membranes.	27
Figure 3.5: Absorption isotherm for water uptake for m-PBI membranes. The solid lines are fitted with the data.	28
Figure 3.6: Water uptake of membranes with different crosslinked degree doped in a series concentration of phosphoric acid solutions in closed vessels at 110 °C. The solid lines are fitted with the data.	29

Figure 3.7: Acid doping level of pure m-PBI as a function of acid concentration in solution at a series doping temperature. The solid lines are fitted with the data.....	31
Figure 3.8: The acid doping level of crosslinked m-PBI and non-crosslinked m-PBI membranes as the function of acid concentration in solution at 110 °C. The solid lines are fitted with the data.	32
Figure 3.9: The 3D mapping surface of acid concentration in polymer of pure m-PBI regarding the acid concentration in solution and doping temperature.	33
Figure 3.10: The failures of membrane at the boundary between membrane and gaskets.	35
Figure 3.11: The influence of acid (a) and water uptake (b) on the thickness swelling for acid doped m-PBI membranes.	36
Figure 3.12: Volumetric swelling of PBI membranes with different crosslinked degree as a function of acid doping level.....	37
Figure 3.13: The thickness swelling of crosslinked/non-crosslinked m-PBI membranes as a function of acid concentration in solutions.	38
Figure 3.14: Acid doping level (ADL) of Fumapem AM-55 at 110 °C as a function of the total absorption (Q) of the polymer.	40
Figure 3.15: The polarization curves of HT-PEFCs based on m-PBI membranes with different acid doping levels.....	41
Figure 4.1: The photographs of AB-PBI dissolution process at 90°C (a) the swollen state of the membrane after 4hours (b) the state of the membrane at the breaking time, i.e. 24h (c) the state of the membrane breaking into small pieces after 2 days (d) the state of the dried membrane after 5 days.....	49
Figure 4.2: The photographs of AB-PBI dissolution process at 110°C (a) the swollen state of the membrane after 1.5h (b) the state of the membrane at the breaking time, i.e.4.5h (c) the swollen states of every broken pieces of the membrane after 5h (d) the state of the solution with the membrane completely dissolving.	50
Figure 4.3: The photographs of AB-PBI dissolution process at 110°C (a) the swollen state of the membrane after only 2min (b) the state of the membrane at the breaking time, i.e. 10min.....	50
Figure 4.4: The curly state of the crosslinked AB-PBI membranes at various temperatures.	52
Figure 4.5: The crimping time of crosslinked AB-PBI membranes immersed at various temperatures in an open vessel.	52
Figure 4.6: The weight loss of crosslinked AB-PBI membrane at various temperatures as a function of time in an open vessel.	54

Figure 4.7: (a) The photographs of membranes in 85 wt.-% and 95 wt.-% phosphoric acid solutions for half month; (b) The photographs of phosphoric acid with various concentrations after membranes being taken out at the fifth day.	54
Figure 4.8: The weight loss of AB-PBI membranes (left) and crosslinked AB-PBI membranes (right) in various concentration of phosphoric acid as a function of time at 160 °C.	55
Figure 4.9: The weight loss of non-crosslinked AB-PBI membranes and crosslinked AB-PBI membranes in various concentration of phosphoric acid solution after 40 h.	56
Figure 5.1: Equivalent circuit of HT-PEFC for Nyquist plots fitting.	60
Figure 5.2: The flow field of the bipolar plate used in this work. The red rectangle represents how the samples of MEAs were cut.	62
Figure 5.3: (a) and (b) are the photographs of sample #0 and sample #2 respectively. The bottom schematic is the cross-section of MEA with bipolar plates.	63
Figure 5.4: The results of single cell test. (Upper left) the polarization curves of cell #1 before and after long-term test; (Upper right) the durability test of cell #1 at 200 mA cm ⁻² ; (Bottom left) the polarization curves of cell #2 before and after long-term test; (Bottom right) the durability test of cell #2 at 200 mA cm ⁻² . Testing condition: $\lambda_{An/Ca}=2/2$, T = 160 °C.	64
Figure 5.5: The EIS results of cell #1 and #2 after break-in procedure and long-term test at 200 mA cm ⁻² , $\lambda_{An/Ca}=2/2$, T = 160 °C. The frequency range was from 100 kHz to 100 mHz and AC signal voltage amplitude was ± 5 mV.	66
Figure 5.6: The SEM images of cross-section of used membranes. (a) and (b) were the membrane under the channel of flow field and it under the rib of flow field for sample #0, as well as after 70 h operation; (c) and (d) were the membrane under the channel and the rib for sample #1, as well as after 600 h operation; (e) and (f) were the membrane under the channel and the rib for sample #2, as well as after 950 h operation.	69
Figure 5.7: The thicknesses of different membranes. A): the initial membrane; B): the dried membrane after pre-doped and pre-washed process; C): the membrane under channel for sample #0; D): the membrane under rib for sample #0; E): the membrane under channel for sample #1; F): the membrane under rib for sample #1; G): the membrane under channel for sample #2; H): the membrane under rib for sample #2.	70
Figure 5.8: (a) The cross section image of sample #0 under polarizing microscopy; (b) The SEM image of the surface of catalyst layer.	71
Figure 5.9: Cross-sectional FIB-SEM images. (a) and (b) were the two sides of the membrane used for break-in procedure; (c) and (d) were the two sides of the membrane used for 300 h at various current density.	72
Figure 5.10: The SEM images of the cross-section of the membranes of sample #0 (a), sample #1 (b) and sample #2 (c) used for the EDX analysis.	74

Figure 6.1: Long cell design with five straight parallel gas channels.....	77
Figure 6.2: Scheme of the MEA assembling.	78
Figure 6.3: Temperature distribution along the channel for different heating managements.	79
Figure 6.4: Local current density distribution along the channel of the cell at various average current densities with two different heating methods. $\lambda_{an/ca}=2/2$, co-flow, gas orientation from left to right.	80
Figure 6.5: Oxygen concentration along the channel, calculated via Eq. (6.1). $\lambda_{air}=2$	82
Figure 6.6: Local current density along the channel. Black line is the results calculated via Eq. (6.2), red line is the experimental results (heating method #2). Average current density is 200 mA cm^{-2} , $\lambda_{air}=2$	83
Figure 6.7: Water vapor partial pressure along the channel, calculated via Eq. (6.6). Average current density is 200 mA cm^{-2} , $\lambda_{air}=2$	84
Figure 6.8: Local current density along the channel. Average current density is 200 mA cm^{-2} , $\lambda_{air}=2$	86
Figure 7.1: The photograph of the cell located in the neutron beam. Yellow arrows represent the beam direction which was in-plane of the cell. The gas flow orientation was from right to left.	90
Figure 7.2: Changes in the cell voltage during the measurement time. Operating conditions for each part: 200 mA cm^{-2} (A): $\lambda_{an/ca}=2/2$; 200 mA cm^{-2} (B): $\lambda_{an/ca}=2/4$; 200 mA cm^{-2} (C): $\lambda_{an/ca}=2/6$; 400 mA cm^{-2} : $\lambda_{an/ca}=2/2$; 600 mA cm^{-2} : $\lambda_{an/ca}=2/2$	91
Figure 7.3: Polarization curves of the cell with H_2 and D_2 as anode gas supply at $\lambda_{an/ca}=2/2$, $T=160^\circ\text{C}$	91
Figure 7.4: Impedance spectra of the cell measured at 200 mA cm^{-2} , $\lambda_{an/ca}=2/2$, $T=160^\circ\text{C}$, frequency range from 100 kHz to 100 mHz , the AC amplitude is 10 mV	93
Figure 7.5: The transmittance of the cell at the first switching circle ($\text{H}_2\text{-D}_2\text{-H}_2$). The red line is the smoothed result of the transmittance.	95
Figure 7.6: (a) and (b) show radiographs of the cell after the switchover from H-to-D and D-to-H, respectively. The direction of the white arrow in (a) is the gas flow orientation; (c) and (d) show the changes of cell voltage after the exchange of H-to-D and D-to-H (magnification of Figure 7.2) corresponding to the radiographs, above.....	96
Figure 7.7: The scheme of the exchange process of H-to-D and D-to-H in model 1.....	99
Figure 7.8: The scheme of the exchange process of H-to-D and D-to-H in model 2.....	100
Figure 7.9: (a) The transmittance (average transmittance of the selected red rectangular area on the above radiograph) changes over time at the different position of the cell at 200 mA cm^{-2} , $\lambda_{an/ca}=2/2$.	

(b) The transmittance changes rate of the H-to-D exchange process fitted by the curves in gray rectangle shown in (a).	103
Figure 7.10: (a), (b) and (c) show radiographs of the cell after the switchover from H-to-D at current densities of 200 mA cm^{-2} , 400 mA cm^{-2} and 600 mA cm^{-2} respectively, but with identical stoichiometry $\lambda_{\text{an/ca}}=2/2$; (d) average transmittance changes for the entire active area of the cell, corresponding to the radiographs displayed here.	105
Figure 7.11: Transmittance of the whole active area of the cell over time with various cathode stoichiometries $\lambda_{\text{an/ca}}=2/2$, $\lambda_{\text{an/ca}}=2/4$ and $\lambda_{\text{an/ca}}=2/6$ at 200 mA cm^{-2}	106
Figure 7.12: The possible phosphoric acid redistribution principle in the cathodic catalyst layer by increasing the gas flow rate at cathode.	107
Figure 7.13: 3D surface plots of the radiographs of the cell with H_2 (a) and D_2 (b) operation normalized by H_2 operation condition.	108

List of Tables

Table 2.1: Derivatives of PBI.....	8
Table 3.1: The list of series concentration of phosphoric acid.....	22
Table 4.1: Density of phosphoric acid (over 85 wt.-%) [97]	44
Table 4.2: The weight loss of initial membranes washed by NaOH solutions and distilled water.	46
Table 4.3: The weight loss of doped membranes washed by NaOH solutions and distilled water.	47
Table 4.4: The breaking time and dissolution time of membranes dissolving at different temperatures.....	51
Table 5.1: The physical meaning of each element shown in Figure 5.1.....	61
Table 5.2: The fitting result of each resistor of the cells at 200 mA cm^{-2} with the equivalent circuit shown in Figure 5.1.	67
Table 5.3: The atom fractions of C, F, and Pt in the adhered catalyst layers.	74
Table 5.4: The atom ratios of C/Pt in the adhered catalyst layers for different samples, as well in the initial catalyst layer.....	76
Table 7.1: Thermodynamic data [113-115] and calculated standard voltages of different reactions for 25°C and ambient pressure.....	93
Table 7.2: The attenuation coefficients for different materials [116].	94

Acknowledgments

The four years of my PhD study in Germany is going to be finished. When I look back, there are many people I would like to say thank you, for their friendship, advice, and support.

First of all, I would like to thank my supervisor as well as doctor father, Professor Werner Lehnert, for giving me the opportunity to study my PhD in Forschungszentrum Jülich. Prof. Lehnert has supported my study and research all the time with his patience, encouragement, and knowledge. Without his help, I could not complete my PhD study smoothly. Additionally, I am grateful to the China Scholarship Council (CSC) who provides the funding of my study in Germany.

My sincere thanks also go to the rest of my doctor defense committee: Professor Matthias Wessling, and Professor Andreas Jupke, for their valuable time, effort and insightful comments.

I also would like to say thank you to Dr. Carsten Korte, Dr. Uwe Reimer, Dr. Holger Janßen, Dr. Klaus Wippermann, Dr. Tobias Arlt, Dr. Nikolay Kardjilov, Dr. Marina Khanef and Dr. Olaf Holderer. Thanks a lot to all of you for your patience, guidance, inspired discussion and successful cooperation. In addition, this work was also helped by other colleagues: technical support from Birgit Schumacher, Walter Zwaygardt, Daniel Holtz, and Katja Klafki; experimental work from bachelor students, Jianmin Xue, Yiwei Qiang and Xi Wu.

Dr. Michael Höh, Shuai Liu, Olha Panchenko, Daniel Holtz, Walter Zwaygardt, and Deepjyoti Borah, I will never forget the time that we spent together in HZB and MLZ for the neutron beam-time. It is also a pleasure to thank my colleagues in IEK-3: Dr. Qing Cao, Dr. Vitali Weißbecker, Huijie Zhang, Dr. Junliang Yu, Dr. Yasser Rahim, Yulin Yan, Mian Bilal Hussain, Shidong Zhang, Yuan Wang, Dr. Diankai Qiu, Prof. Xu, Prof. Ni, Ruiyu Li and Yun Cai, who helped me in numerous ways during various stages of my PhD. The interesting discussions and fun we have had in the last years will stay in my mind, and the friendships among us will never end.

At Last, I sincerely appreciate my parents and my wife, Chang Liu who is also doing her PhD study in our institute, for their love, encouragement and understanding. This work is dedicated to them.

Band / Volume 429

Characterization of spatial-temporal varying riverbed hydraulic conductivity and its role on the estimation of river-aquifer exchange fluxes with data assimilation

Q. Tang (2018), xv, 117 pp

ISBN: 978-3-95806-339-6

Band / Volume 430

Der Einfluss von Wasserdampf auf den Sauerstofftransport in keramischen Hochtemperaturmembranen

F. Thaler (2018), ii, 93, XXXI pp

ISBN: 978-3-95806-340-2

Band / Volume 431

Analysis & modeling of metastable photovoltaic technologies: towards dynamic photovoltaic performance models

M. Görig (2018), 246 pp

ISBN: 978-3-95806-342-6

Band / Volume 432

Laser Treatment of Silicon Thin-Films for Photovoltaic Applications

C. Maurer (2018), vii, 165 pp

ISBN: 978-3-95806-347-1

Band / Volume 433

Mentalitäten und Verhaltensmuster im Kontext der Energiewende in NRW

K. Schürmann & D. Schumann (Hrsg.) (2018), 236 pp

ISBN: 978-3-95806-349-5

Band / Volume 434

Adhäsionsverhalten von wässrigen Nafion-Lösungen an dispersen Phasengrenzen

A. Schulz (2018), xii, 129 pp

ISBN: 978-3-95806-354-9

Band / Volume 435

Alterungs- und fehlertolerante optimale Betriebsführung eines Direktmethanol-Brennstoffzellensystems

R. Keller (2018), XX, 175 pp

ISBN: 978-3-95806-355-6

Band / Volume 436

Chamber study of biogenic volatile organic compounds: plant emission, oxidation products and their OH reactivity

Y. Zhujun (2018), ix, 139 pp

ISBN: 978-3-95806-356-3

Band / Volume 437

Characterization of High Temperature Polymer Electrolyte Fuel Cells

Y. Rahim (2018), iii, 162 pp

ISBN: 978-3-95806-359-4

Band / Volume 438

**Lattice Boltzmann Simulation in Components of
Polymer Electrolyte Fuel Cell**

J. Yu (2018), ii, 173 pp

ISBN: 978-3-95806-360-0

Band / Volume 439

Quantitative Luminescence Imaging of Solar Cells

V. Huhn (2018), 155 pp

ISBN: 978-3-95806-363-1

Band / Volume 440

**Characterization of Phosphoric Acid Doped Polybenzimidazole
Membranes**

Y. Lin (2018), II, IV, 140 pp

ISBN: 978-3-95806-364-8

Weitere **Schriften des Verlags im Forschungszentrum Jülich** unter
<http://www.zbw1.fz-juelich.de/verlagextern1/index.asp>

Energie & Umwelt / Energy & Environment
Band / Volume 440
ISBN 978-3-95806-364-8